

MASTER'S THESIS

Scattering and Absorption Analysis of Radomes Using the Method of Equivalent Dipole Moments

Majid Naeem

Department of Signals and Systems
CHALMERS UNIVERSITY OF TECHNOLOGY
Göteborg, Sweden, October 2011

R&D Section
Netherlands Institute for Radio Astronomy (ASTRON)
Dwingeloo, The Netherlands, October 2011

Scattering and Absorption Analysis of Radomes Using the Method of Equivalent Dipole Moments

MASTER's THESIS

as part of mandatory clauses in
fulfillment of Master's Degree from the
Chalmers University of Technology, Gothenburg, Sweden

by

Majid Naeem
Department of Signals and Systems

October 11, 2011

Scattering and Absorption Analysis of Radomes Using the Method of Equivalent Dipole Moments / by

Majid Naeem. - Gothenburg : Chalmers University of Technology, 2011.

Copyright ©2011 by M. Naeem, Antenna Group, Signals and Systems Department, Chalmers University of Technology, Gothenburg, Sweden; The Netherlands Institute for Radio Astronomy (ASTRON), Dwingeloo, The Netherlands.

The Author grants to Chalmers University of Technology the non-exclusive right to publish the Work electronically and in a non-commercial purpose make it accessible on the Internet. The Author warrants that he/she is the author to the Work, and warrants that the Work does not contain text, pictures or other material that violates copyright law.

The Author shall, when transferring the rights of the Work to a third party (for example a publisher or a company), acknowledge the third party about this agreement. If the Author has signed a copyright agreement with a third party regarding the Work, the Author warrants hereby that he/she has obtained any necessary permission from this third party to let Chalmers University of Technology store the Work electronically and make it accessible on the Internet.

This thesis is carried out under supervision of:

Dr. Rob Maaskant

Examiner:

Prof. Dr. Per-Simon Kildal

Co-Supervisor:

Dion Kant

Technical Report No. 2011:xx

Antenna Group, Department of Signals and Systems

Chalmers University of Technology,

SE-41296, Gothenburg, Sweden.

Telephone: +46 31 772 1000

Cover design: Majid Naeem (Picture on the left shows the discretization of the object after invoking the volume equivalence principle, while the picture on the right depicts a dipole array of two elements covered by a radome.)

Press: Chalmers Reproservice, Göteborg

I dedicate my work presented in this thesis to my parents.

Acknowledgements

First and foremost, I want to thank Dr. Rob Maaskant for providing me the opportunity to work on this Master Thesis project. Throughout the project, he has been generous in helping and encouraging. The technical concepts that I have built under his guidance will surely help me throughout my career. I must express my gratitude to him for being kindly responsive to my questions; a couple of which had even less relevance to this particular project but helped me in broadening my vision in electromagnetics field.

I am grateful to Prof. Per-Simon Kildal for giving me the opportunity to perform towards this Master Thesis project, and providing me with his kind suggestions during the implementation phase.

My co-supervisor Mr. Dion Kant has been very helpful after the time Dr. Rob Maaskant left ASTRON. My heartiest thanks to him for being so helpful.

I want to thank Mr. Michel Arts—who is one of my colleagues at ASTRON—for being immediately responsive to my queries, which helped me to clarify many of the electromagnetics concepts.

Of course, I can not forget to thank Prof. Raj Mittra—from Pennsylvania State University, USA—for sharing his vast experience with me, and advising me during the implementation phase. The fundamental concept of the method, developed in this Master Thesis project, was introduced by him.

Last but not least, I would like to thank ASTRON and Dr. Miroslav—from the Onsala Space Observatory, Sweden—for providing the financial support to complete this project.

Abstract

A primary function of radomes is to protect the antenna against climate change. However, its presence can have a detrimental effect on the antenna radiation pattern if it has not been taken into account during the electromagnetic design of the antenna system. Another complication is that existing commercial electromagnetic software packages are known to be inefficient and/or inaccurate for solving electromagnetic problems involving electrically thin and/or complex-shaped objects.

In this work a novel method is presented, which is simple to implement and yields potentially more accurate results as compared to existing commercial software packages. Furthermore, efficiency enhancement techniques are employed to alleviate the computational burden of the implemented method.

A universal approach is presented—utilizing cube-shaped high resolution basis functions—for solving multi-scale scattering problems. A major advantage of employing micro-domain basis functions is the ability to discretize arbitrarily-shaped geometries more accurately as compared to conventional types of basis functions which are typically one to two orders larger in size. However, increasing the number of basis functions increases the computation time and decreases the memory efficiency of a standard method of moments (MoM) approach. In order to overcome this problem, we exploit translation symmetry and use the Adaptive Cross Approximation (ACA) algorithm to ameliorate time efficiency, while the Characteristic Basis Function Method (CBFM) is an effective approach for mitigating the memory storage requirements. Moreover, the approach lends itself for a parallel implementation and involves supplementary analytical computations for dealing with the field singularities.

To verify the proposed method, a number of dielectric scattering problems have been solved and results have been compared to the commercially available HFSS and WIPL-D softwares, as well as the analytical Mie-series solution. The results obtained through our method generally demonstrate high accuracy and computational efficiency in comparison with the results obtained by the HFSS software.

After validating the novel implemented numerical method, the operating principle of the Substrate Measurement System (SMS) is described for measuring the permittivity and the loss tangent of dielectric materials. The procedure for the calculation of the constitutive parameters of the materials, used by the SMS, are detailed. To complete the study, the scattering from both flat and shaped radomes have been analyzed for the herein presented method, called MEDM, and the detrimental effect of the radome on the antenna radiation pattern are examined

Contents

1	Introduction	1
1.1	Background Information	1
1.2	Brief Review of Computational Electromagnetic Methods	3
1.3	Organization of the Thesis	5
2	The Method of Equivalent Dipole Moments (MEDM)	7
2.1	Introduction	7
2.2	Mathematical Problem Formulation	8
2.2.1	The Volume Equivalence Principle	9
2.2.2	The Electric-Field Integral Equation (EFIE)	10
2.3	The Method of Weighted Residuals (MWR)	12
2.4	Conclusions	15
3	Choice of Basis and Testing Functions	17
3.1	Introduction	17

3.1.1	Basis Function Selection	18
3.1.2	Selection of Weighting Functions	19
3.2	Computation of the Moment Matrix Elements	19
3.2.1	The Self-Term Z_{nn}	19
3.2.2	The Off-Diagonal Moment Matrix Term Z_{mn} ($m \neq n$)	22
3.3	Conclusions	24
4	Numerical Validation	25
4.1	Mie-Series Solution	25
4.2	Mie-Series Validation	29
4.2.1	Comparison With a Published Mie-Series Solution	29
4.2.2	Mie-Series in Comparison With HFSS	29
4.3	MEDM in Comparison with Ansoft's HFSS and WIPL-D	31
4.3.1	Scattering From a Dielectric Sphere	31
4.3.2	Scattering From a Small Plate	35
4.3.3	Scattering From a Small Dielectric Cube	36
4.4	Convergence Study	37
4.5	Conclusions	39
5	Solution to Large Problems	41
5.1	Introduction	41

5.2	Formulation	42
5.2.1	CBF Generation	42
5.2.2	Reduced Matrix Implementation	43
5.3	Acceleration Techniques	46
5.3.1	Lorentz Reciprocity	46
5.3.2	Translation Symmetry	47
5.3.3	The Adaptive Cross Approximation (ACA)	47
5.3.4	Fast Matrix Generation and Solution	49
5.4	The MEDM with and without the Efficiency Enhancement Techniques (EETs)	49
5.4.1	Scattering From a Dielectric Sphere	51
5.4.2	Scattering From a Small Plate	52
5.4.3	Scattering From a Small Dielectric Cube	53
5.4.4	Solution to Electrically Large Problems for MEDM	54
5.5	Conclusions	56
6	Numerical Results	57
6.1	Substrate Measurement System (SMS)	57
6.1.1	Measurement Setup	57
6.1.2	The Principle of the Measurement Technique	58
6.1.3	Objective (Cost) Function	62

6.1.4	Measurement Results	63
6.2	A Realistically Large Radome Simulation	64
6.2.1	Antenna Array Beam	64
6.2.2	Numerical Results	65
6.3	Conclusions	71
7	Conclusions and Recommendations	73
7.1	Conclusions	73
7.2	Recommendations	75
A	Field in the Center of the Cube	77
A.1	Scattered Field Evaluation	77
A.2	Contribution of the Second Taylor Term	81
B	Field of an Infinitesimal Dipole	83

Preface

The work presented in this Master Thesis has been performed towards the partial fulfillment of a Master of Science degree in Communications Engineering, with specialization in research (60 credits Master Thesis project, and one advanced level course) from the signals and systems research school at the Chalmers University of Technology. The work has been financed by the Netherlands Organization for Scientific Research (NWO), The Netherlands, and the Onsala Space Observatory, Sweden. The research has been carried out at the Netherlands Institute for Radio Astronomy (ASTRON), The Netherlands. The work has been examined and closely supervised by Prof. Per-Simon Kildal and Dr. Rob Maaskant, respectively. Prof. Per-Simon Kildal is the head of antenna group at the Chalmers University of Technology, while Dr. Rob Maaskant is a Postdoctoral researcher in the same group. The thesis has been co-supervised by Mr. Dion Kant, who is the head of the system design and integration group at ASTRON. The thesis work was carried out from November 1st, 2010, until October 11th, 2011.

List of Acronyms¹

Acronym	Definition
MoM	Method of Moments
FEM	Finite Element Method
FDTD	Finite Difference Time Domain
HFSS	High Frequency Structure Simulator (FEM-based software)
FEKO	Field Calculations for Bodies with Arbitrary Surface (MoM-based software)
CAESAR	Computationally Advanced and Efficient Simulator for ARrays (MoM-based software)
SKA	Square Kilometre Array
EFIE	Electric Field Integral Equation
MWR	Method of Weighted Residuals
MEDM	Method of Equivalent Dipole Moments
CBFM	Characteristic Basis Function Method
ACA	Adaptive Cross Approximation
SVD	Singular Value Decomposition
MRHS	Multiple Right Hand Side
EET	Efficiency Enhancement Technique

¹Acronyms are listed progressively as they appear in the text

Chapter 1

Introduction

The introduction and the contextual background of the problem is discussed in this chapter. An overview of the pros and cons incurred by the use of a radome is made. The feasibility of obtaining a numerical solution as well as the most popular techniques in computational electromagnetics are described. The need for a computationally efficient and accurate tool is discussed, after which the developed and employed techniques in this thesis are described. Finally, the organization of the thesis is provided.

1.1 Background Information

A radome is used primarily to protect the antenna against climate changes, such as humidity and temperature variations [1, Chapter 14]. However, the presence of a radome may also cause the incident electromagnetic waves to scatter in various undesired directions, which, in turn, affects the antenna radiation pattern. Furthermore, the power absorption losses may increase and, as a result, the system noise temperature as well. Ideally, a radome must therefore be transparent for electromagnetic waves or be accounted for in the design otherwise. Most commonly, a radome is therefore made from a thin material with a low effective permittivity to minimize the electromagnetic interaction between the antenna and the radome. Neglecting the influence of the radome eases the antenna design; however, it is still of importance to quantify the actual absorption losses and the scattering of (possibly shaped and multilayer) radomes to indeed demonstrate that the impedance

and radiation characteristics of antennas are barely affected by such objects.



Figure 1.1: An artist's impression (Xilostudios) of the manner in which aperture array tiles in the square kilometer array can be positioned in the field and be protected by radomes [2].

The Square Kilometer Array (SKA) is a future radio telescope, planned to be operational in 2020, with an effective area A_{eff} exceeding 30 times that of the most sensitive radio telescope currently in operation. The SKA will reveal the dawn of galaxy formation, as well as many other new discoveries in the science field called radio astronomy [2, 3]. Fig. 1.1 shows an artistic impression of a SKA station with dishes surrounding the central area made up by aperture array antenna tiles. Each tile consists of a number of antenna elements controlled by a digital beamforming module to image the sky through multiple beams as depicted in Fig. 1.2.

Often, the antenna's radiation pattern is computed in the absence of a radome, however, when a radome is used to protect the antenna elements it can cause beam pointing and beam shaping errors if the radome has not been taken into account directly during the electrical design of the antenna. The magnitude of these errors generally depend on the beam-steering direction, shape and dielectric properties of the radome.

From the above discussion, it is inferred that the effect of a radome can be significant and must therefore be taken into account when an accurate computation of the radiation pattern of the antenna is required. Existing general-purpose electromagnetic software tools employing the conventional Method of Moments (MoM), the Finite Element Method (FEM), or the Finite Difference Time Domain (FDTD), are severely limited in solving

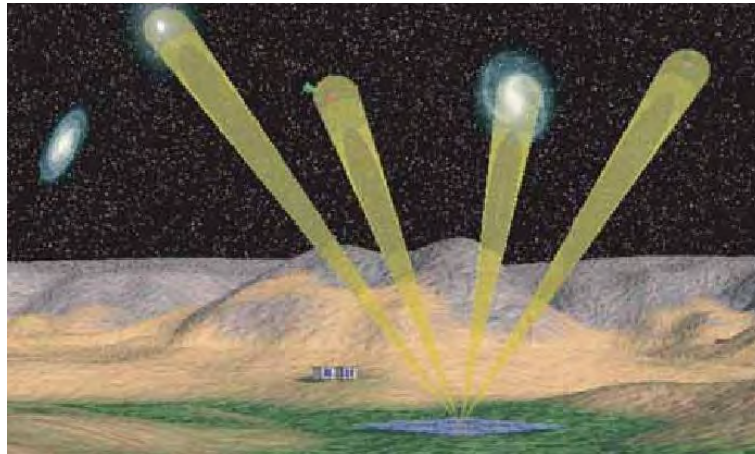


Figure 1.2: Electronic sky survey using multiple beams through digital beamforming [2].

large complex problems accurately and fast. A number of research papers has appeared in recent years on the development of efficient computational electromagnetic methods to reduce the computational cost, while maintaining high accuracy. Nonetheless, further research is on the go; a few contributions towards the development of electromagnetic methods, for including radomes in a MoM setting, can be found in [4, 5].

1.2 Brief Review of Computational Electromagnetic Methods

When designing electromagnetic instrumentation, the exact solution of the corresponding mathematical EM model is desired but not always achievable. In general, the solution error is left on behalf of the physical modeling (geometrical approximation) and/or mathematical modeling (discretization) error. Furthermore, it is time and resource demanding to calculate the solution of Maxwell's equations for large complex problems with minimal error. In order to overcome the limited computational resource capacity of computers, numerically efficient techniques are applied which alleviate the computational burden while being capable to approximate the exact solution with minimal error.

Since the scope of existing computational methods is vast, we discuss here only a few widely recognized computational methods. Thorough exposition of these methods can be found in computational electromagnetics text books [6–8]. In short, the most commonly

applied methods are:

- **FDTD (Finite Difference Time Domain)** [9] discretizes Maxwell's time-dependent curl equations and approximates the field solution iteratively. A few salient features of this method include parallelizability and simplicity; however the FDTD alone is not very attractive for solving electrically large problems or to handle slowly decaying transients due to a maximum allowable time step during each iteration needed for obtaining a stable scheme (Courant criterion), while requiring large number of time steps at the same time to obtain a convergent result. The latter can also result in round-off errors.
- **FEM (Finite Element Method)** [6] sets the weighted residual of Maxwell's curl equations to zero to solve for the unknown set of expansion coefficients. A few nice attributes include the ability to deal with complex structures and the ability to handle dispersive media, while a major disadvantage of a straight forward implementation is the extensive computation time and memory complexity, particularly for open-boundary problems.
- **MoM (Method of Moments)** [10] forms a set of equations through discretizing a boundary or volume integral equation for the surface or volume current, respectively, by imposing boundary conditions on the electric and/or magnetic field. It has the ability to handle dispersive media but is not well suited for complex problems employing non-uniform media.

The above methods can be formulated in both the time and frequency domain. Generally, frequency domain methods are more accurate, while time domain methods can handle nonlinear problems. Despite there has been prolific research towards the development of computational methods, available commercial software tools are multi-purposes codes and are therefore not very attractive for solving certain specific problems. For instance, HFSS [11] rapidly loses its efficiency as the computational domain of the problem grows large; and FEKO [12] can handle much larger problems but is still not very suitable to deal with large finite antenna arrays. Recently, Dr. Maaskant has developed a MoM-based simulator named CAESAR for the analysis of large antenna arrays for the SKA (cf., Fig. 1.1), while maintaining high computational accuracy and efficiency [13], even for problems up-to tens of wavelengths in size.

In this thesis, we implement the recently introduced method of equivalent dipole moments [14] for the scattering and absorption of electromagnetic waves from and inside dielectric objects, respectively. In that formulation, the volumetric polarization currents inside the dielectric body are replaced by equivalent dipole moments (cf., Chapter 3) whose weights are determined through enforcing a consistency condition for the electric fields inside the dielectric body.

An advantageous feature of this novel method is that it superimposes analytical scattered-field solutions of canonical structures for modeling the total scattered field of an arbitrarily-shaped object. These elementary scattered fields are non-singular when approaching the distributed source current, in fact; they are of the same order as the incident field, (i.e., of order one). As a result, the method does not suffer from the singularities encountered in conventional method of moment approaches that are based on Green's function approaches, where a superposition is made of the fields generated by infinitely small concentrated current sources. Furthermore, the method is relatively easy to implement, particularly because the basis functions for the current are electrically small and can therefore be of low order.

1.3 Organization of the Thesis

This thesis is organized as follows:

- Chapter 2 discusses the mathematical formulation of the problem, Maxwell's equations, and the proposed computational method.
- Chapter 3 includes a brief discussion on the basis and weighting functions employed in this thesis. The self-term (radiated electric field weighted over the source current) is computed analytically for the employed basis functions, while the dipole moment representation of these basis functions is used for computing the scattered field at neighboring observation cubes external to the source cubes.
- Chapter 4 describes the analytical Mie-series solution that has been implemented for solving scattering problems of dielectric spheres. In addition, the HFSS results are used as reference solutions.

- Chapter 5 describes the procedure to numerically generate a generalized set of macro-level basis functions, their application for generating a reduced matrix equation, and—in conjunction with that—a number of efficiency enhancement techniques. Validation of the method performed for several scattering problems.
- Chapter 6 describes a measurement procedure to determine the dielectric properties of some radome materials used for the eleven feed antenna [15]. Accordingly, the influence of a radome covering an array of dipoles is examined.
- Chapter 7 concludes the work, and recommendations are provided for future improvements and extensions of the software.

Chapter 2

The Method of Equivalent Dipole Moments (MEDM)

In this chapter, we discuss some fundamentals of electromagnetics and develop a mathematical formulation for the problem as discussed in Chapter 1. The volume equivalence principle is invoked and the Electric Field Integral Equation (EFIE) is formulated to determine the equivalent currents inside the dielectric volume. The EFIE is discretized through the method of weighted residuals using Galerkin's method, which then leads to a moment matrix equation that can be solved for the unknown current.

2.1 Introduction

In this chapter, we will consider the scattering and the absorption of a dielectric body of arbitrary shape. The problem is solved through the method-of-moments by employing micro-domain basis functions for the electric current. The support of these basis functions is one to two orders smaller in terms of wavelength than the typically employed basis functions with edge length $\lambda/10$. The advantageous feature is that the radiated field of a micro-basis function simply equals the field of an electrically small dipole and, hence, this field is known in analytic form. As a result, this significantly eases the computation of the moment-matrix elements since all the matrix elements, including the self-term whose field is tested inside the canonical object, can be computed analytically. To some extent, the proposed method

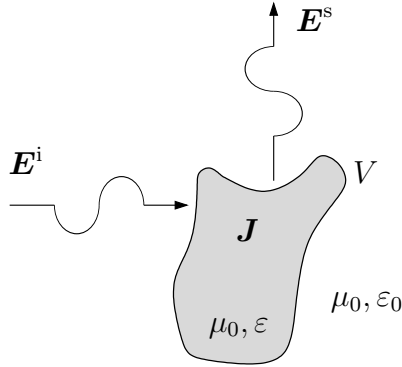


Figure 2.1: The scattering from a dielectric object of arbitrary shape.

bypasses the Green's function approach as the method employs distributed currents as basis functions as opposed to infinitely small concentrated ones. The high-resolution basis functions have the potential to accurately model the fine features in the current resulting in accurate loss computations. Furthermore, it does not suffer from the low-frequency breakdown problem, and enables us to solve problems involving a mixture of conductor and dielectric materials with little to no modification to the formulation.

2.2 Mathematical Problem Formulation

Fig. 2.1 depicts a dielectric domain of arbitrary shape occupying a volume V . The object is made of dielectrics with constitutive parameters $\{\mu_0, \varepsilon\}$ and is placed in free space $\{\mu_0, \varepsilon_0\}$. Furthermore, $k = \omega\sqrt{\mu_0\varepsilon}$ is the wavenumber of the interior medium. The object is illuminated by an electric field \mathbf{E}^i which induces an electric current \mathbf{J} inside the object. The scattered field is denote by \mathbf{E}^s . Our objective is to compute the induced current inside this dielectric object, whose solution will be synthesized indirectly by electrically small *micro-basis functions*. Another major advantage of taking an electrically small basis functions is that the associated radiated field can be computed in closed form. When the problem size becomes unmanageable, larger-domain basis functions can be constructed from smaller ones through a multi-level approach. A monolevel approach is discussed in Chapter 5.

With reference to Fig. 2.1, the relation between the incident field \mathbf{E}^i , the total electric current \mathbf{J} , the medium parameters ε and ε_0 , and the scattered electric field \mathbf{E}^s is readily

found from Maxwell's equations.

In frequency domain, Maxwell's equations for the fields and currents inside the volume V of homogeneously-filled dielectrics are given by [16]

$$\nabla \times \mathbf{E} = -j\omega\mu_0\mathbf{H}, \quad (2.1a)$$

$$\nabla \times \mathbf{H} = \mathbf{J}_{\text{prim}} + j\omega\varepsilon\mathbf{E}, \quad (2.1b)$$

$$\nabla \cdot \mathbf{H} = 0, \quad (2.1c)$$

$$\nabla \cdot \mathbf{E} = \rho/\varepsilon, \quad (2.1d)$$

where

$$\begin{aligned} \mathbf{E}(\mathbf{r}, \omega) & \text{ is called the } \textit{electric field strength} \text{ [Vm}^{-1}\text{]}, \\ \mathbf{H}(\mathbf{r}, \omega) & \text{ is called the } \textit{magnetic field strength} \text{ [Am}^{-1}\text{]}, \\ \mathbf{J}_{\text{prim}}(\mathbf{r}, \omega) & \text{ is called the impressed } \textit{electric current density} \text{ [Am}^{-2}\text{]}, \\ \mathbf{J} = \mathbf{J}_{\text{prim}} + j\omega\varepsilon\mathbf{E} & \text{ is called the total } \textit{electric current density} \text{ [Am}^{-2}\text{]}, \\ \rho(\mathbf{r}, \omega) & \text{ is called the } \textit{electric charge density} \text{ [Asm}^{-3}\text{]}. \end{aligned}$$

In the equations above, we have used that the complex-valued permittivity $\varepsilon = \varepsilon_0\varepsilon_r - j\sigma/\omega$, where σ is the conductivity of the medium.

2.2.1 The Volume Equivalence Principle

The volume equivalence principle is used here to replace the dielectric medium by vacuum, which can be done if the total current \mathbf{J} is replaced by an equivalent current \mathbf{J}_{eq} which is radiating in free space and gives rise to the correct scattered field \mathbf{E}^s [17, pp. 327,328]. In fact, it is easily seen that the right-hand side of (2.1b) can be written as

$$\mathbf{J}_{\text{prim}} + j\omega\varepsilon\mathbf{E} = \mathbf{J}_{\text{prim}} + j\omega(\varepsilon - \varepsilon_0)\mathbf{E} + j\omega\varepsilon_0\mathbf{E} = \mathbf{J}_{\text{eq}} + j\omega\varepsilon_0\mathbf{E}, \quad (2.2)$$

where

$$\mathbf{J}_{\text{eq}} = \mathbf{J}_{\text{prim}} + j\omega(\varepsilon - \varepsilon_0)\mathbf{E} \quad (2.3)$$

is the equivalent current, which includes the primary impressed, the polarization, and conduction currents. Upon substituting (2.2) in (2.1b), one readily observes that the

equivalent current \mathbf{J}_{eq} is radiating in free space. i.e.,

$$\nabla \times \mathbf{E} = -j\omega\mu_0\mathbf{H}, \quad (2.4a)$$

$$\nabla \times \mathbf{H} = \mathbf{J}_{\text{eq}} + j\omega\varepsilon_0\mathbf{E}, \quad (2.4b)$$

$$\nabla \cdot \mathbf{H} = 0, \quad (2.4c)$$

$$\nabla \cdot \mathbf{E} = \rho_{\text{eq}}/\varepsilon_0, \quad (2.4d)$$

where ρ_{eq} is related via the continuity equation for charges and currents as $\nabla \cdot \mathbf{J}_{\text{eq}} = -j\omega\rho_{\text{eq}}$. The above equations are known as the free-space Maxwell's equations. Hence, we have removed the dielectric by incorporating its presence into the equivalent current \mathbf{J}_{eq} . This is generally referred to as the *volume equivalence principle* and illustrated graphically in Fig. 2.2. In our configuration, the total electric field \mathbf{E} is the superposition of the incident

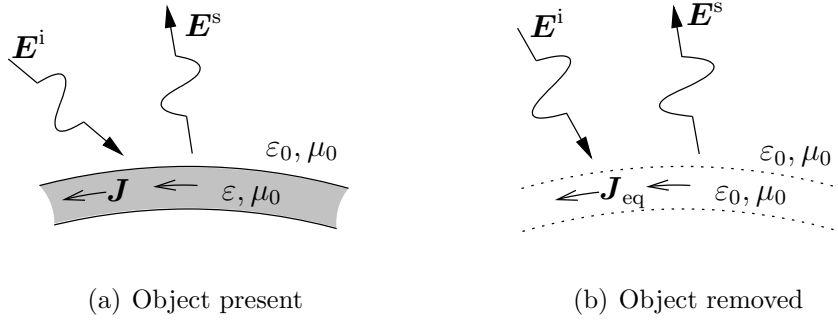


Figure 2.2: The Volume Equivalence Principle.

and scattered field \mathbf{E}^i and \mathbf{E}^s , i.e., $\mathbf{E} = \mathbf{E}^i + \mathbf{E}^s(\mathbf{J}_{\text{eq}})$, where the scattered field is generated by the equivalent current \mathbf{J}_{eq} radiating in free space. Using that $\mathbf{E} = \mathbf{E}^i + \mathbf{E}^s(\mathbf{J}_{\text{eq}})$ in (2.3), we conclude that the fields and currents inside the dielectric domain must satisfy the relation

$$\mathbf{J}_{\text{eq}} = \mathbf{J}_{\text{prim}} + j\omega(\varepsilon(\mathbf{r}) - \varepsilon_0) [\mathbf{E}^i(\mathbf{r}) + \mathbf{E}^s(\mathbf{J}_{\text{eq}})], \quad (2.5)$$

which is the *consistency condition* for the electric field and currents everywhere throughout \mathbb{R}^3 . Assuming that the object in Fig. 3.1 has no internal sources, (2.5) simplifies to

$$\mathbf{J}_{\text{eq}} = j\omega(\varepsilon - \varepsilon_0)[\mathbf{E}^i(\mathbf{r}) + \mathbf{E}^s(\mathbf{J}_{\text{eq}})], \quad \mathbf{r} \in V. \quad (2.6)$$

2.2.2 The Electric-Field Integral Equation (EFIE)

Equation (2.6) can be formulated as an integral equation for the unknown electric current \mathbf{J}_{eq} . To demonstrate this, we need to develop the integral representation of the scattered

electric field \mathbf{E}^s as a function of the current \mathbf{J}_{eq} [18].

To this end, we proceed with (2.4a) and (2.4b) as described in [13]. Because \mathbf{H} is solenoidal [$\nabla \cdot \mathbf{H} = 0$ in (2.4)], we can express this field in terms of a magnetic vector potential \mathbf{A} , i.e.,

$$\mathbf{H} = \nabla \times \mathbf{A}. \quad (2.7)$$

Substituting this equation in (2.4a) and (2.4b), we get

$$\nabla \times (\mathbf{E} + j\omega\mu_0\mathbf{A}) = \mathbf{0}, \quad (2.8a)$$

$$\nabla \times \nabla \times \mathbf{A} = \mathbf{J}_{\text{eq}} + j\omega\varepsilon_0\mathbf{E}. \quad (2.8b)$$

The curl in (2.8a) is operating on a conservative (irrotational) vector field. Hence the general solution to (2.8a) can be formulated mathematically as

$$\mathbf{E} = -j\omega\mu_0\mathbf{A} - \nabla\Phi, \quad (2.9)$$

where Φ is an electric scalar potential, yet to be determined. Substituting (2.9) in (2.8b), and utilizing the vector identity $\nabla \times \nabla \times \mathbf{A} = \nabla(\nabla \cdot \mathbf{A}) - \nabla^2\mathbf{A}$, leads to the following result

$$\nabla^2\mathbf{A} + k_0^2\mathbf{A} = -\mathbf{J}_{\text{eq}} + \nabla(\nabla \cdot \mathbf{A} + j\omega\varepsilon_0\Phi), \quad (2.10)$$

where $k_0 = \omega\sqrt{\mu_0\varepsilon_0}$. The vector field \mathbf{A} is defined uniquely if both its curl and divergence are specified, provided that \mathbf{A} is known in a single point or vanishes at infinity. With reference to definition (2.7), and in view of (2.10), it is advantageous to set

$$\nabla \cdot \mathbf{A} = -j\omega\varepsilon_0\Phi, \quad (2.11)$$

which is known as Lorentz gauge. Upon substituting this result in (2.10), one arrives at the inhomogeneous Helmholtz wave equation

$$\nabla^2\mathbf{A} + k_0^2\mathbf{A} = -\mathbf{J}_{\text{eq}}, \quad (2.12)$$

which can be solved for a given forcing function \mathbf{J}_{eq} . The radiation condition imposed on \mathbf{A} at infinity requires that only outward traveling wave solutions are physically possible. It can be shown that the well-known general solution to (2.12) is [19, pp. 78-80]

$$\mathbf{A}(\mathbf{r}) = \iiint_V G(\mathbf{r} - \mathbf{r}')\mathbf{J}_{\text{eq}}(\mathbf{r}') dV', \quad (\mathbf{r} \text{ outside } V), \quad (2.13)$$

with the scalar free-space Green's function $G = \exp(-jk_0R)/(4\pi R)$ and $R = |\mathbf{r} - \mathbf{r}'|$. Upon taking the divergence of (2.9), and by using (2.11) as well as that $\nabla \cdot \mathbf{E} = \rho/\varepsilon_0$, one

readily arrives at the inhomogeneous wave equation for the electric scalar potential, which reads

$$\nabla^2 \Phi + k_0^2 \Phi = -\frac{\rho}{\varepsilon_0}, \quad (2.14)$$

and has the generic solution

$$\Phi(\mathbf{r}) = \frac{1}{\varepsilon_0} \iiint_V G(\mathbf{r} - \mathbf{r}') \rho(\mathbf{r}') dV'. \quad (2.15)$$

Substituting the continuity equation $\nabla' \cdot \mathbf{J}_{\text{eq}}(\mathbf{r}') = -j\omega\rho(\mathbf{r}')$ in the above expression for Φ , we get

$$\Phi(\mathbf{r}) = -\frac{1}{j\omega\varepsilon_0} \iiint_V G(\mathbf{r} - \mathbf{r}') \nabla' \cdot \mathbf{J}_{\text{eq}}(\mathbf{r}') dV'. \quad (2.16)$$

By substituting (2.16) and (2.13) in (2.9), the radiated free-space electric field \mathbf{E}^s is determined as

$$\begin{aligned} \mathbf{E}^s(\mathbf{r}, \mathbf{J}_{\text{eq}}) = & -j\omega\mu_0 \iiint_V \mathbf{J}_{\text{eq}}(\mathbf{r}') \frac{e^{-jk_0|\mathbf{r}-\mathbf{r}'|}}{4\pi|\mathbf{r}-\mathbf{r}'|} dV' \\ & - \frac{1}{j\omega\varepsilon_0} \iiint_V \nabla' \cdot \mathbf{J}_{\text{eq}}(\mathbf{r}') \nabla' \left(\frac{e^{-jk_0|\mathbf{r}-\mathbf{r}'|}}{4\pi|\mathbf{r}-\mathbf{r}'|} \right) dV'. \end{aligned} \quad (2.17)$$

The EFIE is obtained by substituting (2.17) in (2.6), i.e.,

$$\begin{aligned} \mathbf{J}_{\text{eq}} = & j\omega(\varepsilon - \varepsilon_0) \left[\mathbf{E}^i(\mathbf{r}) - j\omega\mu_0 \iiint_V \mathbf{J}_{\text{eq}}(\mathbf{r}') \frac{e^{-jk_0|\mathbf{r}-\mathbf{r}'|}}{4\pi|\mathbf{r}-\mathbf{r}'|} dV' \dots \right. \\ & \left. - \frac{1}{j\omega\varepsilon_0} \iiint_V \nabla' \cdot \mathbf{J}_{\text{eq}}(\mathbf{r}') \nabla' \left(\frac{e^{-jk_0|\mathbf{r}-\mathbf{r}'|}}{4\pi|\mathbf{r}-\mathbf{r}'|} \right) dV' \right]. \end{aligned} \quad (2.18)$$

The exact solution to the above equation can only be found analytically in a few cases e.g., through Wiener-Hopf techniques. However, there exist a number of numerical techniques to find the approximate solution to the EFIE in (2.18). One of those techniques is discussed in the next section.

2.3 The Method of Weighted Residuals (MWR)

The MWR is an approximation technique for solving differential and integral equations [20]. Using the MWR, an approximate solution is constructed for the current as a linear combination of known basis functions for the current with unknown expansion coefficients.

These unknown coefficients can be obtained by solving a matrix equation, which is formed through testing the EFIE in (2.18) at least at an equal number of test points as the number of basis functions. The MWR can be further classified into many sub-methods depending on the choice of testing functions. Among the most well-known techniques, we mention the collocation method, and Galerkin method [7].

At this moment, we proceed generally and discretize (2.18) by expanding the current \mathbf{J}_{eq} as follows [10]:

$$\mathbf{J}_{\text{eq}} = \sum_{n=1}^N \alpha_n \mathbf{f}_n(\mathbf{r}), \quad (2.19)$$

where \mathbf{f}_n are the N basis functions and $\{\alpha_n\}_{n=1}^N$ is the corresponding set of N expansion coefficients. Detailed mathematical studies exist for the appropriate selection of basis and test functions for certain formulations involving integro-differential operators [21]. A modest exposition about this is made in the next chapter, or can be found in detail in [17]. Herein, we only proceed with the general formalism (i.e., by not yet assuming explicit forms for the basis and test functions). Substituting (2.19) in (2.6), yields

$$\begin{aligned} \mathbf{J}_{\text{eq}} &= \sum_{n=1}^N \alpha_n \mathbf{f}_n(\mathbf{r}) \\ &= j\omega(\varepsilon - \varepsilon_0) \left[\mathbf{E}^{\text{i}}(\mathbf{r}) + \mathbf{E}^{\text{s}} \left(\sum_{n=1}^N \alpha_n \mathbf{f}_n(\mathbf{r}) \right) \right] \\ &= j\omega(\varepsilon - \varepsilon_0) \left[\mathbf{E}^{\text{i}}(\mathbf{r}) + \sum_{n=1}^N \alpha_n \mathbf{E}^{\text{s}}(\mathbf{f}_n(\mathbf{r})) \right], \end{aligned} \quad (2.20)$$

where $\{\alpha_1, \alpha_2, \dots, \alpha_N\}$ are the N unknown expansion coefficients to be determined. The next step is to test (2.20) at N points to get N equations with N unknowns, which we can then solve for the m^{th} test point ($m = 1, 2, \dots, N$). In general, one can test the above EFIE over a small region, i.e., in a weak form using the symmetric product, which is defined as,

$$\langle \mathbf{a}, \mathbf{b} \rangle = \iiint_{S_a \cap S_b} \mathbf{a} \cdot \mathbf{b} \, dV, \quad (2.21)$$

where S_a and S_b are the supports of the basis and test or weight functions a and b , respectively. Accordingly, we get,

$$\sum_{n=1}^N \alpha_n \langle \mathbf{f}_n(\mathbf{r}), \mathbf{w}_m(\mathbf{r}) \rangle = j\omega(\varepsilon - \varepsilon_0) \left[\langle \mathbf{E}^{\text{i}}(\mathbf{r}), \mathbf{w}_m(\mathbf{r}) \rangle + \sum_{n=1}^N \alpha_n \langle \mathbf{E}^{\text{s}}(\mathbf{f}_n(\mathbf{r})), \mathbf{w}_m(\mathbf{r}) \rangle \right], \quad (2.22)$$

for $m = 1, 2, \dots, N$. The vector function \mathbf{w}_m is the m^{th} weighting function with support S_m and $\mathbf{w}_m = \mathbf{0}$ outside of its support. The choice of the weighting function is also very important in terms of the accuracy of the result. As mentioned above, two important choices are Galerkin's method and the point matching method. For point matching: $\mathbf{w}_m = \delta(\mathbf{r} - \mathbf{r}_m)$, and for Galerkin's testing: $\mathbf{w}_m = \mathbf{f}_m$. Galerkin's method is known to be more accurate and leads to a well-conditioned matrix [22]. Note that, for Galerkin's method ($\mathbf{w}_m = \mathbf{f}_m$), Eq. (2.22) leads to the matrix equation

$$\mathbf{Z}\mathbf{l} = \mathbf{V}, \quad (2.23)$$

where,

$$Z_{mn} = \frac{1}{j\omega(\varepsilon - \varepsilon_0)} \langle \mathbf{f}_n(\mathbf{r}), \mathbf{f}_m(\mathbf{r}) \rangle - \langle \mathbf{E}^s(\mathbf{f}_n(\mathbf{r})), \mathbf{f}_m(\mathbf{r}) \rangle, \quad (2.24)$$

$$\mathbf{V}_m = \langle \mathbf{E}^i, \mathbf{f}_m(\mathbf{r}) \rangle. \quad (2.25)$$

Using the integral representation in (2.21), we obtain,

$$Z_{mn} = \frac{1}{j\omega(\varepsilon - \varepsilon_0)} \iiint_V \mathbf{f}_n \cdot \mathbf{f}_m \, dV - \iiint_V \mathbf{E}^s(\mathbf{f}_n) \cdot \mathbf{f}_m \, dV, \quad (2.26)$$

where the first entry in the above equation is non-zero if \mathbf{f}_n and \mathbf{f}_m partially overlap. We refer to the self-term in case \mathbf{f}_n and \mathbf{f}_m fully overlap ($m = n$). The moment matrix equation in (2.23), that is,

$$\begin{bmatrix} Z_{11} & \cdots & Z_{1N} \\ \vdots & \ddots & \vdots \\ Z_{N1} & \cdots & Z_{NN} \end{bmatrix} \begin{bmatrix} \alpha_1 \\ \vdots \\ \alpha_N \end{bmatrix} = \begin{bmatrix} \mathbf{V}_1 \\ \vdots \\ \mathbf{V}_N \end{bmatrix}, \quad (2.27)$$

can be solved using direct Gaussian elimination techniques provided that the matrix condition number is sufficiently low to obtain a unique solution [23, Sec. 2.2.4.3]. It is important to realize that, typically, the Gaussian elimination method, or any other matrix inversion technique, has a time complexity $\mathcal{O}(N^3)$, while the filling of \mathbf{Z} has complexity $\mathcal{O}(N^2)$.

The time needed to solve the equation $\mathbf{l} = \mathbf{Z}^{-1}\mathbf{V}$ can be further reduced by a number of matrix acceleration/compression techniques. A suitable technique is selected and discussed in Chapter 5.

2.4 Conclusions

In this chapter we have formulated and discretized the EFIE using the method of weighted residuals. This discretization leads to a moment matrix equation which can be solved for the unknown expansion coefficients for the current. The next step is to select a suitable and explicit form for the basis and test functions and to evaluate the moment matrix elements.

Chapter 3

Choice of Basis and Testing Functions

The choice of the basis and weighting functions in the MoM plays a key role in both the numerical solution accuracy and computational efficiency. Theoretical aspects of basis and weighting functions with a description of the restrictions on their choice are described, leading to a discussion on the implication of Galerkin and non-Galerkin moment method approaches. The microdomain basis functions are discussed with pros and cons compared to existing types of basis functions, thereby motivating our specific choice of microdomain basis functions. The self-generated field in the center of a microdomain basis function is derived analytically as well as for the field outside of the source cube. This allows us to develop expressions for the moment matrix elements are formulated in closed form.

3.1 Introduction

The choice of a suitable set of basis and weighting functions is dependent on both mathematical and physical requirements. The general discretization process through the MWR has been explained in Chapter 2, hence, the next step is to select explicit mathematical forms for the basis and weighting functions.

3.1.1 Basis Function Selection

In practice, basis functions can be classified into two types: subdomain basis functions and entire domain basis functions [17, pp. 683-689]. Subdomain basis functions are nonzero only over an electrically small part of the domain, while entire domain basis functions are nonzero over a larger or even the entire domain of the considered object. Both types of basis functions should have the ability to accurately represent or resemble the anticipated unknown function, which is the equivalent electric current \mathbf{J}_{eq} in our case. Because entire domain basis functions of an analytical type are for specific structures only and are difficult to use for forming a matrix equation (self-term), we choose to employ low-order subdomain basis functions. The size of these subdomain basis functions need to be chosen small enough to approximate the solution with sufficiently high accuracy (typically $\lambda/10$ edge length). However, we will employ so-called microdomain basis functions of edge length $\approx \lambda/100$ to obtain a potentially very accurate solution as well as an easy-to-implement discretization scheme. A microdomain basis function has been depicted in Fig. 3.1 and can be defined mathematically as follows:

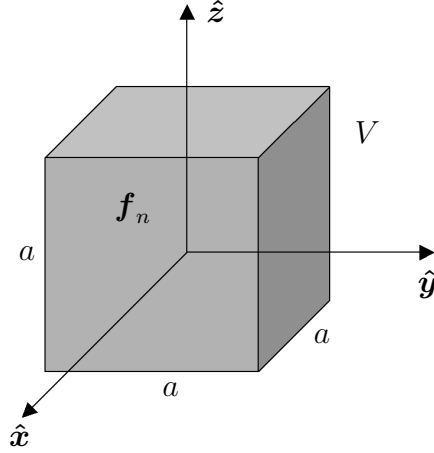


Figure 3.1: The microdomain basis function.

$$\mathbf{f}_n(\mathbf{r}) = \begin{cases} \hat{x}, & \mathbf{r} \in V_n; n \in \{1, \dots, N/3\} \\ \hat{y}, & \mathbf{r} \in V_n; n \in \{N/3 + 1, \dots, 2N/3\} \\ \hat{z}, & \mathbf{r} \in V_n; n \in \{2N/3 + 1, \dots, N\} \\ \mathbf{0}, & \mathbf{r} \notin V_n. \end{cases}$$

where V_n is the cubic support of \mathbf{f}_n with constant cube-volume a^3 and $n \in \{1, \dots, N\}$.

Although the moment matrix is larger than the case that entire-domain basis functions were to be employed, we can still solve electrically large problems by realizing that entire-domain basis functions can be expanded through a fixed combination of micro-domain basis functions (Chapter 5).

3.1.2 Selection of Weighting Functions

After the discretization of the EFIE by assuming an explicit form of the basis functions, the next step in the MWR is to select the weighting functions. The appropriate choice of the weighting functions depends on the range-space of the integro-differential operator. Without justifying the choice, we will employ Galerkin's method since this choice is known to yield accurate results for a large variety of problems [24]. In our case, however, we can also use the collocation method for testing the field, which is equivalent to Galerkin's method evaluated through the midpoint integration rule (discussed in the following section).

3.2 Computation of the Moment Matrix Elements

The procedure to compute the moment matrix elements [see (2.27)] has been described in this section. In MEDM, we employ equal sized basis functions of low order, as a result of which the self-coupling moment matrix entries are all identical and can be computed analytically. The off-diagonal matrix elements can be computed via the dipole-moment approach as explained below.

3.2.1 The Self-Term Z_{nn}

With reference to (2.24), to compute an on-diagonal matrix element Z_{nn} , we have to evaluate

$$Z_{nn} = \frac{1}{j\omega(\varepsilon - \varepsilon_0)} \langle \mathbf{f}_n(\mathbf{r}), \mathbf{f}_n(\mathbf{r}) \rangle - \langle \mathbf{E}^s(\mathbf{f}_n(\mathbf{r})), \mathbf{f}_n(\mathbf{r}) \rangle. \quad (3.1)$$

The first term in the above equation is evaluated analytically in this section as $\langle \mathbf{f}_n, \mathbf{f}_n \rangle = a^3$.

To evaluate the second term, we assume that the basis function \mathbf{f}_n is a z -directed unit current, which is supported by a cube of size $a \times a \times a$. Accordingly,

$$\mathbf{f}_n = \hat{\mathbf{z}} [U(x + a/2) - U(x - a/2)] [U(y + a/2) - U(y - a/2)] [U(z + a/2) - U(z - a/2)], \quad (3.2)$$

where the Heaviside step-function U borders the cubic support region. Before substituting (3.2) in (2.17) for computing $\mathbf{E}^s(\mathbf{f}_n)$, we first note that

$$\nabla' \left(\frac{e^{-jk_0R}}{4\pi R} \right) = (\mathbf{r} - \mathbf{r}') [1 + jk_0R] \frac{e^{-jk_0R}}{4\pi R^3}, \quad (3.3)$$

where $R = |\mathbf{r} - \mathbf{r}'|$. Upon assuming that a is electrically small, then, in the quasi-static case, $k_0R \ll 1$, so that $e^{-jk_0R} = 1 - jk_0R + \dots \approx 1$. Accordingly, we can approximate (3.3) as

$$\lim_{k_0a \rightarrow 0} \left\{ \nabla' \left(\frac{e^{-jk_0R}}{4\pi R} \right) \right\} = \frac{(\mathbf{r} - \mathbf{r}')}{4\pi R^3}. \quad (3.4)$$

Using (3.2), we have for the charge density,

$$\nabla' \cdot \mathbf{f}_n(\mathbf{r}') = [\delta(z' + a/2) - \delta(z' - a/2)], \quad (3.5)$$

which appears to exist only at the top and bottom faces of the cubic support. Substituting the preceding expressions in the quasi-static form of (2.17), yields

$$\mathbf{E}^s(\mathbf{f}_n) \approx \frac{-j\omega\mu_0\hat{\mathbf{z}}}{4\pi} \iiint_V \frac{1}{|\mathbf{r} - \mathbf{r}'|} dV' + \frac{1}{j\omega\varepsilon_04\pi} \left[\iint_{S^+} \frac{(\mathbf{r} - \mathbf{r}')}{|\mathbf{r} - \mathbf{r}'|^3} dS' - \iint_{S^-} \frac{(\mathbf{r} - \mathbf{r}')}{|\mathbf{r} - \mathbf{r}'|^3} dS' \right], \quad (3.6)$$

where S^+ and S^- are the top and bottom surfaces of the cube at $z = a/2$ and $z = -a/2$, respectively. The integrals with singular kernels in (3.6) can be solved analytically using methodologies described in [25, 26]. Following [26, Eq. (7)], we transform the volume integral in (3.6) into a surface integral, yielding

$$\iiint_V \frac{1}{|\mathbf{r} - \mathbf{r}'|} dV' = -\frac{1}{2} \iiint_V \nabla' \cdot \frac{(\mathbf{r} - \mathbf{r}')}{|\mathbf{r} - \mathbf{r}'|} dV' = \frac{1}{2} \iint_{\partial V} \hat{\mathbf{R}}' \cdot \hat{\mathbf{n}} dS', \quad (3.7)$$

where $\hat{\mathbf{R}}' = (\mathbf{r}' - \mathbf{r})/|\mathbf{r}' - \mathbf{r}|$ and where we made use of Gauss' theorem [27, pp. 193-196], that is,

$$\iiint_V \nabla \cdot \mathbf{A} dV' = \iint_{\partial V} \mathbf{A} \cdot \hat{\mathbf{n}} dS', \quad (3.8)$$

with the normal vector $\hat{\mathbf{n}}$ pointing outwards. The most obvious choice is to test the E -field, given by (2.5) in the center of the cube, that is, at $\mathbf{r} = \mathbf{0}$. Along with (3.7), Eq. (3.6) reduces to

$$\mathbf{E}^s(\mathbf{f}_n)|_{\mathbf{r}=\mathbf{0}} = \frac{-j\omega\mu_0\hat{\mathbf{z}}}{8\pi} \iint_{\partial V} \hat{\mathbf{r}}' \cdot \hat{\mathbf{n}} \, dS' + \frac{1}{j\omega\varepsilon_0 4\pi} \left[\iint_{S^-} \frac{\hat{\mathbf{r}}'}{r'^2} \, dS' - \iint_{S^+} \frac{\hat{\mathbf{r}}'}{r'^2} \, dS' \right], \quad (3.9)$$

where $r' = |\mathbf{r}'|$, and where $\hat{\mathbf{r}}' = \mathbf{r}'/r'$. This expression can be evaluated analytically to yield (see Appendix A)

$$\mathbf{E}^s(\mathbf{r} = \mathbf{0}, \mathbf{f}_n) = \hat{\mathbf{z}} \left[-j\omega\mu_0 a^2 \left[\frac{3}{4\pi} \ln \left(\frac{\sqrt{3}+1}{\sqrt{3}-1} \right) + \frac{3}{2\pi} a^2 \arctan \left(\frac{1}{\sqrt{3}} \right) - \frac{3}{8} \right] - \frac{1}{j\omega\varepsilon_0} \left[1 - \frac{4}{\pi} \arctan \left(\frac{1}{\sqrt{3}} \right) \right] \right]. \quad (3.10)$$

Note that this result is valid if we account for only one Taylor term in (3.4) when approximating $e^{-jk_0 R}$. Taking also the second Taylor term $-jk_0 R$ into account (see Appendix A.2) yields,

$$\mathbf{E}^s(\mathbf{r} = \mathbf{0}, \mathbf{f}_n) = \hat{\mathbf{z}} \left[\frac{-\omega\mu_0 k_0}{4\pi} a^3 - j\omega\mu_0 a^2 \left[\frac{3}{4\pi} \ln \left(\frac{\sqrt{3}+1}{\sqrt{3}-1} \right) + \frac{3}{2\pi} a^2 \arctan \left(\frac{1}{\sqrt{3}} \right) - \frac{3}{8} \right] - \frac{1}{j\omega\varepsilon_0} \left[1 - \frac{4}{\pi} \arctan \left(\frac{1}{\sqrt{3}} \right) \right] \right], \quad (3.11)$$

which shows that the approximation error, when taking only one Taylor term into account, is $\omega\mu_0 k_0 a^3/4\pi$. This finalizes the formulation of the self-generated field for a z -polarized basis function current. The unit vector $\hat{\mathbf{z}}$ can be replaced by $\hat{\mathbf{x}}$ or $\hat{\mathbf{y}}$ as defined in Fig. 3.1 to find the field of the other polarizations.

Upon substituting (3.11) in (2.26), and by using that $\langle \mathbf{f}_n, \mathbf{f}_n \rangle = a^3$, the expression for the self-term becomes

$$Z_{nn} = \frac{a^3}{j\omega(\varepsilon - \varepsilon_0)} - a^3 \left[\frac{-\omega\mu_0 k_0}{4\pi} a^3 - j\omega\mu_0 a^2 \left[\frac{3}{4\pi} \ln \left(\frac{\sqrt{3}+1}{\sqrt{3}-1} \right) + \frac{3}{2\pi} a^2 \arctan \left(\frac{1}{\sqrt{3}} \right) - \frac{3}{8} \right] - \frac{1}{j\omega\varepsilon_0} \left[1 - \frac{4}{\pi} \arctan \left(\frac{1}{\sqrt{3}} \right) \right] \right], \quad (3.12)$$

where, we have used the mid-point integration rule, i.e.,

$$\langle \mathbf{E}^s(\mathbf{f}_n), \mathbf{f}_n \rangle = \iiint_V \mathbf{E}^s(\mathbf{f}_n) \cdot \mathbf{f}_n \, dV \approx a^3 \mathbf{E}^s(\mathbf{f}_n(\mathbf{r}_n)) \cdot \mathbf{f}_n, \quad (3.13)$$

where \mathbf{r}_n is the centroid of the n th cube, and

$$a^3 = \iiint_{V_n} dV \quad (3.14)$$

is the volume of the n^{th} cube. As long as $k_0 a \ll 1$, we can approximate Eq. (3.12) as follows:

$$Z_{nn} \approx \frac{a^3}{j\omega(\varepsilon - \varepsilon_0)} - a^3 \left[-\frac{1}{j\omega\varepsilon_0} \left[1 - \frac{4}{\pi} \arctan\left(\frac{1}{\sqrt{3}}\right) \right] \right], \quad (3.15)$$

3.2.2 The Off-Diagonal Moment Matrix Term Z_{mn} ($m \neq n$)

The off-diagonal moment matrix entries are computed using the equivalent dipole moment approach. Using this approach, the field radiated by a basis function of uniform current is assumed to be equal to the field of an infinitesimal dipole placed at the center of this cubic support with dipole moment $Il\hat{\mathbf{f}}$, where $\hat{\mathbf{f}} \in \{\hat{\mathbf{x}}, \hat{\mathbf{y}}, \hat{\mathbf{z}}\}$. The E -field of a z -oriented dipole can be easily computed using the following analytical expressions (derived in Appendix B).

$$E_x^s = \frac{IlC}{4\pi j\omega\varepsilon_0} xze^{-jk_0|\mathbf{r}_{mn}|} \quad (3.16a)$$

$$E_y^s = \frac{IlC}{4\pi j\omega\varepsilon_0} yze^{-jk_0|\mathbf{r}_{mn}|} \quad (3.16b)$$

$$E_z^s = \frac{Il}{4\pi j\omega\varepsilon_0} \left[C_{mn}z^2 + \frac{k_0^2}{|\mathbf{r}_{mn}|} - \frac{jk_0}{|\mathbf{r}_{mn}|^2} - \frac{1}{|\mathbf{r}_{mn}|^3} \right] e^{-jk_0|\mathbf{r}_{mn}|}, \quad (3.16c)$$

where

$$C_{mn} = -\frac{k_0^2}{|\mathbf{r}_{mn}|^3} + \frac{3jk_0}{|\mathbf{r}_{mn}|^4} + \frac{3}{|\mathbf{r}_{mn}|^5}. \quad (3.17)$$

Substituting (3.16) in (2.26), and using that $\mathbf{f}_n \cdot \mathbf{f}_m = 0$ ($\forall m \neq n$), we get for a z -oriented basis function current

$$\mathbf{Z}_{mn} = -a^3 [E_x^s \hat{\mathbf{x}} + E_y^s \hat{\mathbf{y}} + E_z^s \hat{\mathbf{z}}] \cdot \mathbf{f}_m. \quad (3.18)$$

Here, \mathbf{Z}_{mn} is the electric field tested by the m th basis function which is radiated by the n th basis function current, which is assumed to be z -oriented.

It will be demonstrated numerically in Sec. 4.4 that a single dipole is indeed sufficient to accurately represent the external field of a microdomain basis function. This is done through a convergence analysis for the external E -field by subdividing the source cube into smaller subcubes.

In the following we will justify that we can choose for the strength of above dipole moment that $Il = a^3$. By substituting (2.11) in (2.9), we have that

$$\mathbf{E} = \frac{1}{j\omega\epsilon_0} [\nabla(\nabla \cdot \mathbf{A}) + k_0^2 \mathbf{A}]. \quad (3.19)$$

The magnetic vector potential \mathbf{A} in (2.13) can be evaluated for $\mathbf{f}_n(\mathbf{r}') = Il\hat{\mathbf{z}}\delta(x')\delta(y')\delta(z')$ as

$$\begin{aligned} \mathbf{A} &= \iiint_V \mathbf{f}_n(\mathbf{r}') \frac{e^{-jk_0|\mathbf{r}-\mathbf{r}'|}}{4\pi|\mathbf{r}-\mathbf{r}'|} dV' \\ &= \frac{Il}{4\pi} \hat{\mathbf{z}} \frac{e^{-jk_0|\mathbf{r}|}}{|\mathbf{r}|}. \end{aligned} \quad (3.20)$$

Substituting (3.20) in (3.19) gives the field of a dipole (see Appendix B) which is then tested at the observation cube to get \mathbf{Z}_{mn} . However, instead of computing the field from a dipole, we have to evaluate the actual volumetric integral in (3.20) for the basis function \mathbf{f}_n . Assuming a cube of z -oriented uniform current

$$\mathbf{f}_n(\mathbf{r}) = \begin{cases} \hat{\mathbf{z}}, & \mathbf{r} \in V_n \\ \mathbf{0}, & \mathbf{r} \notin V_n, \end{cases} \quad (3.21)$$

where $V_n = a^3$ represents the volume of the source cube. Using (3.21) in (3.20), yields

$$\mathbf{A} = \int_{-a/2}^{a/2} \int_{-a/2}^{a/2} \int_{-a/2}^{a/2} \hat{\mathbf{z}} \frac{e^{-jk_0|\mathbf{r}-\mathbf{r}'|}}{4\pi|\mathbf{r}-\mathbf{r}'|} dV'.$$

Then, using the mid-point integration rule,

$$\iiint_{V_n} \mathbf{f}(\mathbf{r}') dV' = V_n \mathbf{f}(\mathbf{r}_0) = a^3 \mathbf{f}(\mathbf{r}_0),$$

where $\mathbf{r}_0 = (\mathbf{0}, \mathbf{0}, \mathbf{0})$ is the center point of the cube, and V_n is the cube volume, we obtain

$$\begin{aligned} \mathbf{A} &= \int_{-a/2}^{a/2} \int_{-a/2}^{a/2} \int_{-a/2}^{a/2} \hat{\mathbf{z}} \frac{e^{-jk_0|\mathbf{r}-\mathbf{r}'|}}{4\pi|\mathbf{r}-\mathbf{r}'|} dV' \\ &= \frac{a^3}{4\pi} \hat{\mathbf{z}} \frac{e^{-jk_0|\mathbf{r}|}}{|\mathbf{r}|}, \end{aligned} \quad (3.22)$$

which shows that taking a dipole in (3.20) to represent the scattered field is equivalent to using a mid-point integration rule for evaluating \mathbf{A} using the actual volumetric current distribution, provided that $Il = a^3$. Conclusively, subdividing the source cube into smaller sub cubes each of which contains a dipole with associated dipole moment will therefore yield the same total radiated field as evaluating \mathbf{A} through a composite mid-point integration rule using the actual cube supporting a uniform current.

3.3 Conclusions

In this chapter we have made our choice of basis and test functions. The equivalent dipole moment of a micro-domain basis function has been derived. The scattered field at the center of the cube has been calculated, which is needed for testing the field inside the observation cube to compute the self-term. The scattered field values in the centers of the remaining cubes (i.e., the coupling-terms) have been determined through the dipole field representation. We now have regular closed-form expressions for the moment matrix elements which can be evaluated numerically. The next step is to implement and to examine the accuracy of the herein presented formulation.

Chapter 4

Numerical Validation

The Mie-series solution is the analytical field solution for the scattering of a dielectric or conducting sphere. In this chapter, the Mie-series is formulated mathematically and validated by comparing the results for a specific problem to published data. Afterwards, the numerically computed results by using the MoM implementation as described in the previous chapter are validated and compared to the analytical Mie series solution. Furthermore, HFSS and WIPL—which are commercially available electromagnetic software tools—are then also used to compare the numerically computed results to the present MoM implementation.

4.1 Mie-Series Solution

To validate computational methods, it is important to have an analytical reference solution available to be able to determine the accuracy of the developed numerical method. The Mie-series is an important reference solution since it represents a closed-form solution of the scattered field from a dielectric or conducting sphere. In this section, we will outline the mathematical steps to derive the Mie-series; while a more detailed description on the associated series expansion methods can be found in [7, Chap. 2] or [16, Sec. 9.25].

Consider an x -polarized plane wave traveling in the positive z -direction and a sphere of radius R placed at the origin of a spherical coordinate system as depicted in Fig. 4.1.

The free-space permittivity and permeability are ε_0 and μ_0 , respectively; the permittivity and permeability of the sphere are ε and μ_0 , respectively. The propagation constant $k_2 = \omega\sqrt{\varepsilon_0\mu_0}$ is for the exterior free space medium (represented by medium 2), and $k_1 = \omega\sqrt{\varepsilon\mu_0}$ is the propagation constant of the interior sphere region (represented by medium 1).

The medium properties of the sphere are assumed to be homogeneous. Using separation

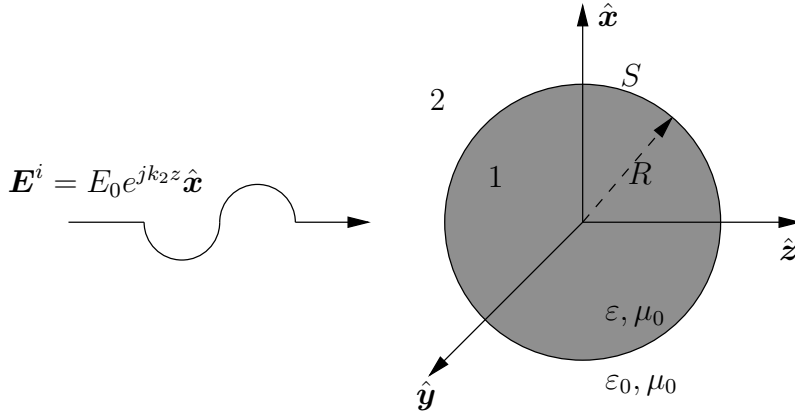


Figure 4.1: Plane wave incidence on a sphere of radius R .

of variables, the incident field can be decomposed into a sum of vector spherical wave functions j_n , as follows [16, Sec. 9.25]:

$$\mathbf{E}^i = E_0 e^{j(k_2 z - \omega t)} \hat{\mathbf{x}} = E_0 e^{-j\omega t} \sum_{n=1}^{\infty} j^n \frac{2n+1}{n(n+1)} (\mathbf{m}_E - j\mathbf{n}_E), \quad (4.1a)$$

$$\mathbf{H}^i = \frac{k_2}{\mu_0 \omega} E_0 e^{j(k_2 z - \omega t)} \hat{\mathbf{y}} = -\frac{k_2 E_0}{\mu_0 \omega} e^{-j\omega t} \sum_{n=1}^{\infty} j^n \frac{2n+1}{n(n+1)} (\mathbf{m}_H - j\mathbf{n}_H), \quad (4.1b)$$

where E_0 is the amplitude of the incident field and

$$\mathbf{m}_E = \frac{1}{\sin \theta} j_n(k_2 R) P_n^1(\cos \theta) \cos \phi \hat{\boldsymbol{\theta}} - j_n(k_2 R) \frac{\partial P_n^1}{\partial \theta} \sin \phi \hat{\boldsymbol{\phi}}, \quad (4.2a)$$

$$\mathbf{m}_H = -\frac{1}{\sin \theta} j_n(k_2 R) P_n^1(\sin \theta) \cos \phi \hat{\boldsymbol{\theta}} - j_n(k_2 R) \frac{\partial P_n^1}{\partial \theta} \cos \phi \hat{\boldsymbol{\phi}}, \quad (4.2b)$$

$$\begin{aligned} \mathbf{n}_E &= \frac{n(n+1)}{k_2 R} P_n^1(\cos \theta) \sin \phi \hat{\mathbf{r}} + \frac{1}{k_2 R} [k_2 R j_n(k_2 R)]' \frac{\partial P_n^1(\cos \theta)}{\partial \theta} \sin \phi \hat{\boldsymbol{\theta}} \\ &\quad + \frac{1}{k_2 R \sin \theta} [k_2 R j_n(k_2 R)]' P_n^1(\cos \theta) \cos \phi \hat{\boldsymbol{\phi}}, \end{aligned} \quad (4.2c)$$

$$\begin{aligned} \mathbf{n}_H &= \frac{n(n+1)}{k_2 R} P_n^1(\cos \theta) \cos \phi \hat{\mathbf{r}} + \frac{1}{k_2 R} [k_2 R j_n(k_2 R)]' \frac{\partial P_n^1(\cos \theta)}{\partial \theta} \cos \phi \hat{\boldsymbol{\theta}} \\ &\quad - \frac{1}{k_2 R \sin \theta} [k_2 R j_n(k_2 R)]' P_n^1(\cos \theta) \sin \phi \hat{\boldsymbol{\phi}}, \end{aligned} \quad (4.2d)$$

where j_n is a spherical Bessel function of the first kind and of order n , P_n^1 is the Legendre polynomial of the first kind and of order n , and the superscript $'$ represents differentiation with respect to the argument of the Bessel function (i.e., $k_2 R$). The spherical Bessel function is used to represent the standing wave in the radial direction. Analogously to the spherical Bessel function of the first kind, the spherical Bessel function of the second kind is denoted by y_n . The scattered field in medium 2 can be written as

$$\mathbf{E}^s = E_0 e^{-j\omega t} \sum_{n=1}^{\infty} j^n \frac{2n+1}{n(n+1)} (a_n^s \tilde{\mathbf{m}}_E - j b_n^s \tilde{\mathbf{n}}_E), \quad (4.3a)$$

$$\mathbf{H}^s = -\frac{k_2 E_0}{\mu_0 \omega} e^{-j\omega t} \sum_{n=1}^{\infty} j^n \frac{2n+1}{n(n+1)} (b_n^s \tilde{\mathbf{m}}_H + j a_n^s \tilde{\mathbf{n}}_H), \quad (4.3b)$$

which is valid on the boundary surface S and outside of the sphere (i.e., $R \geq a$). The functions $\tilde{\mathbf{m}}_E$, $\tilde{\mathbf{m}}_H$, $\tilde{\mathbf{n}}_E$ and $\tilde{\mathbf{n}}_H$ are obtained by replacing $j_n(k_2 R)$ by $h_n^{(1)}(k_2 R)$ in (4.2). Here, $h_n^{(1)}$ is the spherical Hankel function of the first kind and of order n , used to represent the outward-traveling spherical wave. The spherical Hankel function of the first and second kind can be obtained using the spherical Bessel functions of the first and second kind as follows:

$$h_n^{(1)} = j_n + y_n,$$

$$h_n^{(2)} = j_n - y_n.$$

It should be noted that the minus or plus signs in the above spherical Hankel function definitions of the first and second kind depend on the chosen time factor $e^{\pm j\omega t}$ [here $e^{-j\omega t}$,

since the propagation is in the positive z -direction in (4.1)]. Analogously to the scattered field, the transmitted field in medium 1 is written as

$$\mathbf{E}^t = E_0 e^{-j\omega t} \sum_{n=1}^{\infty} j^n \frac{2n+1}{n(n+1)} (a_n^t \mathbf{m}_E - j b_n^t \mathbf{n}_E), \quad (4.4a)$$

$$\mathbf{H}^t = -\frac{k_2 E_0}{\mu_0 \omega} e^{-j\omega t} \sum_{n=1}^{\infty} j^n \frac{2n+1}{n(n+1)} (b_n^t \mathbf{m}_H + j a_n^t \mathbf{n}_H). \quad (4.4b)$$

The transmitted field is valid on the boundary and the interior region of the sphere. Applying the boundary conditions to the total $\{\mathbf{E}, \mathbf{H}\}$ fields at $R = a$, gives

$$\hat{\mathbf{r}} \times (\mathbf{E}^i + \mathbf{E}^s) = \hat{\mathbf{r}} \times \mathbf{E}^t, \quad (4.5a)$$

$$\hat{\mathbf{r}} \times (\mathbf{H}^i + \mathbf{H}^s) = \hat{\mathbf{r}} \times \mathbf{H}^t, \quad (4.5b)$$

where $\hat{\mathbf{r}}$ is the outward-pointing radial unit vector on the sphere surface. Substituting the values of the incident, transmitted and scattered fields in the above boundary conditions leads to the system of inhomogeneous equations [16, Sec. 9.25]

$$a_n^t j_n(N\rho) - a_n^s h_n^{(1)}(\rho) = j_n(\rho), \quad (4.6a)$$

$$a_n^t [N\rho j_n(N\rho)]' - a_n^s [\rho h_n^{(1)}(\rho)]' = [\rho j_n(\rho)]', \quad (4.6b)$$

$$N b_n^t j_n(N\rho) - b_n^s h_n^{(1)}(\rho) = j_n(\rho), \quad (4.6c)$$

$$b_n^t [N\rho j_n(N\rho)]' - N b_n^s [\rho h_n^{(1)}(\rho)]' = N [\rho j_n(\rho)]', \quad (4.6d)$$

where $\rho = k_2 a$, $k_1 a = N\rho$ and $N = k_1/k_2$ is the refractive index of the dielectric sphere, which may be complex for lossy dielectrics. By substituting a_n^s from (4.6a) in (4.6b), the value for a_n^t is derived and vice versa for determining a_n^s ; the same analogy is used to determine b_n^t and b_n^s . This yields.

$$a_n^s = -\frac{j_n(N\rho)[\rho j_n(\rho)]' - j_n(\rho)[N\rho j_n(N\rho)]'}{j_n(N\rho)[\rho h_n^{(1)}(\rho)]' - h_n^{(1)}(\rho)[N\rho j_n(N\rho)]'}, \quad (4.7a)$$

$$b_n^s = -\frac{j_n(N\rho)[N\rho j_n(\rho)]' - N^2 j_n(\rho)[\rho j_n(\rho)]'}{h_n^{(1)}(\rho)[N\rho j_n(\rho)]' - N^2 j_n(N\rho)[\rho h_n^{(1)}(\rho)]'}, \quad (4.7b)$$

$$a_n^t = \frac{\mu_0 j_n(N\rho)[\rho h_n^{(1)}(\rho)]' - \mu_0 h_n^{(1)}(\rho)[\rho j_n(\rho)]'}{\mu_0 j_n(N\rho)[\rho h_n^{(1)}(\rho)]' - h_n^{(1)}(\rho)[N\rho j_n(N\rho)]'}, \quad (4.7c)$$

$$b_n^t = \frac{\mu_0 N j_n(N\rho)[\rho h_n^{(1)}(\rho)]' - \mu_0 N h_n^{(1)}(\rho)[\rho j_n(\rho)]'}{N^2 j_n(N\rho)[\rho h_n^{(1)}(\rho)]' - \mu_0 h_n^{(1)}(\rho)[N\rho j_n(N\rho)]'}. \quad (4.7d)$$

We now have determined the mode expansion coefficients in (4.3) and (4.4) to find the total fields inside and outside of the sphere. The field inside of the sphere can be computed using (4.4), while the field outside of the sphere is the sum of the incident, i.e. Eq. (4.1), and the scattered fields, i.e. Eq. (4.3).

4.2 Mie-Series Validation

4.2.1 Comparison With a Published Mie-Series Solution

The Mie-series, as derived mathematically in the previous section, has been implemented in Matlab and is herein validated by comparing it to a reference solution published in [28] for the scattering of the electromagnetic fields from a dielectric sphere. The specifications of the problem are as follows:

Table 4.1: Specifications for the dielectric sphere.

• x -directed plane wave	• $k_0 R = 1/2$
• $\varepsilon_r = 16$	• $\phi^i = 0$
• $\theta^i = \pi$	• $R = \lambda/4\pi$

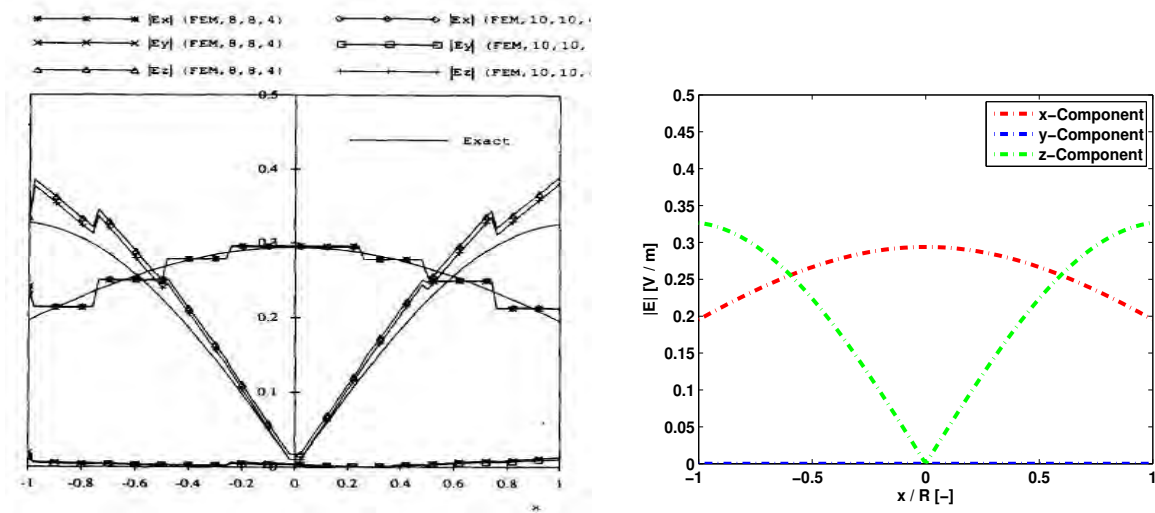
Figure 4.2 depicts the comparison between the solution of the implemented Mie-series and the published results in [28]. In [28] the hybrid MoM and FEM method has been validated by comparing it to the Mie-series solution. The analytical solution as presented in the journal paper and the one obtained by the herein implemented Mie-series, are in exact correspondence with each other. The comparison in Fig. 4.2 shows that we can proceed using our implemented Mie-series for the validation of our MoM code.

4.2.2 Mie-Series in Comparison With HFSS

In addition to the above comparison, the Mie-series solution and the numerically computed results obtained by HFSS have been compared as depicted in Fig. 4.3. The specifications of the problem are as follows:

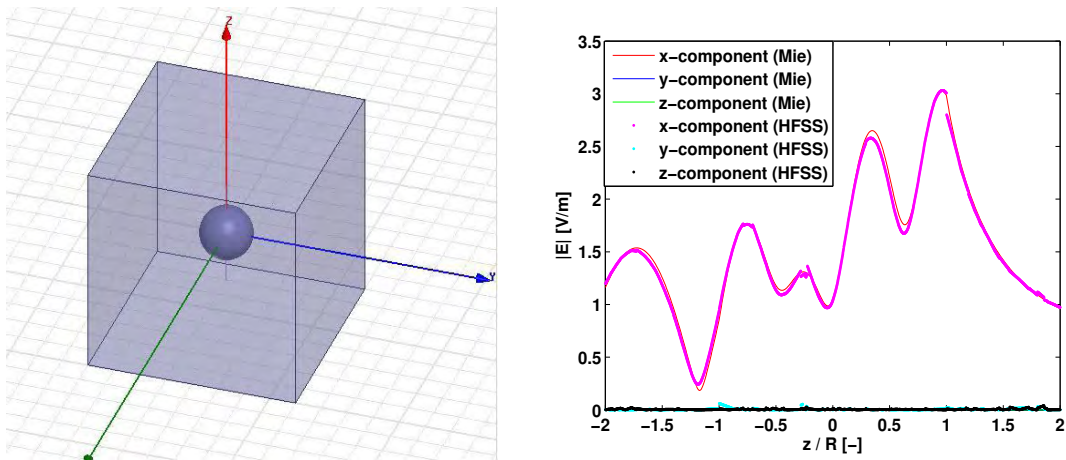
Table 4.2: Specifications for the dielectric sphere.

• x -directed plane wave	• $k_0 R = \pi$
• $\varepsilon_r = 3.55$	• $\phi^i = 0$
• $\theta^i = \pi$	• $R = \lambda/2$



(a) The hybrid MoM and FEM method in comparison with the Mie-series [28]. (b) The Mie-series solution for the magnitude of the E -Field along the x -axis.

Figure 4.2: Mie-series comparison with [28]; specifications: see Table 4.1.



(a) Problem (graphical illustration). (b) The magnitude of the E -Field along z -axis.

Figure 4.3: The Mie-series in comparison with HFSS; specifications: see Table 4.2.

Upon comparing the analytical solution to the HFSS solution, it can be observed that HFSS suffers from certain field discontinuities in the solution, particularly at the surface of the sphere, as is evident from Fig. 4.3(b). Overall, the HFSS solution is in very good agreement with the Mie-series solution with a root mean square relative error of 6.32%, for

2001 sample points, calculated using the following formula:

$$\text{Error} = \sqrt{\frac{1}{N} \sum_{n=1}^N \left| \left(\frac{E_{\text{Mie}}^n - E_{\text{HFSS}}^n}{E_{\text{Mie}}^n} \right) \right|^2} \times 100\%, \quad (4.8)$$

where N represents the total number of samples and $E = |\mathbf{E}|$.

4.3 MEDM in Comparison with Ansoft's HFSS and WIPL-D

Thus far, we have developed two reference solutions that can be used to validate MEDM, i.e., the Mie-series solution, and the commercial HFSS software. In this section, we make a comparison among Ansoft's HFSS (v 13.0), WIPL-D Pro (v 9.0) [29], and MEDM in terms of the accuracy, execution time and memory usage. For the generation of the results, an Intel Centrino laptop equipped with a dual core processor@2.2GHz and 2GB of RAM has been used; except for the sphere of radius $R = \lambda/50$, where a remote desktop server has been used equipped with a dual core processor@2.4GHz and 16GB of RAM. For the HFSS computation, a desktop server with a quad core processor@2.33GHz, has been used with 4GB of RAM memory.

4.3.1 Scattering From a Dielectric Sphere

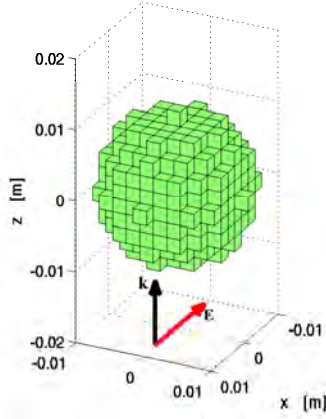
A dielectric sphere has been simulated using the HFSS, WIPL-D and MEDM software. The comparison between the results, obtained by MEDM, WIPL-D and HFSS, is depicted in Figs. 4.4 and 4.5. In HFSS, a *maximum delta energy*¹ of 0.00027 is reached for the error in the computed field after six mesh-refinement steps (passes) for this particular problem. The specifications of the problem are described in Table 4.3.

¹The maximum delta energy is the difference in computed field energies in going from one mesh refinement step to the next one.

Table 4.3: Specifications for the dielectric sphere.

• x -directed plane wave	• $k_0 R = \frac{\pi}{50}$
• $\varepsilon_r = 6$	• $\phi^i = 0$
• $\theta^i = \pi$	• $R = \lambda/100$

Mesh of the structure (1545 micro-basis functions)



(a) Problem (graphical illustration).

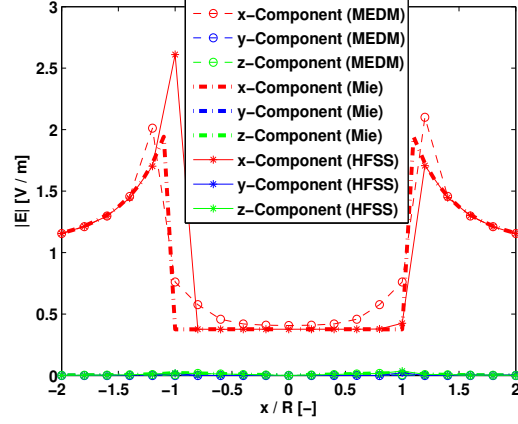
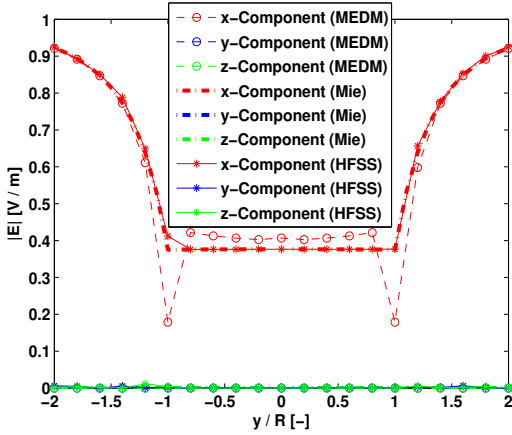
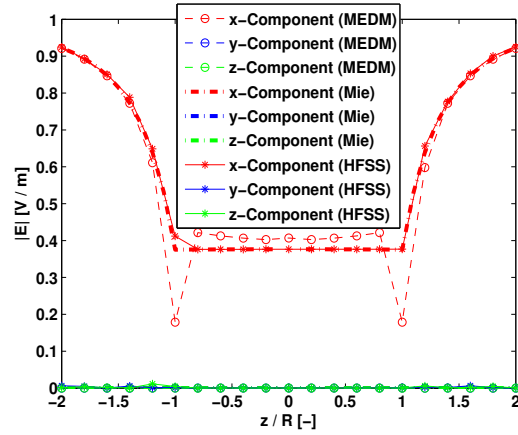
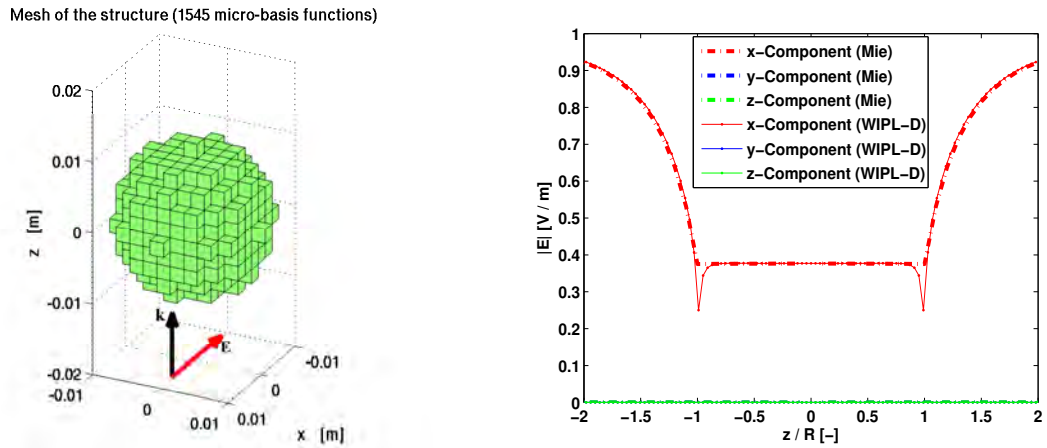
(b) The magnitude of the E-Field along x -axis.(c) The magnitude of the E-Field along y -axis.(d) The magnitude of the E-Field along z -axis.

Figure 4.4: MEDM in comparison with the HFSS and the Mie-series; specifications: see Table 4.3.

As compared to the analytical Mie-series solution, the results obtained by HFSS demonstrate a root mean square relative error of 2.24% while this error is 16.38% for the MEDM and 10.34% in case of WIPL-D [for 21 sample points in (4.8)]. Note that the field inside the sphere is approximately uniform, which is particularly true if the sphere is electrically



(a) Problem (graphical illustration).

(b) The magnitude of the E-Field along z -axis.

Figure 4.5: WIPL-D in comparison with the Mie-series; specifications: see Table 4.3.

small and has a low dielectric contrast. The level of the field inside the sphere can be calculated from [30] as

$$|\mathbf{E}^t| = \left[\frac{3\epsilon_0}{\epsilon_r + 2\epsilon_0} \right] \quad (4.9)$$

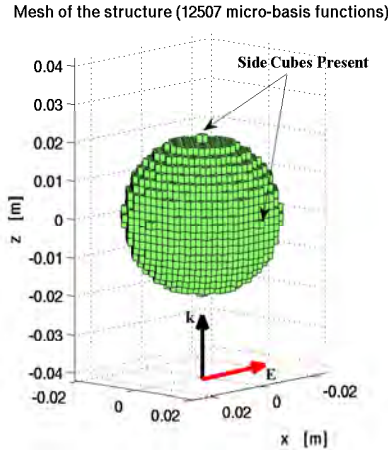
which is evaluated to be 0.375 V/m for this particular problem. But when the size of the sphere becomes electrically large, the field is no more constant inside the sphere. Additionally, as the conductivity of the sphere increases, the field inside the sphere decreases because charges and currents tend to reside on the surface of the conductors.

The magnitude of the field inside the sphere as computed by the MEDM code (cf. Fig. 4.4) is observed to be almost uniform, which resembles the analytical computations rather well. To further analyze the convergence of the field uniformity inside the sphere a larger sphere (as compared to $R = \lambda/100$) is simulated. The results have been depicted in Fig. 4.6. The specifications for the larger sphere with $R = \lambda/50$ can be found in Table 4.4.

Table 4.4: Specifications for the dielectric sphere.

• x -directed plane wave	• $k_0 R = \frac{\pi}{25}$
• $\epsilon_r = 6$	• $\phi^i = 0$
• $\theta^i = \pi$	• $R = \lambda/50$

As can be seen in Fig. 4.6, increasing the size of the sphere forces the value of the magnitude of the E-field inside the sphere to approach the theoretical value of 0.375 V/m, primarily



(a) Problem (graphical illustration).

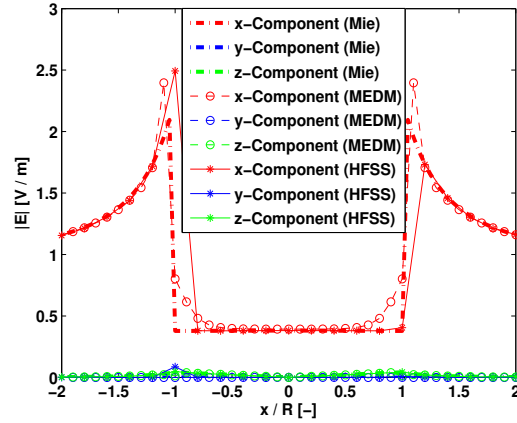
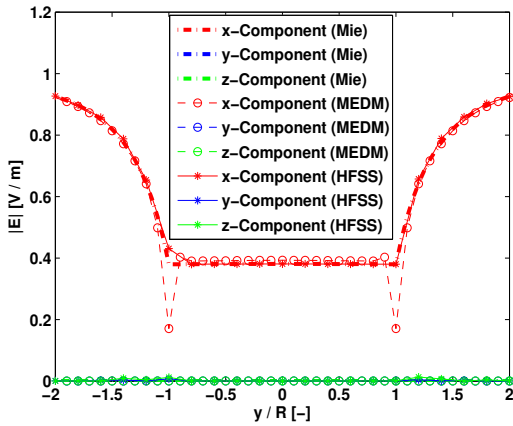
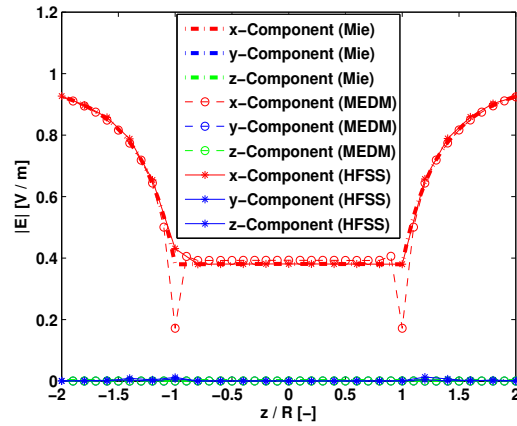
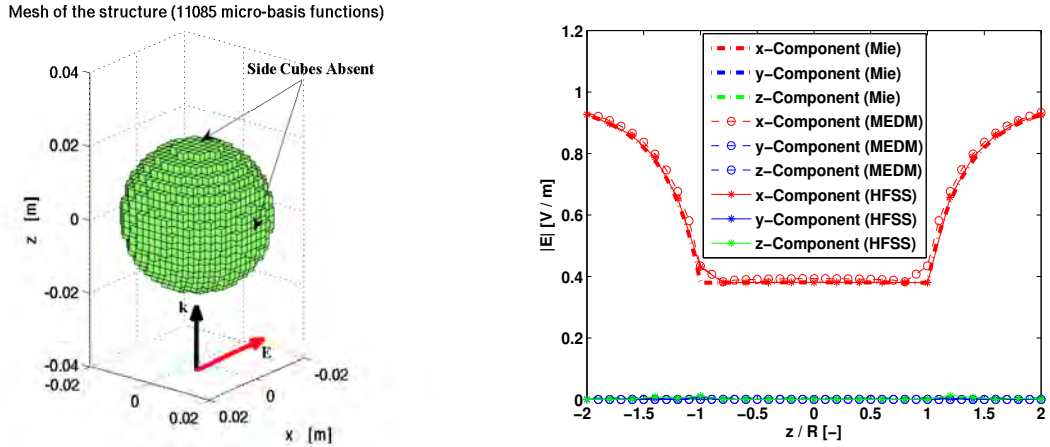
(b) The magnitude of the E-Field along x -axis.(c) The magnitude of the E-Field along y -axis.(d) The magnitude of the E-Field along z -axis.

Figure 4.6: MEDM in comparison with the HFSS and Mie-series; specifications: see Table 4.4.

because the number of basis functions increases for large spheres, so that the geometrical and electrical discretization error becomes smaller. However, a strong discontinuity is observed (similar to in Fig. 4.4) at the surface of the sphere which needs particular attention as it clearly deviates from the analytical solution. In order to investigate the reason for this spurious glitch in the field, certain tests have been performed; one obvious choice is to remove the side cubes and observe the differences between the results, obtained with and without side cubes. The latter has been illustrated in Fig. 4.7. The reason for the field discontinuity at the surface of the sphere (using MEDM) can be investigated using Fig. 4.7, where the glitch disappears after removing the side cubes. As stated previously, we employ pulse-type basis functions for the equivalent current and the divergence of that



(a) Problem (graphical illustration).

(b) The magnitude of the E-Field along z-axis.

Figure 4.7: MEDM in comparison with HFSS and Mie-series; specifications: see Table 4.4.

for the charge density. Hence, taking the divergence of a locally-supported uniform current amounts to surface charges at the end faces of each basis-function cube. By employing these type of basis functions, we possibly observe some glitch in the field solution at the boundary of the dielectric domain due to some residual spurious surface charge at the end faces of this last cube, which can not be compensated for by an opposite charge of a neighboring basis function (since we are already at the boundary). But the results obtained by WIPL-D (c.f. Fig. 4.5) demonstrate that the spurious solution at the edges of the sphere persists even when the entire-domain basis functions of WIPL-D are applied, which renders the above described hypothesis enigmatic.

4.3.2 Scattering From a Small Plate

As mentioned in Chapter 1, available computational tools are known to be inaccurate in case of thin structures; such as thin wires, thin plates, etc. However, MEDM can still yield potentially accurate results as compared to existing commercial software packages owing to the micro-domain basis functions, even if the geometry of the problem is electrically thin. For verification purposes, an electrically thin dielectric plate is simulated using HFSS, WIPL-D and MEDM. The comparison between MEDM, WIPL-D and HFSS is depicted in Fig. 4.8. A maximum delta energy in the field solution of $3.2492e-6$ is obtained after 11 adaptive mesh refinement steps in HFSS. The specifications of the problem are mentioned in Table 4.5.

Table 4.5: Specifications for the electrically thin plate.

• x -directed plane wave	• $k_0 l_x = k_0 l_y = \frac{\pi}{25}$
• $\varepsilon_r = 6$	• $\phi^i = 0$
• $\theta^i = \pi$	• $k_0 l_z = \frac{\pi}{125}$

Here l_x, l_y , and l_z are lengths of the plate in the x, y and z -directions, respectively. To

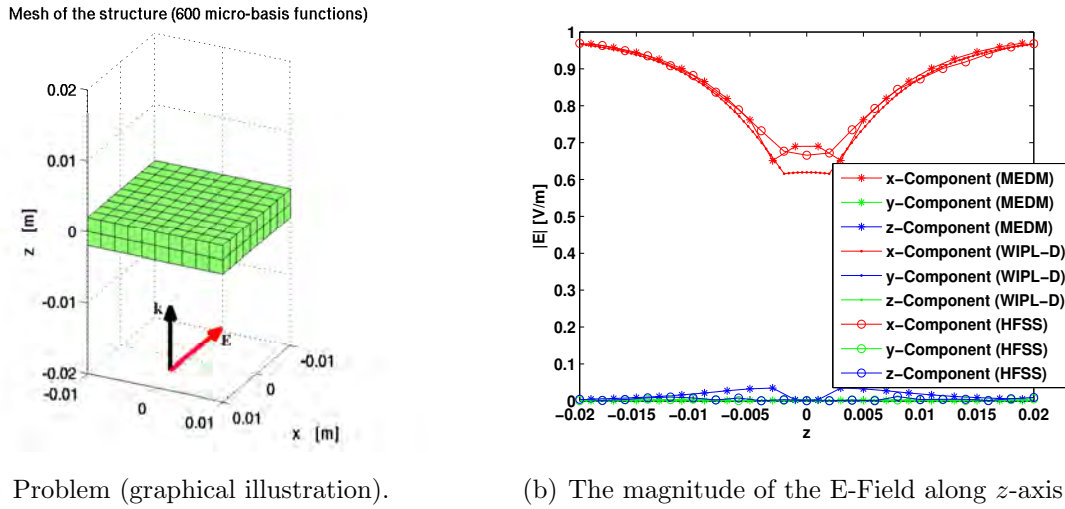


Figure 4.8: MEDM in comparison with HFSS and WIPL-D; specifications: see Table 4.5.

substantiate the aforementioned discussion in this section, the transmission coefficient for a plate with specifications as mentioned in the Table 4.5—but infinitely large in the xy plane—is computed and found to be 0.58. By considering this factor as a reference value, it is apparent from Fig. 4.8 that, MEDM is in good agreement with HFSS and WIPL-D.

4.3.3 Scattering From a Small Dielectric Cube

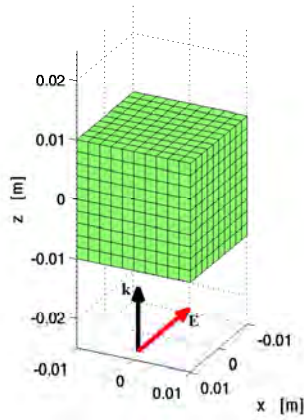
For completeness, a small dielectric cube is simulated in HFSS and compared to the results that are computed by MEDM. The results are depicted in Fig. 4.9. A maximum delta energy of 0.000737 is obtained after 8 adaptive mesh refinement steps in HFSS. The specifications of the problem are as follows:

Table 4.6: Specifications for dielectric cube.

• x -directed plane wave	• $k_0 l_x = k_0 l_y = k_0 l_z = \frac{\pi}{25}$
• $\varepsilon_r = 6$	• $\phi^i = 0$
• $\theta^i = \pi$	

Here $l_x = l_y = l_z$ are the edge lengths of the cube.

Mesh of the structure (3000 micro-basis functions)



(a) Problem (graphical illustration).

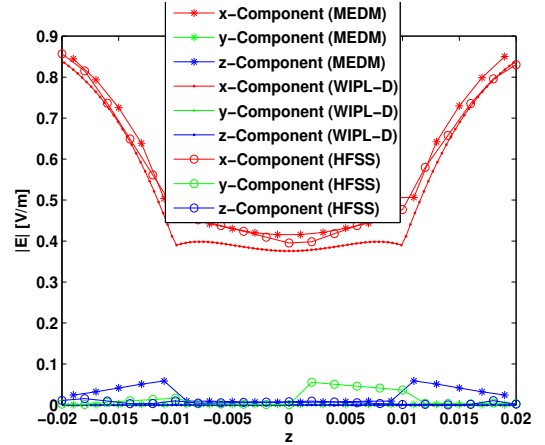
(b) The magnitude of the E-Field along z -axis.

Figure 4.9: MEDM in comparison with HFSS and WIPL-D; specifications: see Table 4.6.

Table 4.7 summarizes the comparison between MEDM and HFSS, for the three different types of problems as discussed in this and the previous sections. It is concluded from Table. 4.7 and the Figs. 4.6, 4.8 and 4.9 that the total execution time is generally shorter than that required by HFSS, while the results are still in good agreement.

4.4 Convergence Study

As described in Sec. 3.2.2, taking a dipole in (3.20) to represent the scattered field is equivalent to using a mid-point integration rule for evaluating the vector potential \mathbf{A} with the actual volumetric current distribution, provided that $Il = a^3$. This is a quasi-static approximation of which the error can be analyzed by subdividing the source cube into smaller sub-cubes each containing an equivalent dipole with a corresponding smaller dipole

Table 4.7: Summary of the comparison between HFSS and MEDM.

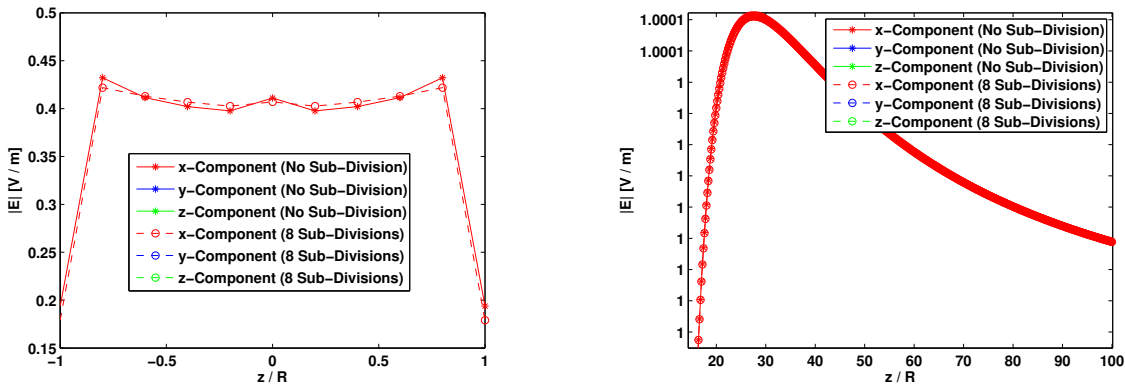
(a) HFSS

Problem Type	Specifications [Reference]	Delta Mag Energy	No. Passes	No. Tetrahedra's	Simulation Time [Sec]
Sphere	Table 4.3	07.2186e-5	14	24178	676
Plate	Table 4.5	3.2492e-6	11	3559	21
Cube	Table 4.6	0.000737	8	1778	10

(b) MEDM

Problem Type	Specifications [Reference]	No. Basis Functions	Simulation Time [Sec]
Sphere	Table 4.3	1545	11.2686
Plate	Table 4.5	600	2.1111
Cube	Table 4.6	3000	16.4713

moment. Fig. 4.10 illustrates the comparison for the exterior and interior fields in case the source cube is subdivided into eight subcubes relative to a single one. Fig. 4.10 shows that



(a) Inside the sphere.

(b) Outside the sphere.

Figure 4.10: Convergence analysis for the exterior field radiated by one basis function of which the supporting cube is subdivided into eight subcubes relative to no subdivisions; specifications: see Table 4.3.

the magnitude of the computed E -field does not improve significantly. It is clear that both results, with and without subdivisions, are approximately the same, so that, a subdivision of the source cube does not lead to more accurate results for the radiated field external to

this cube. It should be realized that this criteria is valid as long as the basis functions are small enough to satisfy the quasi-static condition.

4.5 Conclusions

The Mie-series has been formulated mathematically and its implementation has been validated by comparing the solution for the scattered field to a result published in the literature. In addition, we have numerically computed the results in HFSS and WIPL-D. Despite the simplicity of the MEDM code, the numerical solutions of several scattering problems (sphere, thin plate and cube) are in good agreement with the HFSS and WIPL-D results, as well as with the analytical Mie-series solution for the sphere. However, MEDM is generally faster and requires less amount of memory. Finally, it has been verified numerically that a subdivision of the source cube does not lead to a significant improvement in the field value at neighboring observation cubes.

Chapter 5

Solution to Large Problems

After discretizing the Electric Field Integral Equation (EFIE), one can obtain the numerical solution for electrically small problems only, since the solution of large scattering problems is still memory and time consuming. In order to overcome these limitations, this chapter includes the description of a few novel memory and time efficiency enhancement techniques. More specifically, the Characteristic Basis Function Method (CBFM) and the Adaptive Cross Approximation (ACA) are employed to improve both the memory and time efficiency. Translation symmetry and the Lorentz reciprocity theorem are used to further enhance the time efficiency.

5.1 Introduction

The MoM has been a commonly used tool for obtaining a full wave solution of various computational electromagnetic problems. However, a conventional MoM approach is inefficient in handling electrically large structures. In fact, the large number of required basis functions renders the solution of electrically large problems intractable. A number of computationally efficient techniques have been proposed for the MoM to be able to solve electrically large problems on moderate sized computers. In this chapter, we select and discuss a few of the recently published Efficiency Enhancement Techniques (EETs)—that are compatible with our method—and hybridize these with the previously presented MoM method.

As already pointed out in Chapter 3, when the electrical size of the electromagnetic problem becomes very large, the solution for \mathbf{I} of the relatively large matrix equation $\mathbf{Z}\mathbf{I} = \mathbf{V}$ becomes cumbersome, since the time complexity of a direct Gaussian elimination method scales as $\mathcal{O}(N^3)$, where N is the total number of high-resolution basis functions. Note that the filling of the moment matrix has only a time complexity of $\mathcal{O}(N^2)$. In the following, the CBFM will be used to employ a relatively small set of entire-domain basis functions for the current, thereby reducing the size of the moment matrix equation leading to a faster solve time and reduced memory storage requirements [31]. Furthermore, the ACA algorithm [32] is used, and reciprocity [17, Sec. 7.5] and translation symmetry [13, pp. 104-109] are exploited to reduce the matrix fill time. In the CBFM, entire-domain basis functions—called the Characteristic Basis Functions (CBFs)—are generated numerically using a plane wave spectrum [33], then down-selected using a singular value decomposition with a thresholding procedure on the singular values, after which the reduced set of CBFs thus generated leads to a reduced matrix equation which can be solved for Multiple Right Hand Sides (MRHs). The use of a plane wave spectrum renders the problem independent of the angle of incidence, which is desired in many electromagnetic scattering applications.

5.2 Formulation

The procedure to generate the CBFs, which are then used to reduce the size of the moment matrix, will be discussed in this section.

5.2.1 CBF Generation

The CBFM starts by subdividing the original problem into many smaller blocks each of which will support a set of CBFs. Toward this end, each sub-block is first extended by its neighboring blocks as illustrated in Fig. 5.1 and then excited by plane waves incident from different directions with equal steps in azimuth and elevation angles to obtain a set of basis functions which are independent of the angle of incidence. A two dimensional pictorial representation of a plane-wave spectrum incident on an extended block is provided in Fig. 5.1. To generate CBFs, we use the self-coupling matrix block $\mathbf{Z}_{bb}^{\text{Ext}}$ ($b = 1, 2, \dots, N_b$), where N_b represents the total number of (extended) CBF-blocks. The CBFs pertaining to

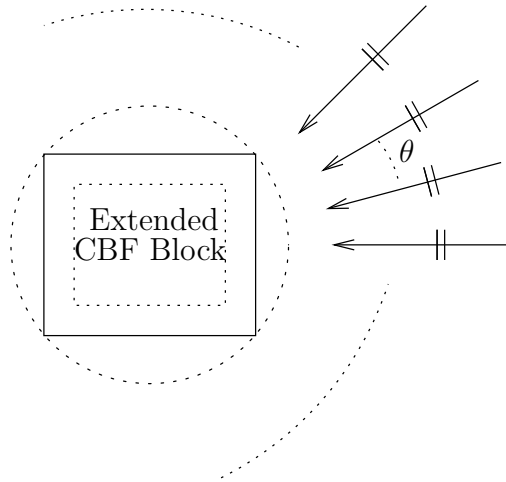


Figure 5.1: 2D Representation of a plane-wave spectrum generation.

the b th sub-block are extracted from the induced current distribution by truncating the support of the current to the original (non-extended) block size. The truncation step is needed to eliminate the edge-singular current at the outer edge of the extended blocks and will therefore lead to a more continuous representation of the equivalent electric current at the interfaces between the non-extended sub-blocks.

Ideally, it is desired to have an orthogonal set of CBFs that can span the whole solution space of the problem. However, the basis functions that are obtained by solving the relatively small MoM equation for MRHS are in general, i.e. after truncation, not independent and carry therefore redundant information (this primarily depends on the density of the plane wave spectrum). Through the application of the singular value decomposition, the set of CBFs can be orthonormalized and reduced using an appropriate thresholding procedure on the singular values as detailed in the next section.

5.2.2 Reduced Matrix Implementation

To rapidly solve the full moment matrix equation, the matrix equation in (2.27) is first reduced through the application of the above-described set of CBFs. To demonstrate the principles of CBFM, we select a simple example representing twelve contiguous CBF-blocks as depicted in Fig. 5.2. In this figure, only one CBF is generated and thus supported per sub-block to maintain simplicity in the notation. As mentioned above, the CBFM subdi-

vides the basic geometry of the problem into many extended sub-blocks, which themselves consist of many micro-domain cubes, and then solves each correspondingly small matrix equation for a spectrum of incident plane waves to generate the CBFs.

For the derivation of the reduced matrix elements, we expand the total equivalent current \mathbf{J}_{eq} in terms of $N^{\text{CBF}} = N_b$ characteristic basis functions (CBFs), so that

$$\mathbf{J}_{\text{eq}}(\mathbf{r}) = \sum_{b=1}^{N^{\text{CBF}}} \alpha_b^{\text{CBF}} \mathbf{J}_b^{\text{CBF}}(\mathbf{r}), \quad (5.1)$$

where $\mathbf{J}_b^{\text{CBF}}$ represents the b th CBF and α_b^{CBF} represents the b th unknown expansion coefficient for that CBF. The b th CBF is expanded in terms of $N_b^{\mu\text{BF}}$ micro-basis functions with known expansion coefficients $\{\alpha_l^b\}_{l=1}^{N_b^{\mu\text{BF}}}$, as;

$$\mathbf{J}_b^{\text{CBF}}(\mathbf{r}) = \sum_{l=1}^{N_b^{\mu\text{BF}}} \alpha_l^b \mathbf{f}_l^b(\mathbf{r}). \quad (5.2)$$

The vector basis function \mathbf{f}_l^b represents the l^{th} micro-domain basis function on the b th domain. The reduced moment matrix element $\mathbf{Z}_{mn}^{\text{CBF}}$ between the n^{th} source and m^{th} observation CBF is given as

$$\begin{aligned} \mathbf{Z}_{mn}^{\text{CBF}} &= \frac{1}{j\omega(\varepsilon - \varepsilon_0)} \langle \mathbf{J}_n^{\text{CBF}}(\mathbf{r}), \mathbf{J}_m^{\text{CBF}}(\mathbf{r}) \rangle - \langle \mathbf{E}^s(\mathbf{J}_n^{\text{CBF}}(\mathbf{r})), \mathbf{J}_m^{\text{CBF}}(\mathbf{r}) \rangle \\ &= \sum_{i=1}^{N_b^{\mu\text{BF}}} \sum_{j=1}^{N_b^{\mu\text{BF}}} \left[\alpha_i^m \left(\underbrace{\frac{1}{j\omega(\varepsilon - \varepsilon_0)} \langle \mathbf{f}_j^n(\mathbf{r}), \mathbf{f}_i^m(\mathbf{r}) \rangle - \langle \mathbf{E}^s(\mathbf{f}_j^n(\mathbf{r})), \mathbf{f}_i^m(\mathbf{r}) \rangle}_{\mathbf{Z}_{ij}^{mn}} \right) \alpha_j^n \right] \\ &= \sum_{i=1}^{N_b^{\mu\text{BF}}} \sum_{j=1}^{N_b^{\mu\text{BF}}} \alpha_i^m \mathbf{Z}_{ij}^{mn} \alpha_j^n \\ &= (\boldsymbol{\alpha}^m)^T \mathbf{Z}^{mn} \boldsymbol{\alpha}^n. \end{aligned} \quad (5.3)$$

Similarly, the m^{th} element $\mathbf{V}_m^{\text{CBF}}$ of the reduced excitation vector is computed as

$$\begin{aligned} \mathbf{V}_m^{\text{CBF}} &= \iint_{S_m} \mathbf{J}_m^{\text{CBF}} \cdot \mathbf{E}^i(\mathbf{r}) \, dS \\ &= \sum_{i=1}^{N_b^{\mu\text{BF}}} \alpha_i^m \left[\iint_{S_m} \mathbf{f}_i^m \cdot \mathbf{E}^i(\mathbf{r}) \, dS \right] \\ &= (\boldsymbol{\alpha}^m)^T \mathbf{V}_m, \end{aligned} \quad (5.4)$$

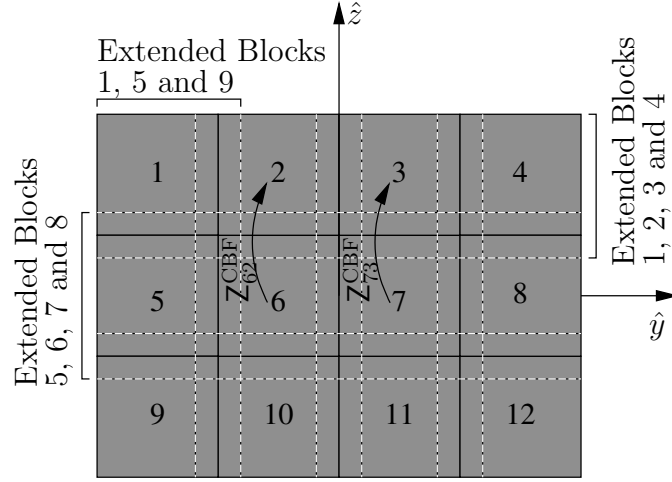


Figure 5.2: 2-D representation of the block extension in the CBFM.

where the vector \mathbf{V}_m is the excitation vector of the original problem pertaining to the m th block.

In conclusion, the moment matrix equations can be reduced to a small size matrix representation using the CBFM to yield

$$\begin{bmatrix} \mathbf{Z}_{11}^{\text{CBF}} & \cdots & \mathbf{Z}_{1(12)}^{\text{CBF}} \\ \vdots & \ddots & \vdots \\ \mathbf{Z}_{(12)1}^{\text{CBF}} & \cdots & \mathbf{Z}_{(12)(12)}^{\text{CBF}} \end{bmatrix} \begin{bmatrix} \alpha_1^{\text{CBF}} \\ \vdots \\ \alpha_{(12)}^{\text{CBF}} \end{bmatrix} = \begin{bmatrix} \mathbf{V}_1^{\text{CBF}} \\ \vdots \\ \mathbf{V}_{(12)}^{\text{CBF}} \end{bmatrix}, \quad (5.5)$$

where $\mathbf{Z}_{bb}^{\text{CBF}}$ is the reduced self-coupling matrix element for the CBF-block b ; $\mathbf{Z}_{bc}^{\text{CBF}}$ is the reduced coupling element for the source CBF-block c and the observation CBF-block b (cf., Fig. 5.2). Similarly, $\mathbf{V}_b^{\text{CBF}}$ and α_b^{CBF} are the elements for the reduced excitation and CBF expansion coefficient vectors, respectively.

If more than one CBF is generated per subdomain, say N_b^{PWS} CBFs for the b th subdomain, the N_b^{PWS} CBF expansion coefficient vectors $\alpha_{b,n_w}^{\text{CBF}}$ for $n_w = 1, 2, \dots, N_b^{\text{PWS}}$ can be stacked in a column-augmented matrix \mathbf{A}_b as $\mathbf{A}_b = [\alpha_{b,1}^{\text{PWS}} : \alpha_{b,2}^{\text{PWS}} : \cdots : \alpha_{b,N_b^{\text{PWS}}}^{\text{PWS}}]$. To reduce and orthonormalize this set we use the singular value decomposition of \mathbf{A}_b :

$$\mathbf{A}_b = \mathbf{U}_b \mathbf{S}_b \mathbf{V}_b^{\text{H}}, \quad (5.6)$$

where \mathbf{U}_b is a matrix with orthogonal columns, \mathbf{V}_b^{H} is a matrix with orthogonal rows, and \mathbf{S}_b is a diagonal matrix holding the singular values in descending order. Accordingly, an appropriate threshold—depending on the final desired accuracy of the synthesized current—can

be selected beyond which the singular values can be set to zero. As a result, the corresponding columns of \mathbf{U}_b with zero eigenvalues and rows from \mathbf{V}_b^H can be removed. In effect, this leads to a more compact representation of the CBFs since only a few columns of \mathbf{U}_b have to be retained as CBFs.

5.3 Acceleration Techniques

In the previous section, we have described the CBFM to increase the time and memory efficiency of solving the moment matrix equation. In this section we will introduce a number of complementary techniques that can be used to reduce the moment matrix fill time. One widely known technique to reduce the moment matrix fill time is the Fast Multipole Method (FMM) [34] which involves the multipole expansion of the free-space Green's function. Since the FMM is not kernel independent, we opt for more general fully algebraic efficiency enhancement techniques for reducing the time complexity of filling the reduced moment matrix equation. In particular, MEDM will be enhanced by exploiting reciprocity and translation symmetry, and by making use of the ACA. In this section, we briefly describe these techniques.

5.3.1 Lorentz Reciprocity

The Lorentz reciprocity theorem describes the symmetric relation between the transmitting and receiving antenna, that is, if a current is applied at the source antenna, it will induce an open-circuit voltage at the receiving antenna, while – in the reciprocal case – if this same current is applied at the receiving antenna, it will induce the same open-circuit voltage at the transmitting antenna [17, Sec. 7.5]. The reciprocity relation for electric currents only is expressed as

$$\iiint_V \mathbf{J}_1 \cdot \mathbf{E}_2 \, dV = \iiint_V \mathbf{E}_1 \cdot \mathbf{J}_2 \, dV. \quad (5.7)$$

A consequence of this theorem is that the mutual impedance between the antennas is identical in both the transmitting and receiving situations ($Z_{12} = Z_{21}$, see Fig. 5.3). Similarly, the moment matrix is symmetric since the source basis functions act as the “transmitting antennas” while the testing functions are the “receiving antennas”. Hence, the matrix

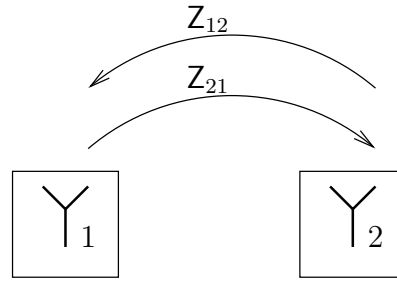


Figure 5.3: Coupling between the two blocks.

in (2.27) is symmetric so that only the upper triangular and diagonal entries need to be computed. The entries in the lower triangular matrix block can simply be obtained by transposing the upper triangular matrix block. It is pointed out that reciprocity can be exploited at multiple-levels in the moment matrix formulation, i.e., on micro- as well as on macro-domain level. An example at macro-domain level is given in Fig. 5.2, where the matrix element Z_{62}^{CBF} is observed to be the same as the matrix element Z_{26}^{CBF} .

5.3.2 Translation Symmetry

The off-diagonal moment matrix entries [i.e. Eq. (3.16) and (3.18)] depend primarily on the distance and mutual orientation between the source and the observation micro-domain basis functions; this property also holds for the CBFs. The reaction integrals for source and observation basis function pairs are therefore the same. This, so-called translation symmetry, has also been exploited in the CBFM-enhanced MEDM to rapidly form the many self and coupling block matrices. The latter has been illustrated in Fig. 5.2; the matrix elements Z_{62}^{CBF} and Z_{73}^{CBF} are identical, so that, only one of them needs to be computed, while the second can simply be replaced by that value.

5.3.3 The Adaptive Cross Approximation (ACA)

The interaction (moment matrix block) between two well-separated groups of basis functions can be represented accurately and efficiently by a much smaller subset of these groups. In fact, the interaction of two well-separated groups of basis functions results in a rank reduction of the corresponding moment matrix block. A near-square low-rank matrix block

can be compressed efficiently through the ACA algorithm. This algorithm is described thoroughly in [32, 35], and summarized below.

Let $\mathbf{Z}^{m \times n}$ represent the moment matrix coupling block between the basis functions supported by two well-separated blocks in the MoM computational domain. The goal of the ACA is to approximate $\mathbf{Z}^{m \times n}$ by the lower rank matrix $\tilde{\mathbf{Z}}^{m \times n}$ with a prescribed accuracy. More specifically, the ACA algorithm constructs the approximated matrix $\tilde{\mathbf{Z}}^{m \times n}$ through a product form,

$$\tilde{\mathbf{Z}}^{m \times n} = \mathbf{U}^{m \times r} \mathbf{V}^{r \times n} = \sum_{i=1}^r \mathbf{u}_i^{m \times 1} \mathbf{v}_i^{1 \times n} \quad (5.8)$$

where r is the effective rank of the matrix $\mathbf{Z}^{m \times n}$. The goal of the ACA is to achieve

$$|\mathbf{R}^{m \times n}| = |\mathbf{Z}^{m \times n} - \tilde{\mathbf{Z}}^{m \times n}| \leq \varepsilon |\mathbf{Z}^{m \times n}| \quad (5.9)$$

where \mathbf{R} is termed the error matrix and ε is a given accuracy. The norm $|\cdot|$ is herein the 2-norm, or *Frobenius* norm.

Let $\mathbf{I} = [I_1, \dots, I_r]$ and $\mathbf{J} = [J_1, \dots, J_r]$ be the arrays containing orderly selected row and column indexes of the matrix $\mathbf{Z}^{m \times n}$. The following ACA algorithm is written in Matlab's notation, where $\tilde{\mathbf{R}}(I_1, :)$ stands for the I^{th} row of the matrix $\tilde{\mathbf{R}}$.

The steps involved in the ACA algorithm are as follows:

1. Initialize the 1st row index $I_1 = 1$ and $\tilde{\mathbf{Z}} = \mathbf{0}$.
2. Initialize the 1st row of the approximate error matrix: $\tilde{\mathbf{R}}(I_1, :) = \mathbf{Z}(I_1, :)$.
3. Find the 1st column index J_1 : $|\tilde{\mathbf{R}}(I_1, J_1)| = \max_j |\tilde{\mathbf{R}}(I_1, j)|$.
4. $\mathbf{v}_1 = \tilde{\mathbf{R}}(I_1, :) / \tilde{\mathbf{R}}(I_1, J_1)$.
5. Initialize 1st column of the approximate error matrix: $\tilde{\mathbf{R}}(:, J_1) = \mathbf{Z}(:, J_1)$.
6. $\mathbf{u}_1 = \tilde{\mathbf{R}}(:, J_1)$.
7. $|\tilde{\mathbf{Z}}^{(1)}|^2 = |\tilde{\mathbf{Z}}^{(0)}|^2 + |\mathbf{u}_1|^2 |\mathbf{v}_1|^2$.
8. Find the 2nd row index I_2 : $|\tilde{\mathbf{R}}(I_2, J_1)| = \max_i (|\tilde{\mathbf{R}}(i, J_1)|)$.

5.4. The MEDM with and without the Efficiency Enhancement Techniques (EETs) 49

k^{th} iteration:

1. Update I_k^{th} row of the approximate error matrix: $\tilde{\mathbf{R}}(I_k, :) = \mathbf{Z}(I_k, :) - \sum_{l=1}^{k-1} (\mathbf{u}_l)_{I_k} \mathbf{v}_l$.
2. Find the next column index J_k : $|\tilde{\mathbf{R}}(I_k, J_k)| = \max_j (|\tilde{\mathbf{R}}(I_k, j)|), j \neq J_1, \dots, J_{k-1}$.
3. $\mathbf{v}_k = \tilde{\mathbf{R}}(I_k, :) / \tilde{\mathbf{R}}(I_k, J_k)$.
4. Update J_k^{th} column of the approximate error matrix: $\tilde{\mathbf{R}}(:, J_k) = \mathbf{Z}(:, J_k) - \sum_{l=1}^{k-1} (\mathbf{v}_l)_{J_k} \mathbf{u}_l$.
5. $\mathbf{u}_k = \tilde{\mathbf{R}}(:, J_k)$.
6. $|\tilde{\mathbf{Z}}^{(k)}|^2 = |\tilde{\mathbf{Z}}^{(k-1)}|^2 + 2 \sum_{j=1}^{k-1} |\mathbf{u}_j^T \mathbf{u}_k| \cdot |\mathbf{v}_j^T \mathbf{v}_k| + |\mathbf{u}_k|^2 |\mathbf{v}_k|^2$.
7. Check convergence: if $|\mathbf{u}_k| |\mathbf{v}_k| \leq \varepsilon |\tilde{\mathbf{Z}}^{(k)}|$, end iteration.
8. Find the next row index I_{k+1} : $|\tilde{\mathbf{R}}(I_{k+1}, J_k)| = \max_i (|\tilde{\mathbf{R}}(i, J_k)|), i \neq I_1, \dots, I_k$.

5.3.4 Fast Matrix Generation and Solution

To examine the effectiveness of the previously described EETs, we select a plate of size $20 \times 20 \times 5$ microdomain basis functions and then subdivide and solve the combined problem using CBF blocks of size $5 \times 5 \times 5$ micro-domain basis functions. The comparison results between the MEDM, with and without employing Efficiency Enhancement Techniques (EETs), are listed in Table 5.1. The corresponding problems have been depicted in Fig. 5.4. The computational platform used for solving the problems consists of a remote desktop server, equipped with a quad core processor and 148 GB of RAM, operating at 2.2 GHz. For the problems mentioned in Table 5.1, the tolerance for the ACA and the CBFM are set to be 1/15 and 1/100, respectively.

5.4 The MEDM with and without the Efficiency Enhancement Techniques (EETs)

The dielectric objects discussed earlier in Chapter 4 for several different shapes are reconsidered in this section for the case when EETs are employed. The computed scattered

Table 5.1: Comparison of the total solution time for the MEDM with and without employing the EETs

(a) Performance parameters for both the CBFM and ACA

No. of Blocks	No. of Micro-Basis	No. of Uniq. CBFs	No. of MoM Blocks [λ]	Min. Block Sep. Dist. ACA
16	6000	9	117	0.012
32	12000	18	459	0.012
48	18000	27	1026	0.012
64	24000	27	1701	0.012
80	30000	27	2376	0.012

(b) Time efficiency comparison

No. of Blocks	CBFM & ACA Time [s]	No CBFM & No ACA Time [s]	Fig. Ref. [Fig. No.]
16	46.48	56.3	5.4(a)
32	157.00	155.73	5.4(b)
48	391.05	409.26	5.4(c)
64	620.5	841.75	5.4(d)
80	782	1493.7	5.4(e)

fields for MEDM with EETs have been compared to those computed in Chapter 4. In Chapter 4, we have validated MEDM by comparing the numerically computed solution to Ansoft's HFSS (v 13.0), in terms of the accuracy, execution time and memory usage. In the following subsections, we will investigate the accuracy and time efficiency of the EETs in comparison with the plain MEDM.

For the generation of the results that follow, an Intel Centrino laptop equipped with a dual core processor@2.2 GHz and 2GB of RAM has been used; except for the sphere of radius $R = \lambda/50$, where a remote desktop server has been used equipped with a quad core processor@2.2 GHz and 148GB of RAM.

5.4. The MEDM with and without the Efficiency Enhancement Techniques (EETs)

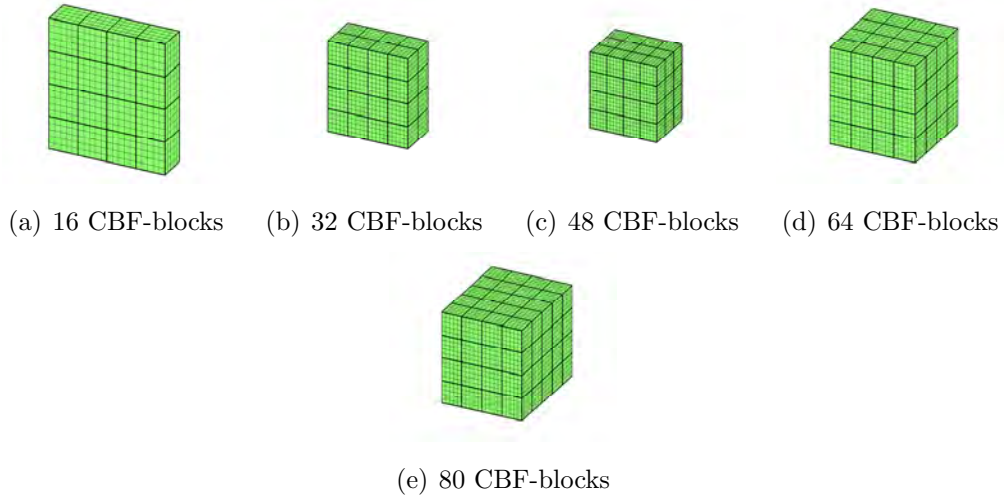


Figure 5.4: Progressive increase in CBFM blocks, examining the effectiveness of EETs

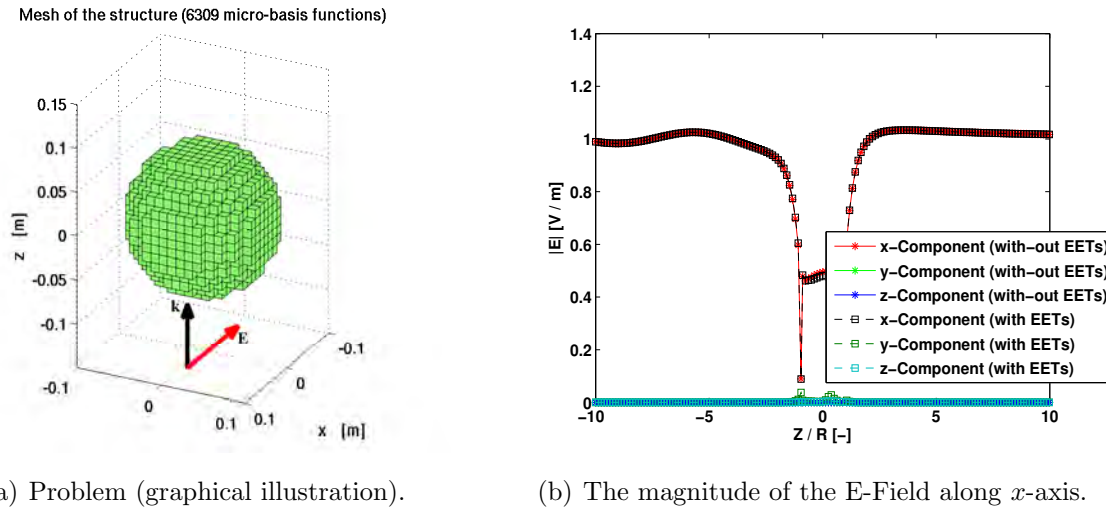
5.4.1 Scattering From a Dielectric Sphere

A dielectric sphere has been simulated using the MEDM, both with and without employing the EETs. The comparison between the numerical results is depicted in Fig. 5.5. The specifications of the problem are described in Table 5.2.

Table 5.2: Specifications for the dielectric sphere.

• x -polarized plane wave	• $k_0 R = \frac{1}{2}$
• $\varepsilon_r = 6$	• $\phi^i = 0$
• $\theta^i = \pi$	• $R = \lambda/4\pi$

The results obtained when EETs are employed seem to be in good correspondence to those obtained without EETs, as illustrated in Fig. 5.5. The field inside the sphere—as computed by the MEDM code (cf., Fig. 5.5)—resembles the analytical computations very well, apart from a spurious glitch in the field solution that has already been discussed in Chapter 4. Usually we are interested in physical quantities that are integrals over the fields or currents (scattering patterns, power losses, energy storage, etc.); hence, the glitch at only the last cell may not be of much concern. For instance, the time-average stored electric energy $1/4 \iiint \varepsilon |\mathbf{E}|^2 dV$ is for MEDM: 5.68e-15 [J]; HFSS: 5.60e-15 [J]; and Mie: 5.77e-15 [J], which shows that MEDM result is close to the analytically derived value, than is the one given by HFSS.



(a) Problem (graphical illustration).

(b) The magnitude of the E-Field along x -axis.

Figure 5.5: MEDM results with and without employing EETs; specifications: see Tables 4.3 and 5.2.

5.4.2 Scattering From a Small Plate

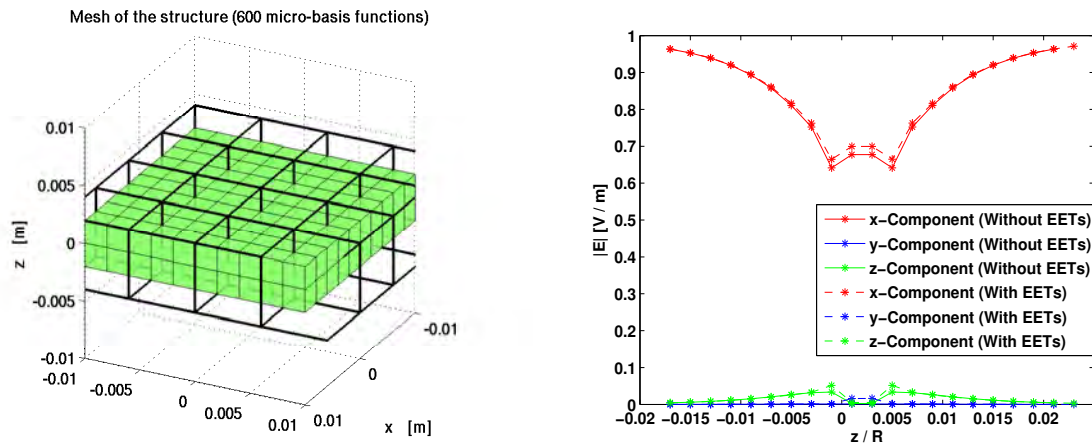
An electrically thin dielectric plate has been simulated using the MEDM (see Table 4.5). The comparison between the MEDM—with and without employing EETs—is depicted in Fig. 5.6. The specifications for the corresponding EETs and the total execution time are listed in Table 5.3.

Table 5.3: EET specifications for the electrically thin plate.

• CBF-Block Size = $3 \times 3 \times 3$	• CBF-Block Exten. Dist. = 2 Cells
• MinDistACA = $5 \times \text{MeshCellSize}$	• TolACA = $1/40$
• Execution Time = 25.1248 Sec	

It is apparent from Table 5.3 that, when the geometry of the object is very small compared to the size of CBF-block, or when the degree of translation symmetry is less, a plain MEDM can even outperform the MEDM with EETs employed, both in terms of the execution time and memory usage. This is due to a relatively large computational overhead in the CBFM which is needed for generating the CBFs.

5.4. The MEDM with and without the Efficiency Enhancement Techniques (EETs)



(a) Problem (graphical illustration).

(b) The magnitude of the E-Field along z-axis.

Figure 5.6: Accuracy of MEDM with and without employing EETs; specifications: see Tables 4.5 and 5.3.

5.4.3 Scattering From a Small Dielectric Cube

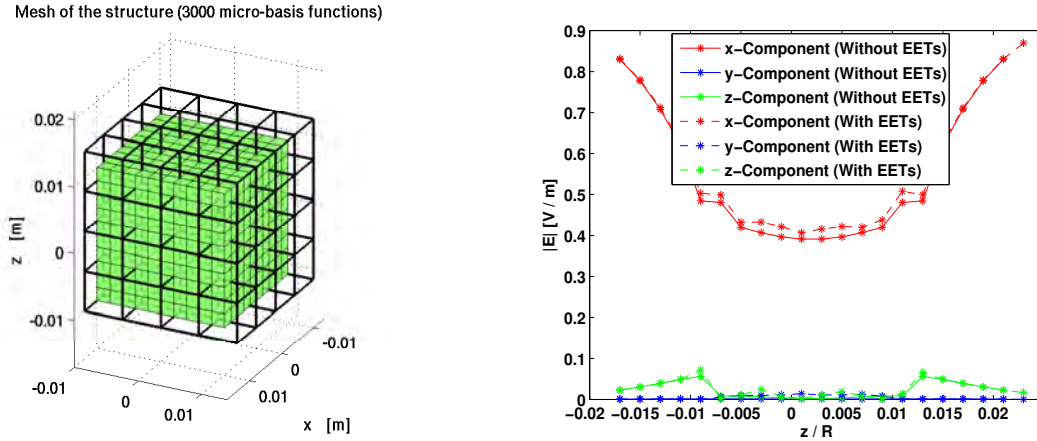
A relatively small dielectric cube is simulated using MEDM without employing EETs to be able to compare it to the results that are computed by MEDM when EETs are employed. The results are depicted in Fig. 5.7. The specifications of the problem are as follows:

Table 5.4: EET specifications for the dielectric cube.

• CBF-Block size = $3 \times 3 \times 3$	• CBF-Block Exten. Dist. = 2 Cells
• MinDistACA = $5 \times$ Mesh Cell Size	• TolACA = $1/40$
• Execution Time = 159.7257 Sec	

Table 5.5 summarizes the comparison between the results—generated by MEDM—with and without the application of EETs, for the three different types of problems as discussed in this and the previous section.

It is concluded from Table. 5.5 and the Figs. 5.5, 5.6 and 5.7 that the use of EETs do not affect the solution accuracy much but do increase the computational efficiency significantly. A larger improvement is expected for a multi-level CBFM approach.



(a) Problem (graphical illustration).

(b) The magnitude of the E-Field along z -axis.

Figure 5.7: MEDM in comparison with HFSS; specifications: see Table 4.6.

Table 5.5: Summary of comparison between EETs and without EETs.

Problem Type	CBFM Specifications [Reference]	Execution Time	
		With EETs	Without EETs
Sphere	Table 5.2	150.0000	165.0000
Plate	Table 5.3	25.1248	2.1111
Cube	Table 5.4	159.7257	16.4713

5.4.4 Solution to Electrically Large Problems for MEDM

Generally, the largest size of the problem that can be solved by MEDM depends upon the available system memory. Nevertheless, in order to guesstimate the largest number of basis functions that can be solved on a machine whose specifications have been mentioned in Section 5.3.4, a sphere of radius $R = \lambda/8$ has been simulated first, for which the results have been depicted in Fig. 5.8. The edge length for the basis functions is set to $\lambda/100$.

Table 5.6: Specifications for the largest solvable dielectric sphere.

• x -polarized plane wave	• $k_0 R = \frac{\pi}{4}$
• $\varepsilon_r = 6$	• $\phi^i = 0$
• $\theta^i = \pi$	• $R = \lambda/8$

Accordingly, the size of sphere is increased even further. The results have been depicted

5.4. The MEDM with and without the Efficiency Enhancement Techniques (EETs)

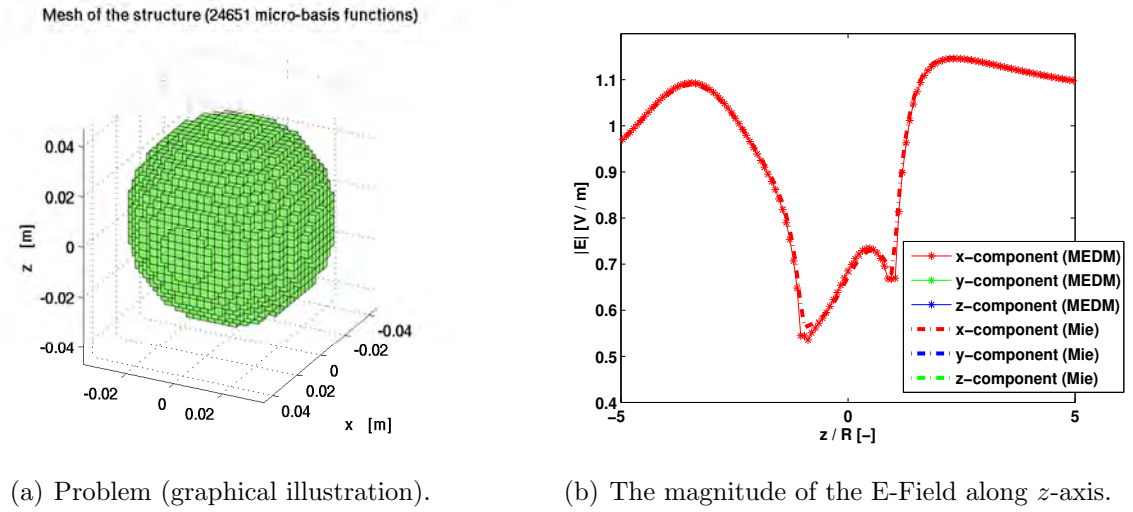


Figure 5.8: Solution to an electrically large problem by the MEDM. Specifications: see Table 5.6.

in Fig. 5.9, while the specifications of the problem can be found in Table 5.7.

Table 5.7: Specifications for the largest solvable dielectric sphere.

• x -polarized plane wave	• $k_0 R = \frac{\pi}{3}$
• $\varepsilon_r = 6$	• $\phi^i = 0$
• $\theta^i = \pi$	• $R = \lambda/6$

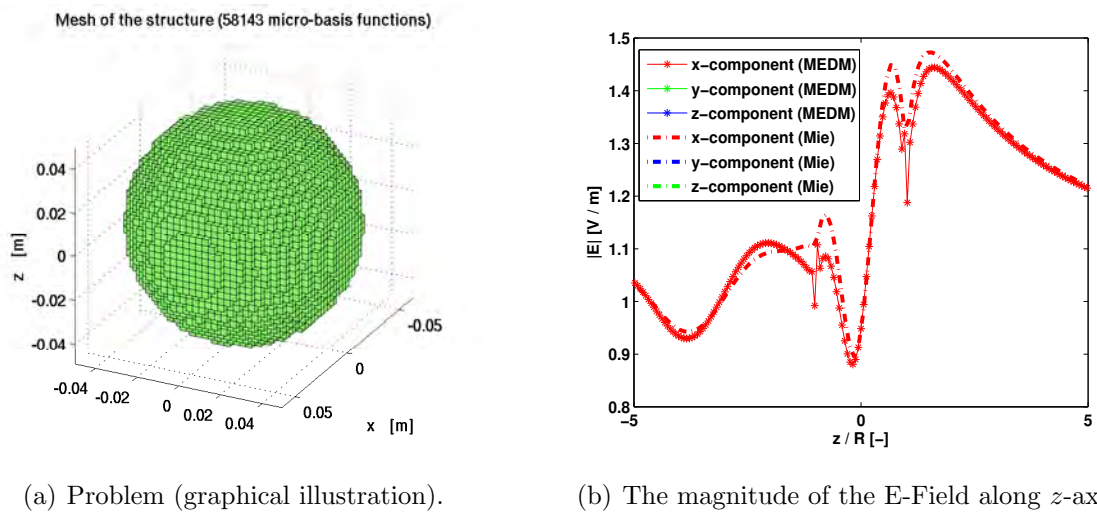


Figure 5.9: Solution to an electrically large problem by the MEDM. Specifications: see Table 5.6.

5.5 Conclusions

The CBFM and the ACA algorithm have been described, implemented, and applied to several scattering problems. It has been demonstrated that the MEDM with EETs employed can provide enhanced memory storage capabilities and reduce the total execution time significantly, with only a subtle compromise on the accuracy of the desired results. In general, there exists no hard limit on the size of the problem. It merely depends on the available memory resources, and processor specifications to achieve fast results, nonetheless, we have solved an electrically large problem with promising results, among which is a sphere of radius $\lambda/6$ whose current is synthesized by approximately 60,000 high-resolution basis functions. It is expected that even larger problems can be handled when a multi-level version of MEDM is employed.

Chapter 6

Numerical Results

The procedure to measure the permittivity of a radome material using a substrate measurement system has been described in this chapter. The MEDM, as developed during this research project, has been applied to an electrically-large radome covering a dipole antenna array. The influence of the radome on the antenna gain pattern has been studied.

6.1 Substrate Measurement System (SMS)

The SMS is a ring-resonator-based system for the measurement of the permittivity and loss tangent of a sample of dielectric material in the frequency range 1-13 GHz [36,37]. In this section, we briefly describe the procedure to measure the permittivity of a dielectric material, and elaborate on the electromagnetic principles of the measurement method.

6.1.1 Measurement Setup

The apparatus consists of a mechanical setup and software for processing the measurement results that are obtained from a network analyzer. The mechanical setup procedure is described as follows:

A sample of the radome, to be used for the measurements, must be cut with dimen-

sions 56×64 mm and placed on the ground plane of the measurement device as shown in Fig. 6.2(b). The accuracy of the 56 mm size must be quite precise (± 0.1 mm) and the thickness of the sample must be between 0.5 and 1.5 mm. If the thickness of the sample is less than 0.5 mm, it can be stacked with other samples. Samples of Teflon material (5 stacked layers of 0.1 mm each) and Mylar (5 mm thickness) are shown in Figs. 6.1(a) and 6.1(b), respectively. The resonator is placed on top of the sample with the microstrip ring (or strip) facing downwards as shown in Fig. 6.2(c). Afterwards, the coupling elements are placed at the brass board [cf., Fig. 6.2(d)]. There are two available types of coupling elements embedded with the SMS; the coupling element with pin length 0.7 mm can be used, however, if it does not yield a scattering parameter S_{12} in the range -50 to -15 dB, then a coupling element with pin length 0.3 mm can be used. The sample is tightened using the clippers as depicted in Fig. 6.2(e). To measure the resonant frequencies, connect the coaxial cables of the network analyzer must be connected to the coupling elements (cf., Fig. 6.3).

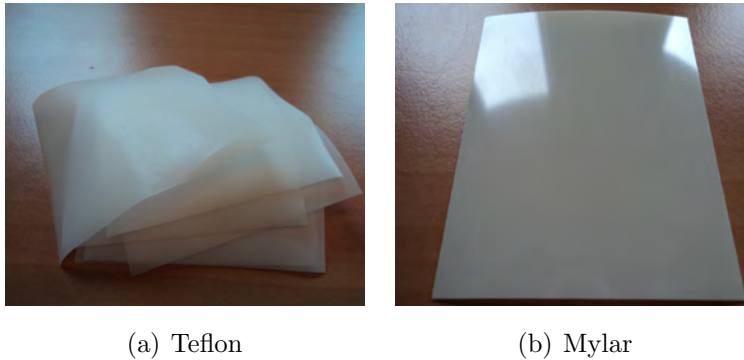


Figure 6.1: Measurement samples as used for the Eleven Feed Radome [38]

6.1.2 The Principle of the Measurement Technique

Herein, we briefly describe the principle of the measurement technique. A thorough exposition of the microstrip ring resonator measurement technique can be found in [37]. The basic principle relies upon the variational principle, where the permittivity of the test material is varied, and hence, the capacitance of the resonator. A ring resonator is used to perform the measurements, primarily because the ring resonator has high quality factor. The ring resonator comprises a copper ring etched on a substrate as shown in Fig. 6.5. The resonance frequency can be determined by setting the guided wavelength (λ_g) equal

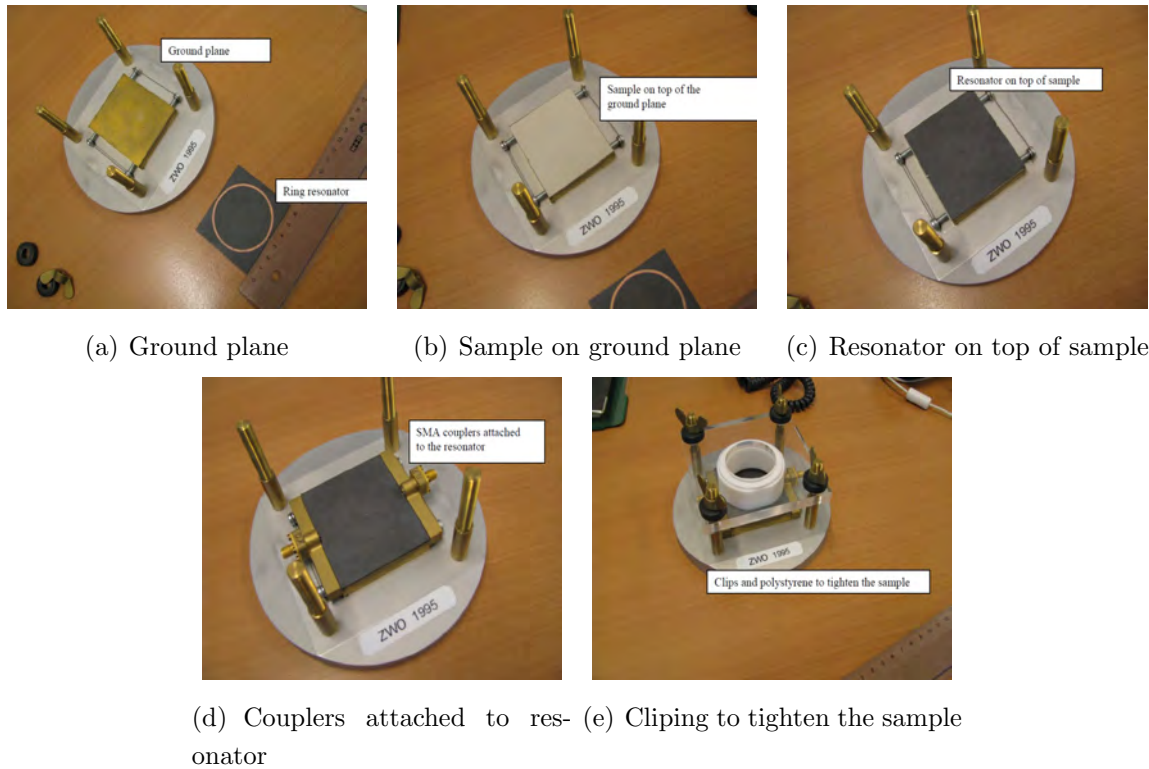


Figure 6.2: Dielectric substrate measurement setup

to a multiple of circumference of the ring, as dictated by the expression [39]

$$\pi(a + b) = n\lambda_g. \quad (6.1)$$

In the above expression, n is the harmonic number, a and b are the inner and outer diameters of the ring, respectively, $\lambda_g = \lambda_0 / \sqrt{\varepsilon_{\text{eff}}(f)}$, and the effective permittivity $\varepsilon_{\text{eff}}(f)$ of the microstrip line can be found in, for instance, [17, 40, 41, Sec. 8.8.2, Sec. 3.4.1, Sec. 1.2.1, respectively]. By rearranging the above expressions, the resonant frequencies of the microstrip line can be calculated as

$$f_n = \frac{nc}{\pi(a + b)\sqrt{\varepsilon_{\text{eff}}(f)}}, \quad (6.2)$$

where c is the speed of light in free space. The following expression describes the relation between the capacitance of a loaded and an unloaded line,

$$\frac{\lambda}{\lambda_0} = \sqrt{\frac{C_0}{C}} = \frac{1}{\sqrt{\varepsilon_{\text{eff}}(f)}}. \quad (6.3)$$

In the above equation, λ_0 and C_0 are the wavelength and capacitance—respectively—of an unloaded ($\varepsilon_1 = \varepsilon_2 = 1$, see Fig. 6.4) line. Similarly, λ and C are the wavelength

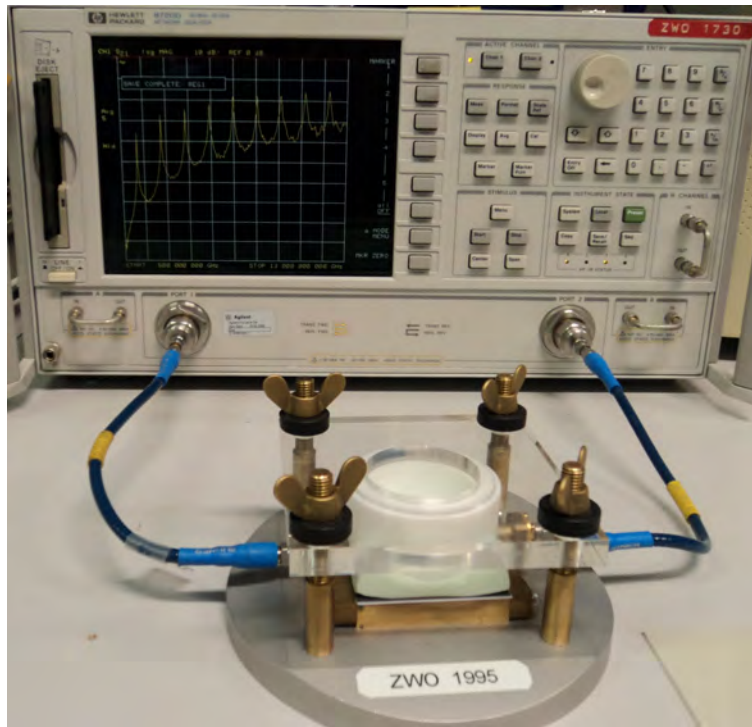


Figure 6.3: Measurement setup and results

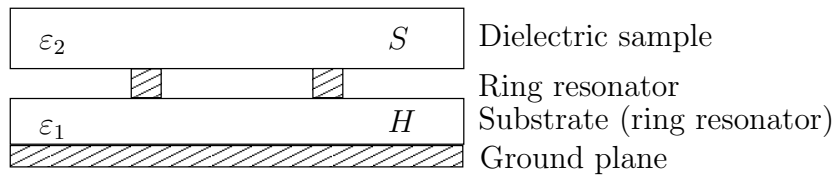
Figure 6.4: Schematic diagram of a dielectric substrate measurement system. Symbols S and H denote the substrate (ring resonator) and sample thicknesses, respectively.

Figure 6.5: Ring resonator

and capacitance—respectively—of a loaded ($\varepsilon_1 = 10$, $\varepsilon_2 = v$) line, where v denotes the variable to be determined. The capacitance of the line can be calculated using the following expression [42, 43]:

$$\frac{1}{C} = \frac{1}{\pi Q^2 \varepsilon_0} \int_0^\infty [f(\beta)]^2 g(\beta) d\beta, \quad (6.4)$$

where

$$Q = \int_{-\infty}^{+\infty} f(x) dx, \quad (6.5a)$$

$$f(\beta) = \int_{-\infty}^{+\infty} f(x) e^{j\beta x} dx, \quad (6.5b)$$

$$g(\beta) = \frac{\varepsilon_2 s}{|\beta| \varepsilon_2 [\varepsilon_2 + \varepsilon_1 h s]}. \quad (6.5c)$$

In the above equations,

$$h = \coth(|\beta|H), \quad (6.6a)$$

$$s = \coth(|\beta|S), \quad (6.6b)$$

while the function $f(x)$ is approximated by the trial function

$$f(x) = \begin{cases} 1 + \left(\frac{2x}{w}\right)^3, & -\frac{w}{2} \leq x \leq \frac{w}{2} \\ 0, & \text{otherwise,} \end{cases} \quad (6.7)$$

where w is the width of the line. The capacitance of the unloaded line (C_0) can be computed by substituting $\varepsilon_1 = \varepsilon_2 = 1$ in Eqs. (6.4)-(6.6b), while the capacitance of the loaded line (C) can be computed by substituting $\varepsilon_1 = 10$ and $\varepsilon_2 = v$. The variable v is varied and the corresponding values of ε_{eff} are plotted using Eq. 6.3. In the next step, the resonant frequencies of the ring with and without test material are measured which are F_1 and F_0 , respectively, using a network analyzer. The effective permittivity without the test material, $\varepsilon_{\text{eff0}}$, is calculated by substituting $\varepsilon_1 = 10$, $\varepsilon_2 = 1$ and $S \rightarrow \infty$, in Eqs. (6.3)-(6.7). Afterwards, the effective permittivity in the presence of the test material $\varepsilon_{\text{eff1}}$ is calculated from the following relation:

$$\pi d_m = n \frac{\lambda_0}{\sqrt{\varepsilon_{\text{eff}}}} = n \frac{c}{F_0 \sqrt{\varepsilon_{\text{eff1}}}} = n \frac{c}{F_1 \sqrt{\varepsilon_{\text{eff0}}}}, \quad (6.8)$$

where c is the velocity of light. Using the above relations,

$$\varepsilon_{\text{eff1}} = \varepsilon_{\text{eff0}} \left(\frac{F_0}{F_1} \right)^2. \quad (6.9)$$

Knowing $\varepsilon_{\text{eff}1}$, we can search for ε_2 from the curve plotted by Eq. (6.3).

The procedure used to compute the dielectric constant of a material using the SMS consists of the following steps:

- Measuring the resonance frequencies and 3 dB bandwidth of each resonance using spectrum analyzer (see Fig. 6.6). From these measurements, the constitutive parameters of the dielectric material will be extracted.
- Performing a thru measurement by removing the SMS and interconnecting the coaxial cables from the network analyzer together. This calibration setup is required to eliminate the effect of the cables.
- The software of the SMS system shows two graphs, one with the initially determined attenuation coefficient and the other with the effective relative dielectric constant.
- Accordingly, the software starts to calculate the dielectric constant and loss tangent. This is done by performing EM simulations using the procedure described in this and the following section.
- Finally, the window displays the determined loss tangent and dielectric constant.

6.1.3 Objective (Cost) Function

In the previous section, we have constructed a model for the system and established a relation between the effective permittivity and the measured resonance frequencies. The second step in the optimization procedure is to construct the objective or cost function to minimize the error between the exact and the developed approximate system. This fitting procedure allows us to extract the effective permittivity of the material under test. By substituting (6.5c) in (6.4), and after subtle manipulations, we arrive at

$$\frac{1}{C} = \frac{\varepsilon_2 s}{\pi Q^2 \varepsilon_0 \varepsilon_2 [\varepsilon_2 + \varepsilon_1 h s]} \int_0^\infty \frac{[f(\beta)]^2}{|\beta|} d\beta, \quad (6.10)$$

which is an inhomogeneous integral equation that can be compactly written as

$$L(f) = \frac{1}{C}. \quad (6.11)$$

In the above equation, L is an integral operator defined as

$$L = \frac{\varepsilon_2 s}{\pi Q^2 \varepsilon_0 \varepsilon_2 [\varepsilon_2 + \varepsilon_1 h s]} \int_0^\infty \frac{[\cdot]^2}{|\beta|} d\beta. \quad (6.12)$$

The unknown function f can be discretized as follows:

$$f = \sum_n \alpha_n f_n, \quad (6.13)$$

where $\{f_n\}$ are the basis functions and $\{\alpha_n\}$ are the expansion coefficients. Substituting the above expression in Eq. (6.11), and using the linearity of L , leads to the following expression:

$$\sum_n \alpha_n L(f_n) = \frac{1}{C}, \quad (6.14)$$

An objective function can be constructed and minimized to determine the unknown expansion coefficients $\{\alpha_n\}$, i.e.,

$$\min \left| \sum_n \alpha_n L(f_n) - L(f) \right|, \quad (6.15)$$

where $|\cdot|$, in this case, represents a modulus operator. The above expression can be optimized by a number of existing optimization techniques [23].

6.1.4 Measurement Results

The above mentioned procedure has been brought into practice by measuring the dielectric properties of the Mylar (0.5 mm thickness) and Teflon materials (5 stacked layers of 0.1 mm each) over the frequency band ranging from 500 MHz up to 13 GHz upon assuming that the relative permittivity and tangent delta are independent of frequency, the average measured values are as follows:

Table 6.1: Measured values for Teflon and Mylar

Material Type	Relative Permittivity (F/m)	Tangent Delta (-)
Mylar	2.89	0.007
Teflon	2.03	0.003

HFSS uses for Teflon $\varepsilon_r=2.1$ and $\tan\delta=0.001$, which are similar to the values provided in Table 6.1. For completeness and in accordance with the aforementioned operating principal of the SMS, the measured scattering parameter S_{21} and the associated resonance frequencies in the presence of Mylar and Teflon materials have been depicted in Fig. 6.6.

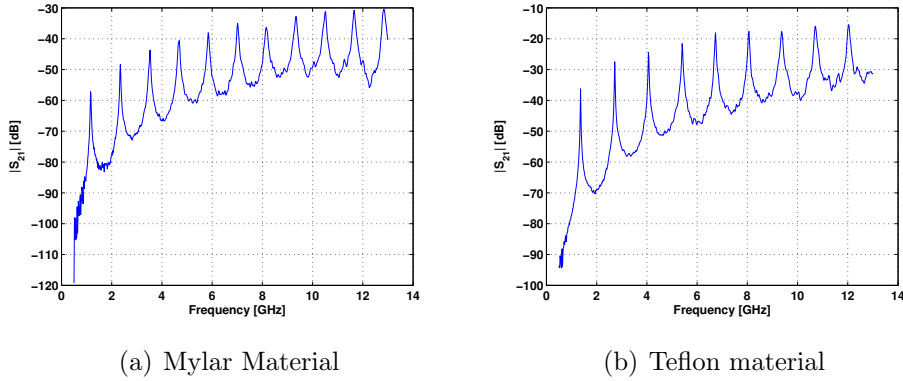


Figure 6.6: Absolute value of the scattering parameter ($|S_{21}|$) versus frequency. Peaks represent the resonance frequencies.

6.2 A Realistically Large Radome Simulation

In the previous chapters, we have focused on the implementation and validation of the MEDM. In this section, we focus on radomes for the radio astronomical applications as alluded to in Chapter 1. The section begins by describing an idealistic antenna array used as a radiation source for illuminating the radome. Afterwards, we present the numerical results—computed through the use of MEDM—and detrimental effect of the radome on the antenna radiation pattern.

6.2.1 Antenna Array Beam

In radar and radio astronomical applications, the primary aim is to point the main beams of the radiation (or receiving) pattern in the desired directions with high precision, while it may be required to place nulls in directions of RF interference sources. Reflector antennas can be used to focus the EM-field from or into a certain direction. However, to steer the

beam using reflector antennas requires the mechanical steering of the reflector antenna itself, which is time consuming as the physical size of these antennas is usually very large. An antenna array, on the other hand, can be used for beam forming and to steer the beam electronically within fractions of seconds.

In the following, we use an array of infinitesimal dipole antenna elements as a radiation source for illuminating the radome with a certain beam. The basic principle is to progressively shift the phase of each antenna element in the array in order to point the antenna beam in the desired direction. For two antenna elements, the resulting field can be expressed mathematically as a superposition of two dipole fields, i.e.,

$$\mathbf{E} = \mathbf{E}_1 e^{-j(\Phi_c + k\mathbf{r}_1 \cdot \hat{\mathbf{r}})} + \mathbf{E}_2 e^{-j(\Phi_c + k\mathbf{r}_2 \cdot \hat{\mathbf{r}})}, \quad (6.16)$$

where, Φ_c is a constant phase offset depending upon the geometrical center of the array, the electric field $\mathbf{E}_n(\theta, \phi)$ represents the embedded element field pattern radiated by the n th dipole and can be computed using the expressions provided in Appendix B, k is the propagation constant, \mathbf{r}_n represents the position of the n th dipole, and $\hat{\mathbf{r}}(\theta_0, \phi_0)$ is a position vector pointing in the main direction (θ_0, ϕ_0) of the array beam. Often, the total radiation pattern \mathbf{E} is expressed in terms of an array factor sum, which can be obtained by manipulating the above expression as follows

$$\begin{aligned} \mathbf{E} &= \mathbf{E}_1 e^{-j(\Phi_c + k\mathbf{r}_1 \cdot \hat{\mathbf{r}})} + \mathbf{E}_2 e^{-j(\Phi_c + k\mathbf{r}_2 \cdot \hat{\mathbf{r}})}, \\ &= e^{-j\Phi_c} [\mathbf{E}_1 e^{-j(k\mathbf{r}_1 \cdot \hat{\mathbf{r}})} + \mathbf{E}_2 e^{-j(k\mathbf{r}_2 \cdot \hat{\mathbf{r}})}]. \end{aligned} \quad (6.17)$$

6.2.2 Numerical Results

The objective of the experiments that have been performed in this section is to simulate a realistically large radome using the MEDM. In this section particular attention is given to study the effect of the radome on the radiation pattern as opposed to focusing on the numerical and/or memory efficiency. For all the experiments listed in this section, the relative permittivity of the material is chosen to be 6, the operating frequency is 1 GHz, and the mesh cell size is $\lambda/50$. The numerical experiments that have been performed are as follows:

Dipole Radiation Pattern in the Presence of a Thin Radome

A relatively thin radome plate of dimensions $1.6\lambda \times 1.6\lambda \times 0.12\lambda$, which is excited by an x -directed infinitesimal dipole placed underneath the radome as depicted in Fig. 6.7(a), has been simulated and the results for the azimuth and elevation patterns of the dipole have been depicted in Figs. 6.7(b) and 6.7(c), respectively. The effect of the presence of

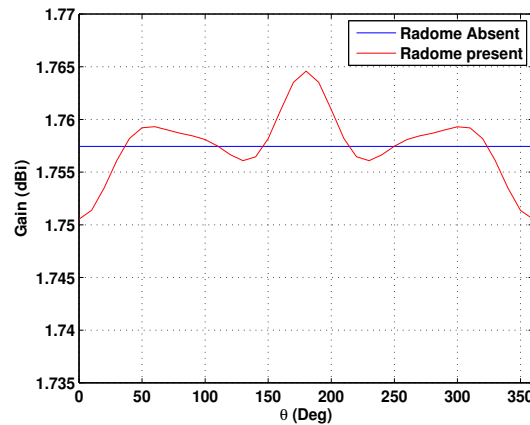
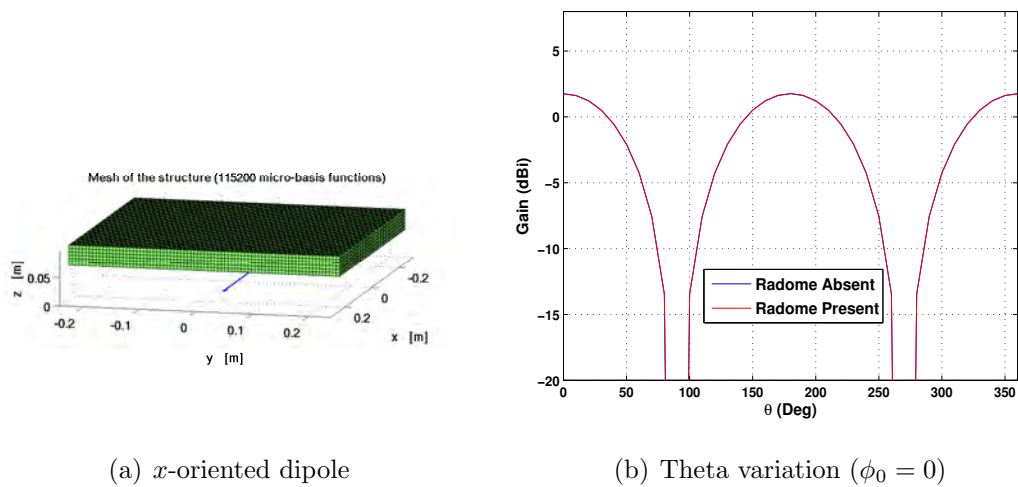


Figure 6.7: Dipole radiation pattern with and without the radome.

the dielectric material is apparent in the azimuthal direction [cf., Fig. 6.7(c)].

Dipole Radiation Pattern in the Presence of a Thick Radome

The above steps are repeated for the above step with a radome plate of dimensions $1.6\lambda \times 1.6\lambda \times 0.36\lambda$ so as to analyze the effect on the radiation pattern for thicker radomes. The results have been depicted in Fig. 6.8. It is evident from Fig. 6.8(c) that the thick

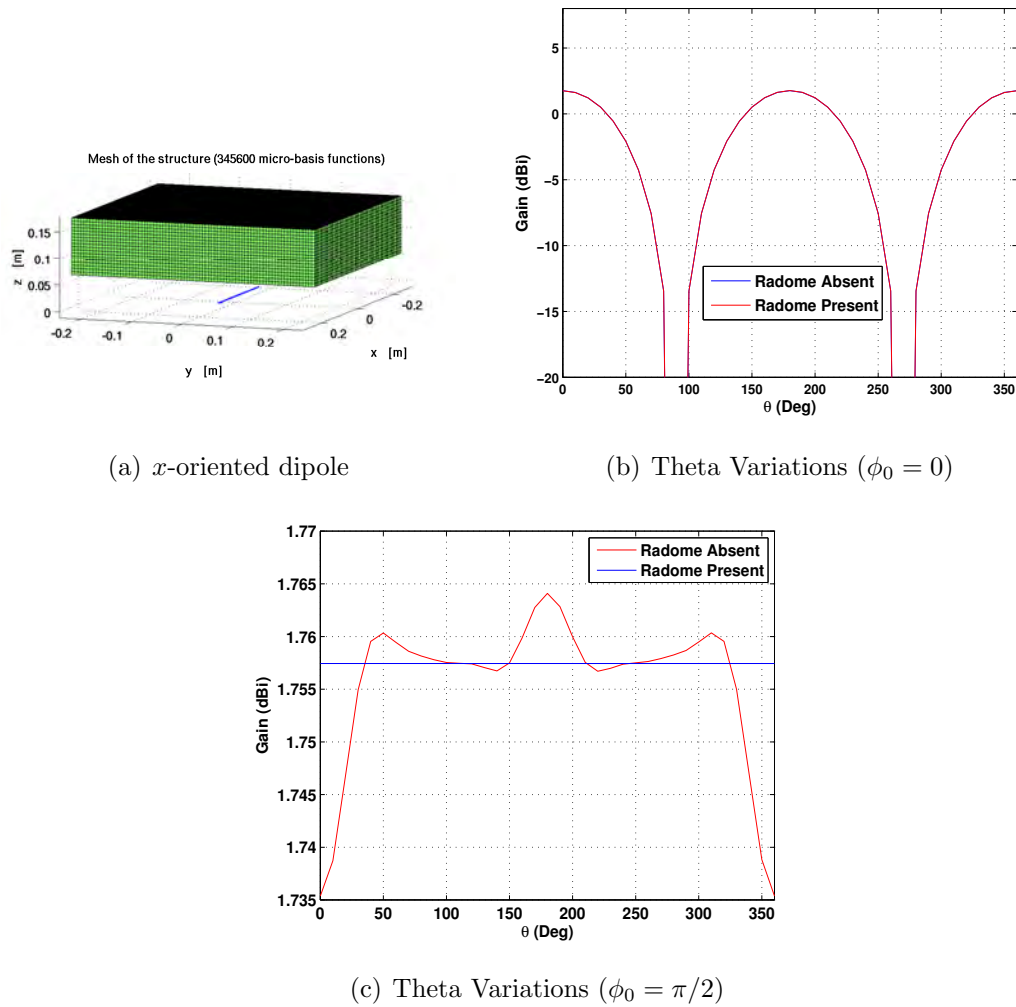


Figure 6.8: Dipole radiation pattern with and without the radome

radome affects the radiation pattern more than the thin radome, as expected. However, the change is minimal in the main beam direction (broadside), but more pronounced for larger elevation angles.

Dipole-Array Radiation Pattern in the Presence of an Electrically Large Radome

In this step, we implement the beam-forming routines for an array of two infinitesimal dipoles illuminating a plate of dimensions $1.6\lambda \times 1.6\lambda \times 0.36\lambda$, which is placed above the dipole array as depicted in Fig. 6.9. The distance between the dipole-array and the plate interface is $\lambda/4$. The antenna array beam is scanned for different azimuthal angles. As

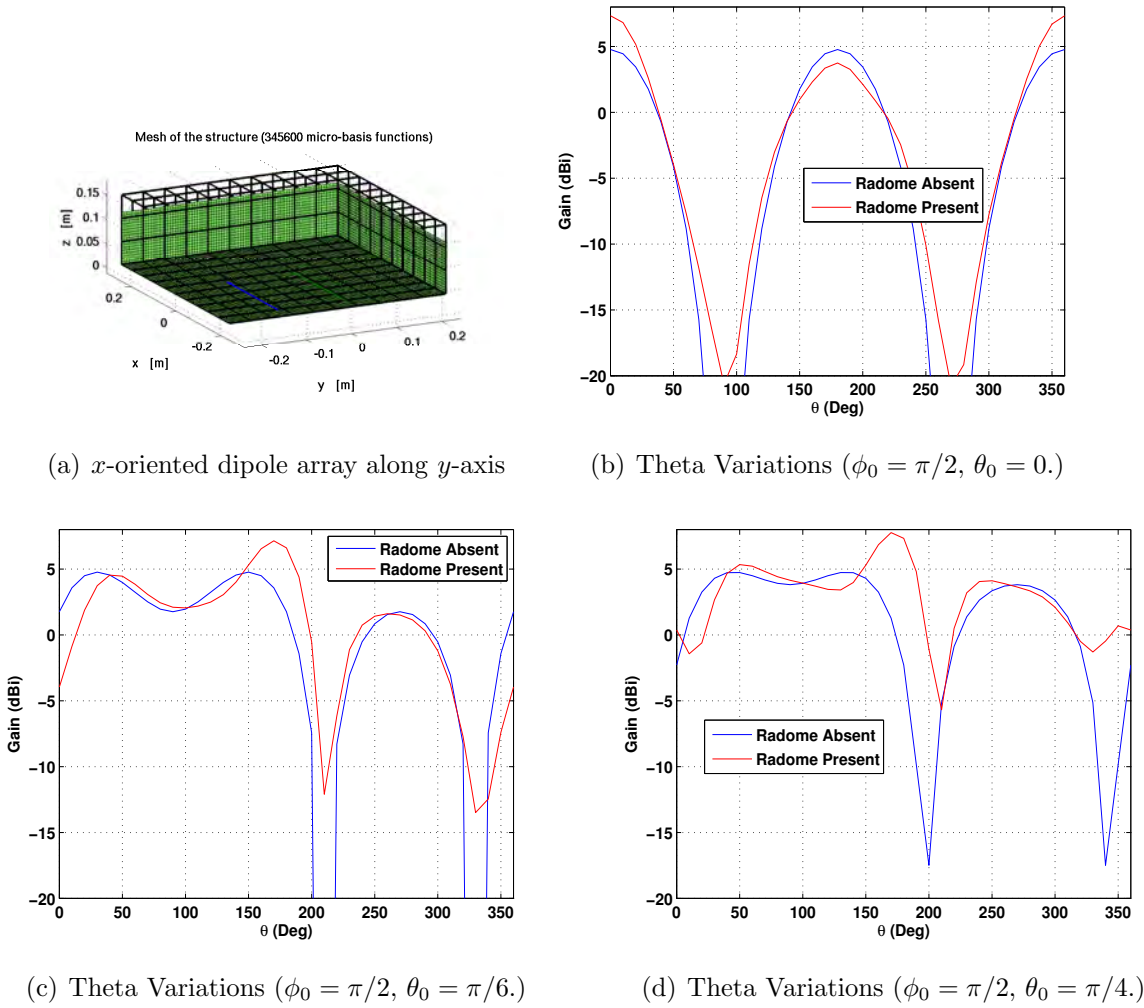


Figure 6.9: Dipole radiation pattern with and without the radome

illustrated in Figs. 6.9(c) and 6.9(d), the effect of the radome on the antenna beam is rather significant when the radome covers most of the radiation by antenna, is relatively thick, and has a large dielectric contrast ($\epsilon = 6$).

Dipole-Array Radiation Pattern in the Presence of a Thin Curved Radome

Next, we simulate an electrically large curved radome of radius = 2λ , thickness = 0.36λ and arc length = 1.6λ with a dipole array placed underneath as shown in Fig. 6.10. A change in

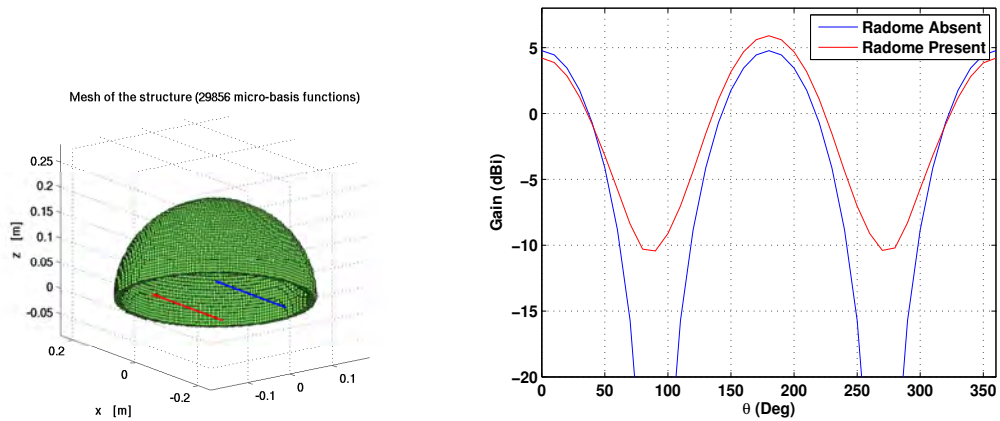
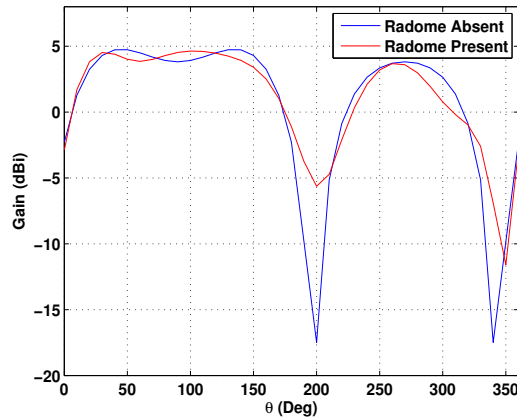
(a) x -oriented dipole array along y -axis(b) Theta Variations ($\phi_0 = \pi/2$, $\theta_0 = 0$.)(c) Theta Variations ($\phi_0 = \pi/2$, $\theta_0 = \pi/4$.)

Figure 6.10: Dipole radiation pattern with and without the curved radome.

the amplitude of the field is observed in the elevation direction, whereas in the azimuthal direction, both the amplitude and the beam pointing direction is distorted.

Dipole-Array Radiation Pattern in the Presence of a Thick Curved Radome

As a last step, we simulate a realistically large curved radome with dipole array placed underneath as shown in Fig. 6.11. As evident from Fig. 6.11, an increase in the radome-

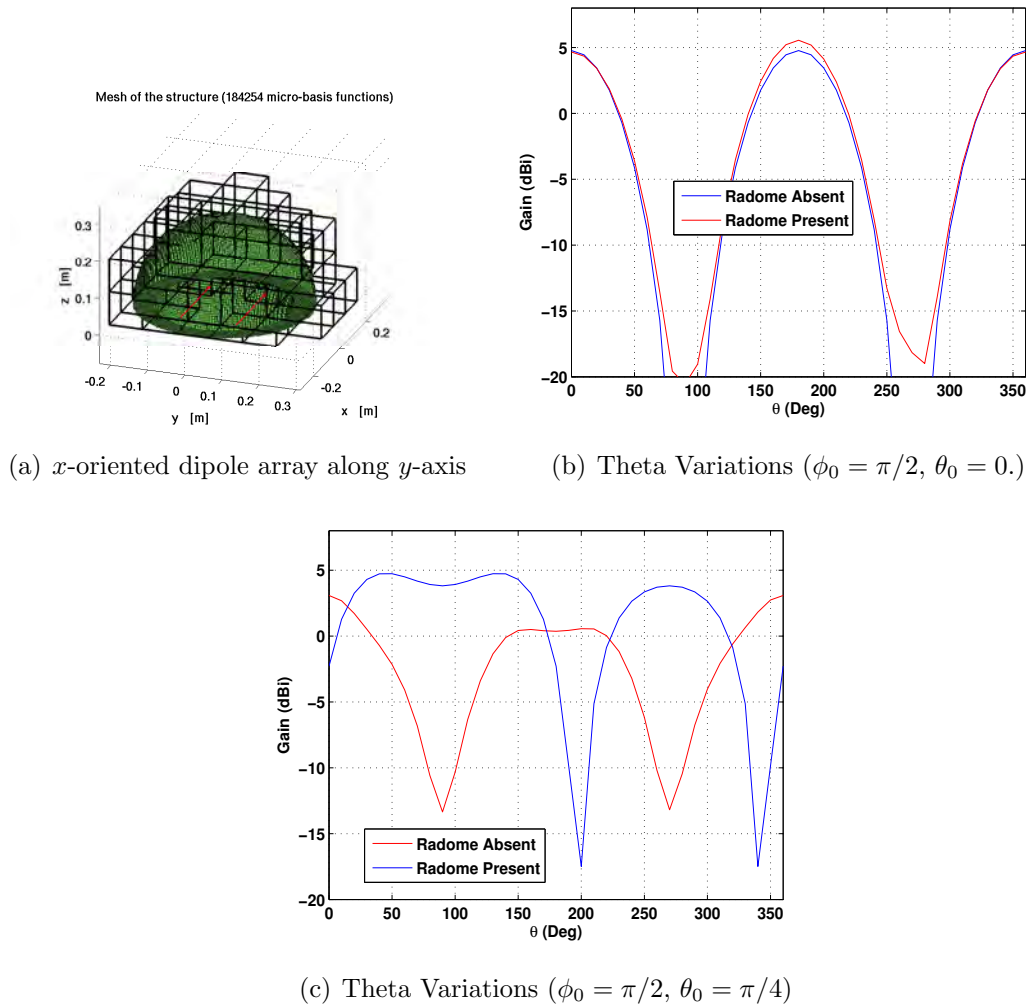


Figure 6.11: Dipole radiation pattern with and without the curved radome.

thickness leads to an increased distortion in the antenna actual radiation pattern and increased beam pointing error as compared to the thin radome.

6.3 Conclusions

In this chapter, we have described the operational principle of the permittivity and loss tangent measurement system for dielectric materials. The values of permittivity for the Mylar and Teflon radome materials are measured and compared to the constitutive parameter values provided by HFSS. Furthermore, the field scattered by several radomes have been analyzed whose scattering effect of this scattering, on the resulting beam, is observed. The detrimental effect of the radome on antenna beam can be significant if the objective is to accurately point the antenna beam into a specific direction, particularly for off-broadside scan angles, thick radomes, and for radomes having a large dielectric contrast.

Chapter 7

Conclusions and Recommendations

7.1 Conclusions

In this thesis, we started with an introductory chapter describing some background information on radomes for electromagnetic antennas, provided a motivation into the thesis subject by introducing the Square Kilometer Array (SKA) radio telescope, and stressed the importance of employing radomes for the SKA design. Afterwards, we briefly reviewed the most prominent existing computational methods for solving electromagnetic (radiation and scattering) problems.

Thereafter, in Chapter 2, we formulated and discretized the Electric Field Integral Equation (EFIE) using the method of weighted residuals. This discretization has led us to a moment matrix equation, which can be solved for the unknown current. Before doing so, we made an explicit choice of basis and test functions; we have chosen to employ low-order micro-domain basis functions because they are potentially well-suited to model fine details in the current, while the numerical implementation is straightforward. The equivalent dipole moment of a micro-domain basis function has been derived for the representation of the field external to the source basis function. The self-term is calculated by testing the scattered field at the center of the source cube. The scattered field value in the center of

the remaining cubes (i.e. coupling-terms) have been determined through the dipole field representation. This allows us to establish regular closed-form expressions for the moment matrix elements which can be evaluated rapidly and in a direct numerical manner.

Following the formulation and implementation of the method, the method is then validated against analytically-known scattering solutions, and compared to existing numerical softwares. For this purpose, the Mie-series has been formulated mathematically and its implementation has been validated by comparing the solution to published results that are available in the literature. In addition, we have simulated the results in HFSS. Overall, the results obtained via the presented MEDM code are in good agreement with the exact solution and the HFSS results, despite the simplicity of the numerical scheme. Furthermore, the solution is computed faster and requires less amounts of memory. Finally, it has been verified numerically (through a convergence study) that a subdivision of the source cube into smaller source cubes does not lead to a significant improvement in the accuracy of the computed radiated field at neighboring observation cubes.

From a theoretical standpoint, we have formulated and implemented a novel numerical Computational Electromagnetic (CEM) method for the accurate solution of dielectric scattering problems. However, employing electrically small basis functions inevitably causes memory storage problems and excessively long simulation times. To overcome these memory and time inefficiency problems, the CBFM and the ACA algorithm have been described, and used to enhance the plain MEDM code. It has been demonstrated—through various examples—that the MEDM with EETs employed reduces the memory storage requirements and increases the time efficiency with only a subtle compromise on the solution accuracy. There is no hard limit on the size of the problem, since this merely depends on the available memory resources and processor specifications; we have successfully solved electrically large scattering problems, among which a dielectric sphere of radius $\lambda/6$.

Chapter 6, contains a description of the permittivity and loss tangent measurement system for dielectric materials. The complex-valued permittivity for Mylar and Teflon materials have been measured and compared to those specified in the HFSS software. Finally, the field scattered by a radome has been analyzed and the effect of this scattering on the resulting antenna phased-array beam has been examined. It is concluded that the effect of the radome on the antenna beam can be relatively large if accurately beam-pointing is required, particularly for thick radomes, off-broadside scan angles, and radomes of high dielectric contrast. In these cases the radome must be taken into account during the

electromagnetic design phase of the antenna system.

7.2 Recommendations

Although we have focused on making the presented method as optimal as possible, we believe that the proposed method can be improved further. The following itemization describes our findings and research curiosities as recommendations which may help to improve and extend the numerical method in future. Also, these recommendations can be effectuated and be an input for a future PhD project. The suggestions are as follows:

- The glitch in the field at the surface of the sphere in Fig. 4.5(a) is a result of spurious charges at the boundary surface of the sphere as described in Chapter 4. It is worthwhile to examine whether this spurious surface charge can be mitigated by introducing more than three degrees of freedom for the basis function current in a micro cube.
- Secondly, the CBFM—as implemented during this project—represents a monolevel version of CBFM. The multilevel implementation of CBFM can result into a fast solution of problems that are even electrically larger, at a reduced computational cost and at a reduced solution time, relative to a monolevel approach.
- Although we have established a short discussion about the scattering analysis of combined antenna-radome problems, a more detailed analysis is required to accurately quantify the detrimental effect of radomes on the antenna performance. It is desired that beam pointing errors incurred by the presence of radome can be predicted in advance and possibly be compensated for in an early stage of the antenna design process.
- The volume equivalent currents employed in MEDM can be combined with the surface equivalent currents in CAESAR to develop a hybrid formulation for solving entire antenna-radome problems. This capability also enables us to design antenna arrays in the presence of a radome.

As a final note, it is worth pointing out that this work has been published at the International Conference on Electromagnetics and Advanced Applications (ICEAA) [44]:

M. Naeem, R. Maaskant, G. W. Kant, P.-S. Kildal, and R. Mittra, “The method of equivalent dipole moments (MEDM) combined with CBFM for the fast and accurate solution of dielectric scattering problems”, *International Conference on Electromagnetics and Advanced Applications (ICEAA)*, Sep. 2011.

Appendix A

Field in the Center of the Cube

A.1 Scattered Field Evaluation

Here, we evaluate the integral terms involved in (3.9), one by one, for simplicity and substitute the simplified forms back to have an integral free expression for the scattered field in the center of the microdomain cube. The first integral in (3.9) is evaluated as

$$\iint_{\partial\mathcal{V}} \hat{\mathbf{r}}' \cdot \hat{\mathbf{n}} \, dS' = \sum_i \iint_{\partial_i\mathcal{V}} \frac{\mathbf{r}'}{|\mathbf{r}'|} \cdot \hat{\mathbf{n}}_i \, dS', \quad (\text{A.1})$$

where the sum of integrals over $\partial_i\mathcal{V}$ indicates that all faces of the cube are integrated separately and then summed. For the face \mathcal{S}_y^+ at $y = a/2$, for instance,

$$\begin{aligned} \iint_{\mathcal{S}_y^+} \frac{\mathbf{r}'}{|\mathbf{r}'|} \cdot \hat{\mathbf{y}} \, dS' &= \hat{\mathbf{y}} \cdot \int_{-a/2}^{a/2} \int_{-a/2}^{a/2} \frac{x' \hat{\mathbf{x}} + (a/2) \hat{\mathbf{y}} + z' \hat{\mathbf{z}}}{\sqrt{x'^2 + (a/2)^2 + z'^2}} \, dx' \, dz' \\ &= \left(\frac{a}{2}\right) \int_{-a/2}^{a/2} \int_{-a/2}^{a/2} \frac{1}{\sqrt{x'^2 + (a/2)^2 + z'^2}} \, dx' \, dz' = \left(\frac{a}{2}\right) \iint_{\mathcal{S}_{y+}} \frac{1}{R} \, dS'. \end{aligned} \quad (\text{A.2})$$

This last integral can be evaluated with the aid of [26, Eq. (5)], where we will now have a “residue” contribution, unlike it was the case for the volume integration in (3.7). The

evaluation proceeds as follows,

$$\iint_{\mathcal{S}_y^+} \frac{1}{R} dS' = \lim_{\varepsilon \rightarrow 0} \iint_{\mathcal{S}_y^+ - \mathcal{S}_\varepsilon} \nabla'_s \cdot \left(\frac{R}{P} \hat{\mathbf{P}} \right) dS' + \lim_{\varepsilon \rightarrow 0} \iint_{\mathcal{S}_\varepsilon} \frac{1}{R} dS', \quad (\text{A.3})$$

where \mathcal{S}_ε is a small circular area excluded from the face of the cube at $y = a/2$, i.e. $\mathcal{S}_\varepsilon \subset \mathcal{S}_y^+$, with center $(x = 0, y = a/2, z = 0)$ and radius ε . Here, $P = |\boldsymbol{\rho}'|$, $\hat{\mathbf{P}} = \boldsymbol{\rho}'/P$, and $\boldsymbol{\rho}' = x'\hat{\mathbf{x}} + z'\hat{\mathbf{z}}$. One readily concludes that the last integral amounts to zero, since

$$\lim_{\varepsilon \rightarrow 0} \iint_{\mathcal{S}_\varepsilon} \frac{1}{R} dS' = \lim_{\varepsilon \rightarrow 0} \int_0^{2\pi} \int_0^\varepsilon \frac{P}{\sqrt{P^2 + (a/2)^2}} dP d\varphi = \lim_{\varepsilon \rightarrow 0} 2\pi(\sqrt{\varepsilon^2 + (a/2)^2} - \sqrt{(a/2)^2}) = 0. \quad (\text{A.4})$$

Using Gauss' theorem for surfaces, that is,

$$\iint_S \nabla'_s \cdot \mathbf{A}_s dS' = \oint_{\partial S} \mathbf{A}_s \cdot \hat{\mathbf{m}} dl', \quad (\text{A.5})$$

where $\hat{\mathbf{m}}$ is pointing outwards along the closed contour, the other integral in (A.3) is evaluated as

$$\begin{aligned} \lim_{\varepsilon \rightarrow 0} \iint_{\mathcal{S}_y^+ - \mathcal{S}_\varepsilon} \nabla'_s \cdot \left(\frac{R}{P} \hat{\mathbf{P}} \right) dS' &= \oint_{\partial \mathcal{S}_y^+} \left(\frac{R}{P} \hat{\mathbf{P}} \right) \cdot \hat{\mathbf{m}} dl' - \lim_{\varepsilon \rightarrow 0} \oint_{\partial \mathcal{S}_\varepsilon} \left(\frac{R}{P} \hat{\mathbf{P}} \right) \cdot \hat{\mathbf{P}} dl' \\ &= \sum_{j=1}^4 \int_{\ell_y^{+,j}} \frac{R}{P} \hat{\mathbf{P}} \cdot \hat{\mathbf{m}}_j dl' - 2\pi \lim_{\varepsilon \rightarrow 0} \varepsilon \frac{\sqrt{(a/2)^2 + \varepsilon^2}}{\varepsilon} \\ &= \sum_{j=1}^4 \int_{\ell_y^{+,j}} \left(\frac{1}{R} + \frac{(a/2)^2}{P^2 R} \right) \boldsymbol{\rho}' \cdot \hat{\mathbf{m}}_j dl' - a\pi, \end{aligned} \quad (\text{A.6})$$

where we integrate over the 4 line segments of the face at $y = a/2$ and sum their contributions. The segment $\ell_y^{+,j}$ is the j th segment at $y = a/2$. The term $\boldsymbol{\rho}' \cdot \hat{\mathbf{m}}_j = a/2$. The first line integral in (A.6) is written as

$$\sum_{j=1}^4 \int_{\ell_y^{+,j}} \frac{1}{R} dl' = 4 \int_{\ell' = -a/2}^{a/2} \frac{1}{\sqrt{(a/2)^2 + (a/2)^2 + \ell'^2}} dl' = 4 \ln \left(\frac{\sqrt{3} + 1}{\sqrt{3} - 1} \right) \quad (\text{A.7})$$

and the second line integral as

$$\begin{aligned} \sum_{j=1}^4 \int_{\ell_y^{+,j}} \frac{1}{P^2 R} d\ell' &= 4 \int_{\ell'=-a/2}^{a/2} \frac{1}{[(a/2)^2 + \ell'^2] \sqrt{(a/2)^2 + (a/2)^2 + \ell'^2}} d\ell' \\ &= \frac{32}{a^2} \arctan \left(\frac{1}{\sqrt{3}} \right), \end{aligned} \quad (\text{A.8})$$

where we have used that

$$\int \frac{1}{[d^2 + x^2] \sqrt{2d^2 + x^2}} dx = \frac{1}{d^2} \arctan \left(\frac{x}{\sqrt{2d^2 + x^2}} \right). \quad (\text{A.9})$$

Substituting (A.8) and (A.7) in (A.6), and then in (A.3), and (A.2), yields

$$\iint_{S_y^+} \hat{\mathbf{r}}' \cdot \hat{\mathbf{n}} dS' = a^2 \left[\ln \left(\frac{\sqrt{3} + 1}{\sqrt{3} - 1} \right) + 2a^2 \arctan \left(\frac{1}{\sqrt{3}} \right) - \frac{1}{2}\pi \right]. \quad (\text{A.10})$$

The flux that we have calculated through the face at $y = a/2$ is equal for all the six faces. Hence, we have in (A.1) that

$$\iint_{\partial \mathcal{V}} \hat{\mathbf{r}}' \cdot \hat{\mathbf{n}} dS' = a^2 \left[6 \ln \left(\frac{\sqrt{3} + 1}{\sqrt{3} - 1} \right) + 12a^2 \arctan \left(\frac{1}{\sqrt{3}} \right) - 3\pi \right]. \quad (\text{A.11})$$

Next, we will evaluate the last two integral expressions in (3.9). On the basis of symmetry, we have for the face S^+ at $z = a/2$ that

$$\begin{aligned} \iint_{S^+} \frac{\hat{\mathbf{r}}'}{r'^2} dS' &= \int_{-a/2}^{a/2} \int_{-a/2}^{a/2} \frac{x' \hat{\mathbf{x}} + y' \hat{\mathbf{y}} + (a/2) \hat{\mathbf{z}}}{[x'^2 + y'^2 + (a/2)^2]^{3/2}} dx' dy' \\ &= \hat{\mathbf{z}} \left(\frac{a}{2} \right) \int_{-a/2}^{a/2} \int_{-a/2}^{a/2} \frac{1}{[x'^2 + y'^2 + (a/2)^2]^{3/2}} dx' dy' = \hat{\mathbf{z}} \left(\frac{a}{2} \right) \iint_{S^+} \frac{1}{R^3} dS'. \end{aligned} \quad (\text{A.12})$$

This last integral can be evaluated using [25, Eq. (26)]. Taking for the present case that $\boldsymbol{\rho}' = x' \hat{\mathbf{x}} + y' \hat{\mathbf{y}}$, $R = \sqrt{x'^2 + y'^2 + (a/2)^2}$, $P = \sqrt{x'^2 + y'^2}$, and $\hat{\mathbf{P}} = \boldsymbol{\rho}'/P$, one can express (A.12) as

$$\iint_{S^+} \frac{1}{R^3} dS' = \lim_{\varepsilon \rightarrow 0} \iint_{S_\varepsilon} \frac{1}{R^3} dS' - \lim_{\varepsilon \rightarrow 0} \iint_{S^+ - S_\varepsilon} \nabla'_s \cdot \left(\frac{\hat{\mathbf{P}}}{PR} \right) dS', \quad (\text{A.13})$$

which can be simplified using Gauss' theorem to

$$\iint_{S^+} \frac{1}{R^3} dS' = \lim_{\varepsilon \rightarrow 0} \iint_{S_\varepsilon} \frac{1}{R^3} dS' - \oint_{\partial S^+} \left(\frac{\hat{\mathbf{P}}}{PR} \right) \cdot \hat{\mathbf{m}} d\ell' + \lim_{\varepsilon \rightarrow 0} \oint_{\partial S_\varepsilon} \left(\frac{\hat{\mathbf{P}}}{PR} \right) \cdot \hat{\mathbf{P}} d\ell'. \quad (\text{A.14})$$

The first term on the right-hand-side is evaluated as

$$\lim_{\varepsilon \rightarrow 0} \iint_{S_\varepsilon} \frac{1}{R^3} dS' = \lim_{\varepsilon \rightarrow 0} \int_0^{2\pi} \int_0^\varepsilon \frac{P}{[P^2 + (a/2)^2]^{3/2}} dP d\varphi = 2\pi \lim_{\varepsilon \rightarrow 0} \left[\frac{2}{\sqrt{a^2}} - \frac{2}{\sqrt{a^2 + 4\varepsilon^2}} \right] = 0, \quad (\text{A.15})$$

and the last term on the right-hand-side is evaluated as

$$\lim_{\varepsilon \rightarrow 0} \oint_{\partial S_\varepsilon} \left(\frac{\hat{\mathbf{P}}}{PR} \right) \cdot \hat{\mathbf{P}} d\ell' = \lim_{\varepsilon \rightarrow 0} \oint_{\partial S_\varepsilon} \left(\frac{1}{PR} \right) d\ell' = 2\pi \lim_{\varepsilon \rightarrow 0} \frac{\varepsilon}{\varepsilon(\sqrt{\varepsilon^2 + (a/2)^2})} = \frac{4\pi}{a}, \quad (\text{A.16})$$

and the middle term on the right-hand-side as

$$\oint_{\partial S^+} \left(\frac{\hat{\mathbf{P}}}{PR} \right) \cdot \hat{\mathbf{m}} d\ell' = \left(\frac{a}{2} \right) \oint_{\partial S^+} \left(\frac{1}{P^2 R} \right) d\ell' = \frac{16}{a} \arctan \left(\frac{1}{\sqrt{3}} \right), \quad (\text{A.17})$$

where we made use of (A.8). Substituting the preceding results back in (A.12), yields

$$\iint_{S^+} \frac{\hat{\mathbf{r}}'}{r'^2} dS' = - \iint_{S^-} \frac{\hat{\mathbf{r}}'}{r'^2} dS' = \hat{\mathbf{z}} \left[2\pi - 8 \arctan \left(\frac{1}{\sqrt{3}} \right) \right]. \quad (\text{A.18})$$

Finally, Eqs. (A.18) and (A.11) are substituted in (3.9) to give the scattered field at the origin, i.e.,

$$\mathbf{E}^s(\mathbf{r} = \mathbf{0}, \mathbf{J}_{\text{eq}}) = \hat{\mathbf{z}} \left[-j\omega\mu_0 a^2 \left[\frac{3}{4\pi} \ln \left(\frac{\sqrt{3}+1}{\sqrt{3}-1} \right) + \frac{3}{2\pi} a^2 \arctan \left(\frac{1}{\sqrt{3}} \right) - \frac{3}{8} \right] - \frac{1}{j\omega\varepsilon_0} \left[1 - \frac{4}{\pi} \arctan \left(\frac{1}{\sqrt{3}} \right) \right] \right]. \quad (\text{A.19})$$

A.2 Contribution of the Second Taylor Term

To arrive at (3.11), we add Adding the second Taylor term ($-jk_0R$) to (2.17) for the basis function $\mathbf{J}_{\text{eq}}(\mathbf{r}') = \mathbf{f}_n(\mathbf{r}')$, which results in the following:

$$\begin{aligned}
\mathbf{E}^s(\mathbf{f}_n)|_{2T} &= -j\omega\mu_0 \iiint_V \mathbf{f}_n(\mathbf{r}') \frac{-jk_0|\mathbf{r} - \mathbf{r}'|}{4\pi|\mathbf{r} - \mathbf{r}'|} dV' & (\text{A.20}) \\
&\quad - \frac{1}{j\omega\varepsilon_0} \iiint_V \nabla' \cdot \mathbf{f}_n(\mathbf{r}') \nabla' \left(\frac{-jk_0|\mathbf{r} - \mathbf{r}'|}{4\pi|\mathbf{r} - \mathbf{r}'|} \right) dV' \\
&= -\frac{\omega\mu_0 k_0}{4\pi} \iiint_V \mathbf{f}_n(\mathbf{r}') dV' + 0 \\
&= -\frac{\omega\mu_0 k_0}{4\pi} \iiint_V \hat{\mathbf{z}} dV' \\
&= -\frac{\omega\mu_0 k_0}{4\pi} a^3 \hat{\mathbf{z}}, & (\text{A.21})
\end{aligned}$$

where $\mathbf{E}^s(\mathbf{f}_n)|_{2T}$ denotes the scattered field due to second taylor term.

Appendix B

Field of an Infinitesimal Dipole

The field of an infinitesimal dipole is derived in this section. By substituting (2.11) in (2.9), we have that

$$\mathbf{E} = \frac{1}{j\omega\epsilon_0} [\nabla (\nabla \cdot \mathbf{A}) + k_0^2 \mathbf{A}]. \quad (\text{B.1})$$

The solution of this equation can be found by substituting the current density for the infinitesimal dipole, $\mathbf{J}_{\text{eq}}(\mathbf{r}') = Il\hat{\mathbf{z}}\delta(x')\delta(y')\delta(z')$, in (2.13) as

$$\begin{aligned} \mathbf{A} &= \iiint_{V_\infty} \mathbf{J}_{\text{eq}}(\mathbf{r}') \frac{e^{-jk_0|\mathbf{r}-\mathbf{r}'|}}{4\pi|\mathbf{r}-\mathbf{r}'|} dV' \\ &= \frac{Il}{4\pi} \hat{\mathbf{z}} \frac{e^{-jk_0|\mathbf{r}|}}{|\mathbf{r}|}. \end{aligned} \quad (\text{B.2})$$

Substituting (B.2) in (B.1), gives the following expression for the field:

$$\mathbf{E} = \frac{Il}{4\pi j\omega\epsilon_0} \left[\nabla \left(\nabla \cdot \hat{\mathbf{z}} \frac{e^{-jk_0|\mathbf{r}|}}{|\mathbf{r}|} \right) + k_0^2 \hat{\mathbf{z}} \frac{e^{-jk_0|\mathbf{r}|}}{|\mathbf{r}|} \right]. \quad (\text{B.3})$$

The different terms in the above expression are solved separately as follows:

$$\begin{aligned} \nabla \cdot \hat{\mathbf{z}} \frac{e^{-jk_0|\mathbf{r}|}}{|\mathbf{r}|} &= \frac{\partial}{\partial z} \frac{e^{-jk_0|\mathbf{r}|}}{|\mathbf{r}|} \\ &= - \left[\frac{1}{|\mathbf{r}|^3} + \frac{jk}{|\mathbf{r}|^2} \right] ze^{-jk_0|\mathbf{r}|}, \end{aligned} \quad (\text{B.4})$$

$$\begin{aligned} \nabla \left(-\frac{1}{|\mathbf{r}|^3} z e^{-jk_0|\mathbf{r}|} \right) &= e^{-jk_0|\mathbf{r}|} \left[\left(\frac{3xz}{|\mathbf{r}|^5} + \frac{jk_0xz}{|\mathbf{r}|^4} \right) \hat{\mathbf{x}} + \dots \right. \\ &\quad \left. \left(\frac{3yz}{|\mathbf{r}|^5} + \frac{jk_0yz}{|\mathbf{r}|^4} \right) \hat{\mathbf{y}} + \dots \right. \\ &\quad \left. \left(\frac{3z^2}{|\mathbf{r}|^5} + \frac{jk_0z^2}{|\mathbf{r}|^4} - \frac{1}{|\mathbf{r}|^3} \right) \hat{\mathbf{z}} \right], \end{aligned} \quad (\text{B.5})$$

$$\begin{aligned} \nabla \left(-\frac{jk}{|\mathbf{r}|^2} z e^{-jk_0|\mathbf{r}|} \right) &= e^{-jk_0|\mathbf{r}|} \left[\left(\frac{2jk_0xz}{|\mathbf{r}|^4} - \frac{k_0^2xz}{|\mathbf{r}|^3} \right) \hat{\mathbf{x}} + \dots \right. \\ &\quad \left(\frac{2jk_0yz}{|\mathbf{r}|^4} - \frac{k_0^2yz}{|\mathbf{r}|^3} \right) \hat{\mathbf{y}} + \dots \\ &\quad \left. \left(\frac{2jk_0z^2}{|\mathbf{r}|^4} - \frac{k_0^2z^2}{|\mathbf{r}|^3} - \frac{jk_0}{|\mathbf{r}|^2} \right) \hat{\mathbf{z}} \right]. \end{aligned} \quad (\text{B.6})$$

Substituting the above terms in (B.3), and after re-arranging, one obtains

$$E_x = \frac{IlC}{4\pi j\omega\varepsilon_0} x z e^{-jk_0|\mathbf{r}_{mn}|}, \quad (\text{B.7a})$$

$$E_y = \frac{IlC}{4\pi j\omega\varepsilon_0} y z e^{-jk_0|\mathbf{r}_{mn}|}, \quad (\text{B.7b})$$

$$E_z = \frac{Il}{4\pi j\omega\varepsilon_0} \left[C_{mn} z^2 + \frac{k_0^2}{|\mathbf{r}_{mn}|} - \frac{jk_0}{|\mathbf{r}_{mn}|^2} - \frac{1}{|\mathbf{r}_{mn}|^3} \right] e^{-jk_0|\mathbf{r}_{mn}|}, \quad (\text{B.7c})$$

where

$$C_{mn} = -\frac{k_0^2}{|\mathbf{r}_{mn}|^3} + \frac{3jk_0}{|\mathbf{r}_{mn}|^4} + \frac{3}{|\mathbf{r}_{mn}|^5}$$

and where the radiated field outside the source cube is

$$\mathbf{E}(\mathbf{r}) = [E_x \hat{\mathbf{x}} + E_y \hat{\mathbf{y}} + E_z \hat{\mathbf{z}}]. \quad (\text{B.8})$$

Bibliography

- [1] A. W. Rudge, K. Milne, A. D. Olver, and P. Knight, *The Handbook of Antenna Design*. Peter Peregrinus Ltd., London, UK., 1983, vol. 2.
- [2] Website:, “www.skatelescope.org.”
- [3] P. J. Hall, Ed., *The Square Kilometre Array: An Engineering Perspective*. Springer, 2005.
- [4] C. Tiantian and D. Wenbin, “Analysis of radome at millimeter wavelengths,” *Millimeter Wave Systems*, vol. 1, 2006.
- [5] V. B. Yurchenko and A. Altintas, “Numerical optimization of a cylindrical reflector-in-radome antenna system,” *IEEE Trans. Antennas Propag.*, vol. 47, no. 4, Apr. 1999.
- [6] A. Bondeson, T. Rylander, and P. Ingelstrom, *Computational Electromagnetics*. Springer, 2005.
- [7] M. N. O. Sadiku, *Numerical Techniques in Electromagnetics*, 2nd ed. CRC Press, 2001.
- [8] D. G. Swanson, J. Wolfgang, and J. R. Hoefe, *Microwave Circuit Modeling Using Electromagnetic Field Simulation*. Artech House Boston, London, 2003.
- [9] K. S. Yee, “Numerical solution of initial boundary value problems involving maxwell’s equations in isotropic media,” *IEEE Trans. Antennas Propag.*, vol. AP-14, no. 3, May 1966.
- [10] R. F. Harrington, *Field Computation by Moment Methods*. New York: The MacMillan Company, 1968.

-
- [11] Website:, “<http://www.ansoft.com/products/hf/hfss/>.”
- [12] —, “<http://www.feko.info/>.”
- [13] R. Maaskant, “Analysis of large antenna systems,” Ph.D. dissertation, Eindhoven University of Technology, 2010.
- [14] R. Mittra and et al. et al., “A universal dipole-moment-based approach for formulating mom-type problems without the use of green’s functions,” *Proc. of the 4th Europ. Conf. on Antennas and Propagat. (EuCAP)*, pp. 1–3, Apr. 2010.
- [15] R. Olsson, P.-S. Kildal, and S. Weinreb, “The eleven antenna: A compact low-profile decade bandwidth dual polarized feed for reflector antennas,” *IEEE Trans. Antennas Propag.*, vol. 54, no. 2, Feb. 2006.
- [16] J. A. Stratton, *Electromagnetic Theory*. McGRAW-HILL, 1941.
- [17] C. A. Balanis, *Advanced Engineering Electromagnetics*. New York: John Wiley and Sons, Inc., 1989.
- [18] S. M. Rao and D. R. Wilton, “Electromagnetic scattering by surfaces of arbitrary shape,” *IEEE Trans. Antennas Propag.*, vol. AP-30, no. 3, May 1982.
- [19] R. F. Harrington, *Time-Harmonic Electromagnetic Fields*. McGRAW-HILL, 1961.
- [20] B. A. Finlayson, *The Method of Weighted Residuals and Variational Principles With Applications in Fluid Mechanics, Heat and Mass Transfer*. Academic Press, INC, 1972, vol. 87.
- [21] T. K. Sarkar, A. R. Djordjevic, and E. Arvas, “On the choice of expansion and weighting functions in the numerical solution of operator equations,” *IEEE Trans. Antennas Propag.*, vol. AP-33, no. 9, Sep. 1985.
- [22] J. S. and, “Direct solvers for the second and fourth order equations using legendre polynomials,” *SIAM J. Sci. Comp.*, no. 15, pp. 1489–1505, 1994.
- [23] P. E. Gill, W. Murray, and M. H. Wright, *Practical Optimization*. Academic Press, INC, 1981.
- [24] T. K. Sarkar, “A note on the choice weighting functions in the method of moments,” *IEEE Trans. Antennas Propag.*, vol. AP-33, no. 4, Apr. 1985.

- [25] R. D. Graglia, "On the numerical integration of the linear shape functions times the 3-D Green's function or its gradient on a plane triangle," *IEEE Trans. Antennas Propag.*, vol. 41, no. 10, pp. 1448–1455, Oct. 1993.
- [26] D. R. Wilton, S. M. Rao, A. W. Glisson, D. H. Schaubert, O. M. Al-Bundak, and C. M. Butler, "Potential integrals for uniform and linear source distributions on polygonal and polyhedral domains," *IEEE Trans. Antennas Propag.*, vol. 32, no. 3, pp. 276–281, Mar. 1984.
- [27] J. F. White, *HIGH FREQUENCY TECHNIQUES—An Introduction to RF and Microwave Engineering*. John Wiley & Sons, Inc., 2004.
- [28] X. Yuan, "Three-dimensional electromagnetic scattering from inhomogeneous objects by the hybrid moment and finite element method," *IEEE Trans. Antennas Propag.*, vol. 38, no. 8, pp. 1053–1058, Aug. 1990.
- [29] Website:, "<http://www.wipl-d.com/>."
- [30] M. Kerker, *The Scattering of Light and Other Electromagnetic Radiation*. Academic Press, INC, 1969, vol. 16.
- [31] R. Maaskant, R. Mittra, and A. Tijhuis, "Fast analysis of large antenna arrays using the characteristic basis function method and the adaptive cross approximation algorithm," *IEEE Trans. Antennas Propag.*, vol. 56, no. 11, 2008.
- [32] M. Bebendorf, "Approximation of boundary element matrices," *Numer. Math.*, vol. 86, no. 4, pp. 565–589, Jun. 2000.
- [33] E. Lucente, G. Tiberi, A. Onorchio, G. Manara, and R. Mittra, "The characteristic basis function method (CBFM): A numerically efficient strategy for solving large electromagnetic scattering problems," *Turk J Elec Engin*, vol. 16, no. 1, 2008.
- [34] R. Coifman, V. Rokhlin, and S. Wandzura, "The fast multipole method for the wave equation: A pedestrian prescription," *IEEE Trans. Antennas Propag.*, vol. 35, no. 3, Jun. 1993.
- [35] M. V. Kezhong Zhao and J.-F. Lee, "Application of the multilevel adaptive cross-approximation on ground plane design," *IEEE Trans. Antennas Propag.*, vol. 38, no. 8, pp. 1053–1058, Aug. 1990.
- [36] Website:, "<http://web.archive.org/web/20070811210939/http://linmic.com/sms.htm>."

- [37] P. A. Bernard and J. M. Gautray, "Measurement of dielectric constant using a microstrip ring resonator," *IEEE Trans. Antennas Propag.*, vol. 39, no. 3, Mar. 1991.
- [38] R. Olsson, P.-S. Kildal, and M. Shields, "Measurements of a 150 to 1700 mhz low loss eleven feed for the 42 m radio telescope at green bank," *Antennas and Propagation Society International Symposium 2006, IEEE*, pp. 347–350, 2006.
- [39] K. Chang, *Microwave Ring Circuits and Antennas*, ser. Wiley Series in Microwave and Optical Engineering. John Wiley and Sons, Inc., 1996.
- [40] F. Gardiol, *Microstrip Circuits*, ser. Wiley Series in Microwave and Optical Engineering. John Wiley & Sons, Inc., 1994.
- [41] K. C. Gupta, R. Garg, and I. J. Bahl, *Microstrip Lines and Slotlines*. Artech House, INC., 1979.
- [42] E. Yamashita and R. Mittra, "Variational method for the analysis of microstrip lines," *IEEE Trans. Antennas Propag.*, vol. MTT-16, no. 4, Apr. 1968.
- [43] E. Yamashita, "Variational method for the analysis of microstrip-like lines," *IEEE Trans. Antennas Propag.*, vol. MTT-16, no. 8, Aug. 1968.
- [44] M. Naeem, R. Maaskant, G. W. Kant, P.-S. Kildal, and R. Mittra, "The method of equivalent dipole moments (MEDM) combined with CBFM for the fast and accurate solution of dielectric scattering problems," *International Conference on Electromagnetics and Advanced Applications (ICEAA)*, Sep. 2011.